Spray Characteristics of Fire Sprinklers

David Thomas Sheppard
Northwestern University
Mechanical Engineering Department
Evanston, IL 60201

NIST GCR 02-838

Spray Characteristics of Fire Sprinklers

Prepared for
U.S. Department of Commerce
Building and Fire Research Laboratory
National Institute of Standards and Technology
Gaithersburg, MD 20899-8663

By
David Thomas Sheppard
Northwestern University
Mechanical Engineering Department
Evanston, IL 60201

June 2002

NORTHWESTERN UNIVERSITY

Spray Characteristics of Fire Sprinklers

A DISSERTATION

SUBMITTED TO THE GRADUATE SCHOOL
IN PARTIAL FULFILMENT OF THE REQUIREMENTS

for the degree

DOCTOR OF PHILOSOPHY

Field of MECHANICAL ENGINEERING

By

DAVID THOMAS SHEPPARD

EVANSTON, ILLINOIS

June 2002

Abstract

Although fire sprinklers have been in use for over 100 years there has been little progress toward developing analytical methods of calculating their effectiveness. This lack of progress is primarily due to absence of information about initial spray characteristics near sprinklers. In this study, experiments were conducted near a variety of sprinkler designs utilizing 1) a pulsed laser sheet and CCD camera and 2) phase Doppler interferometry.

Particle image velocimetry analysis of the CCD camera images has shown that velocities near the sprinklers can be described as a purely radial flow with the origin located between the orifice and deflector for pendant sprinklers and between the orifice and slightly above the deflector for upright sprinklers. The average radial droplet velocity at a distance 0.2m from the sprinkler orifice is 53% of the water velocity through the orifice with a 0.08% standard deviation. The maximum spray velocities ranged from 62% to 120% of the orifice water velocity with a statistically significant trend for higher maximum velocities from pendant sprinklers. The radial velocity is strongly dependent on the elevation angle and less dependent on the azimuthal angle. The radial velocity is a function of the specific sprinkler model, so a general description of the radial velocity independent of sprinkler model is not very accurate. The radial droplet velocity is proportional to square root of the water pressure entering the sprinkler.

The droplet size distribution can be measured by phase Doppler interferometry techniques close to the sprinkler. The median droplet diameter increases with elevation

angle. The median droplet diameter decreases with increasing water pressure, and relationship that has been suggested for the median droplet diameter to be proportional to the –1/3 power of the Weber number was found valid, but the proportionality constant depends on the location in the spray.

The water flux can be calculated from the visible drops in the CCD images. The water flux is strongly dependent on the elevation angle and on the azimuthal angle. The measurement technique is able to discern measurable increases in water flux at locations coinciding with large notches in the sprinkler deflectors. The details of the water flux are somewhat dependent on the water pressure, although the general characteristics of the water flux remain independent of water pressure. The water flux distribution vary so much with pressure and sprinkler type that it is impossible to determine a universal water flux distribution or to assume axisymmetry for the water flux.

Acknowledgements

My graduate education would not have been possible without the patient support of my wife Beth. I would like to thank Richard Lueptow for his guidance. Pravinray Gandhi was the one that made it possible to pursue this degree while working. The phase Doppler tests in this research were possible due to the help of John (Jay) Schwille.

Contents

List of Figures

x

List of Tables

1   Introduction

Fires in the United States cause hundreds of millions of dollars in damage and thousands of deaths each year. To combat this problem, fire protection professionals are increasingly using automatic fire sprinkler systems to control fires [1].

Fire sprinklers have been used in this country to protect warehouses and factories for over one hundred years. Because of changes in building codes and in building construction design, new sprinklers are being designed all the time. Unfortunately, because of the complexity of the physics of sprinkler spray/ fire interaction, there has been no engineering design procedure for deciding which sprinkler is best for a given installation. An engineer's sole basis for deciding whether a specific sprinkler design will control a fire is based upon a limited number of expensive large-scale fire tests that may or may not represent a real fire scenario. This current method of designing sprinkler systems has resulted in a situation where engineers often do not know how effective their suppression systems are, nor do they have a quantifiable measure of the level of safety.

Recent advances in instrumentation and computers are bringing the understanding of sprinkler spray / fire interactions within reach of scientists. The advent of advanced methods of measuring droplet size and velocity allow a detailed look at the actual characteristics of sprinkler sprays. Because of the large number of droplets and the complexity of the interactions between the fire, the surrounding air and the sprinkler droplets, the best way to successfully model sprinkler sprays is computationally. The use of high-speed computer workstations allows the physics of the interactions to be

combined with empirical results to develop a more comprehensive understanding of the sprinkler spray/fire interaction. Unfortunately, empirical information about the sprinkler spray that the computational models require as input has until now been unavailable.

1.1 Research Goal

The goal of this research was to measure the sprinkler spray characteristics required as input for computational sprinkler spray models. The approach that was taken was to experimentally measure the spray characteristics of real fire sprinklers using state-of-the-art diagnostic techniques. The experimental results were then studied to find relationships in the spray characteristics that could be used to simplify later modeling and analysis. Because of the wide variety of existing sprinkler designs, there was concern that relationships developed for a limited sample of sprinklers would not be widely applicable. Therefore, a large number of sprinklers types encompassing a cross-section of commercially available sprinklers were evaluated.

1.2 Background

Fire sprinklers are positioned near the ceiling of rooms where the hot "ceiling jet" spreads radially outward from the fire plume as shown in Figure 1. When the temperature at an individual sprinkler reaches a pre-determined value, the thermal element in the sprinkler activates permitting the flow of water.
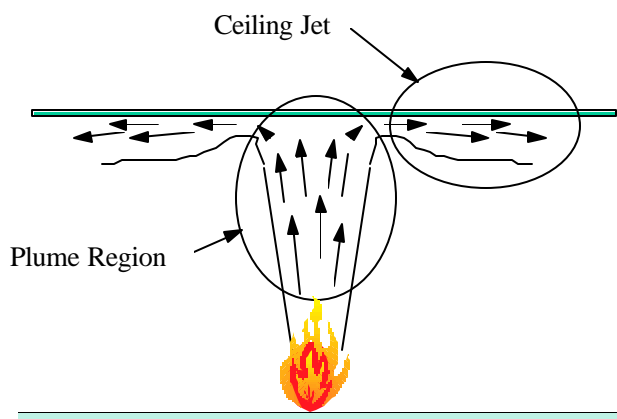
Figure 1. Fire plume dynamics

The sprinkler spray serves three primary purposes: (i) it delivers water to the burning material and reduces the combustion rate by preventing further generation of combustible vapor, (ii) it wets the surrounding material which reduces the flame spread rate, and (iii) it cools the surrounding air by evaporation and displaces air with inert water vapor.

In order for a sprinkler spray to achieve its design purposes it must have the following characteristics. Sprays from sprinklers located directly above the fire must have sufficient vertical momentum to penetrate the fire plume and reach the burning commodity. Spray from sprinklers located in the ceiling jet must have sufficient horizontal momentum to counteract the ceiling jet flow and reach the burning commodity positioned between sprinklers. The spray must absorb enough heat from the plume and ceiling jet to lower the temperatures to an acceptable level.

The limiting factor in sprinkler system design is the amount of water available for the sprinklers. The optimally designed sprinkler system will activate exactly enough

sprinklers at the appropriate time to control the fire. If the sprinkler system responds too slowly, the fire will grow too large to be controlled by the sprinklers. If the sprinkler system responds too quickly, too many sprinklers will operate increasing the water damage and reducing the water available to the sprinklers near the fire.

1.3   Sprinkler Designs

A typical sprinkler is shown in Figure 2. Water from the sprinkler ejects from the circular orifice to form a water jet. The water jet impacts the metal deflector that redirects the flow and forms the water into a spray. The deflector is held rigidly in place by two metal frame arms at opposite sides of the sprinkler. The water leaves the deflector in thin streams called ligaments [2, 3, 4. 5] that break up into droplets due to surface tension. Sprinkler water flow rates are typically in the range of 1.8 to 7.6 $\ell \cdot \sec^{-1}$, and there are typically on the order of 10^8 droplets in the air at any time for each sprinkler.
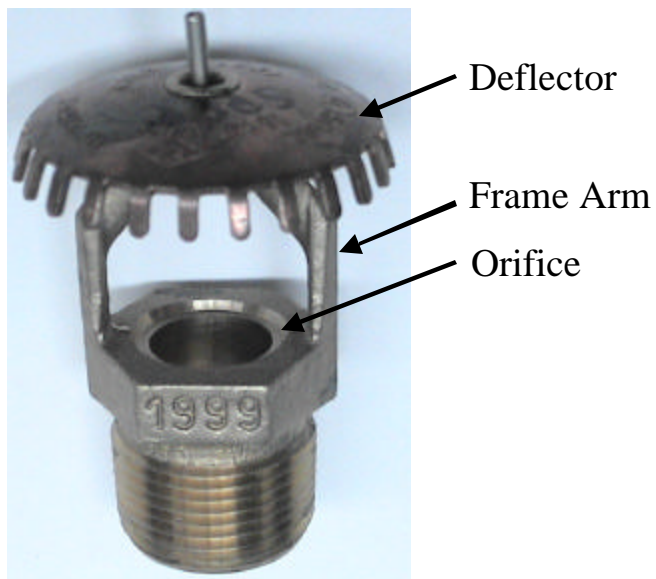
Figure 2. Typical Sprinkler Design

Before the late 70's most sprinklers were constructed with 12.7mm or 13.5mm orifices and were designed to provide a flow rates in the range of 1.2 to 2.9 $\ell \cdot \sec^{-1}$. Research conducted in the 70's and 80's showed that specialized sprinklers could be designed that were more effective in controlling certain types of fires. This research stimulated a renaissance in sprinkler design, where many specialized sprinkler designs were developed for special applications. Figure 3 shows schematically several different sprinkler types.

Traditional Upright   Modern Upright   Standard Pendant   Early Suppression Fast Response
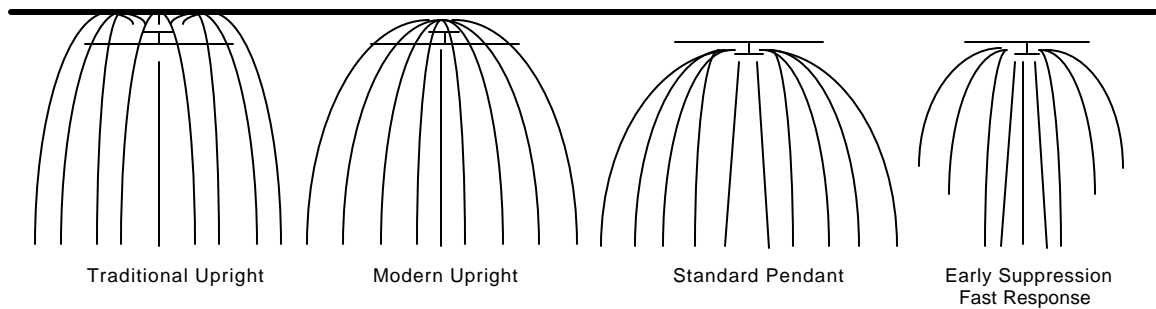
Figure 3. Sprinkler Examples

Traditional Upright sprinklers direct the spray toward the ceiling from which droplets fall to the floor. These sprinklers cool and wet the ceiling above a fire with the water falling off of the ceiling to the area below. These sprinklers are still in wide spread use in Europe, but they are used infrequently in new installations in the United States. Although *Modern Upright* sprinklers are above the water pipe, they are designed to spray the water radially to fall to the area below without necessarily wetting the ceiling. For both upright designs, the pipe interferes with the distribution of the spray as droplets fall downward. *Standard Pendant* sprinklers are directed downward from the pipe and spray the water radially. The pendant design minimizes the effect of the water pipe on the spray distribution. *Early Suppression Fast Response* (ESFR) sprinklers are designed to direct the spray downward directly beneath the sprinkler to provide maximum water delivery in a localized region. ESFR sprinklers are used in applications where the fire source is likely to grow rapidly.

One of the fundamental discoveries that came out of fire sprinkler research was that sprinklers that produced larger median droplet sizes were better able to control fires in areas with high ceilings[6]. As a consequence of the inverse relation between the operating pressure and the mean droplet diameter (discussed in section 1.6), there has been a trend towards designing sprinklers with larger orifices to obtain lower pressures. Another result of this research was the realization that smaller droplets absorbed more of the heat from the air [7].

As a result, sprinkler designers work empirically to balance the number of high momentum large drops that can suppress the fire with the number of smaller drops that cool the fire plume and reduce activation of sprinklers away from the fire. There are currently no analytical methods for determining this balance, and for this reason the design of sprinklers is more of an art than a science.

Sprinklers are designed to be mounted in many different orientations as suggested in Figure 3. The most common styles are mounted with the orifice pointing upward (upright style), with the orifice pointing downward (pendant style), or mounted horizontally (sidewall style).

The sprinkler orifice is designed to provide a known water flow rate at a design water pressure. Sprinkler orifices conform to Bernoulli's orifice equation, which states that the velocity of the water through the orifice is proportional to the water pressure, P [8]. For sprinkler design applications the volumetric flow rate, Q, is more germane than the velocity. Therefore for design applications, Bernoulli's orifice equation is rewritten as

$$Q = k \sqrt{P} \qquad (1.1)$$

The orifice flow coefficient, k, is known as the sprinkler "K-Factor". It is nearly constant for the range of operating pressures used in sprinkler applications. The K-Factor

is nominally proportional to the square of the orifice diameter[1]. The units used for the K-

Factor are $\ell \cdot minute^{-1} \cdot bar^{-1/2}$ or $gallons \cdot minute^{-1} \cdot psi^{-1/2}$.

1.4 Sprinkler Water Distribution

Sprinklers come in many different designs, and as a result, the water distribution

from different sprinklers varies widely. It is important for engineers to understand the

water distribution for different sprinklers in order to choose the correct sprinkler for

specific applications. An example of the wide differences in water distribution can be

observed in the results of "ten pan" tests shown schematically in Figure 4. Ten pan tests

are typically conducted as part of sprinkler approval testing. Ten pan tests are conducted

using one sprinkler located above a rotating array of pans. Ten pan tests provide a

measure of the delivered water flux as a function of radial distance from the fire.
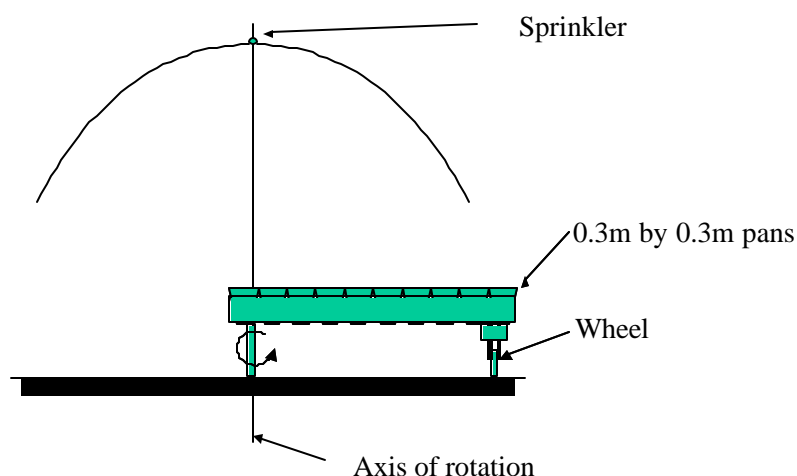
Figure 4. Pan distribution tests

---

[1] This was confirmed by a linear regression of the average K-Factor to the square of the nominal orifice diameter from NFPA 13 Table 2-2.2 has a 99.2% correlation coefficient .

Figure 5 shows the delivered water flux for six different sprinklers from ten-pan tests conducted at Underwriters Laboratories. The measurements were taken on a horizontal plane 3m (10 ft.) below the sprinklers. Models 3, 5, and 6 were evaluated with two water pressures. Figure 5 clearly shows that the water distribution is highly dependent on sprinkler design. For example, the model 1 sprinkler has a maximum water flux of 1.7e-3 m^{-2} directly below the sprinkler at a radial distance of 0m after which it plunges to a local minimum of 1.9e-4 m^{-2} at 0.6m and then reaches a local peak at a water flux of 1.1e-3 m^{-2} for a distance of 1.2 m before decreasing to near zero water flux at 2.7m. On the other hand, the model 6 sprinkler has a very different water flux distribution with a low water flux of 3.7e-4 m^{-2} directly below the sprinkler increasing to a maximum of nearly 1.1e-3 m^{-2} at 0.6m before decreasing to near zero at 2.7m. For the sprinklers that were tested at two water pressures, there are sometimes similarities between the shape of the water distribution functions, but the water distribution functions can be very different. For example, the two tests with the model 6 sprinkler are very similar with the curves nearly overlying each other. The two curves for the model 3 sprinkler on the other hand look very different with the first test at a maximum water flux directly below the sprinkler and the second test with the maximum flux at a radial distance of 1.2m.
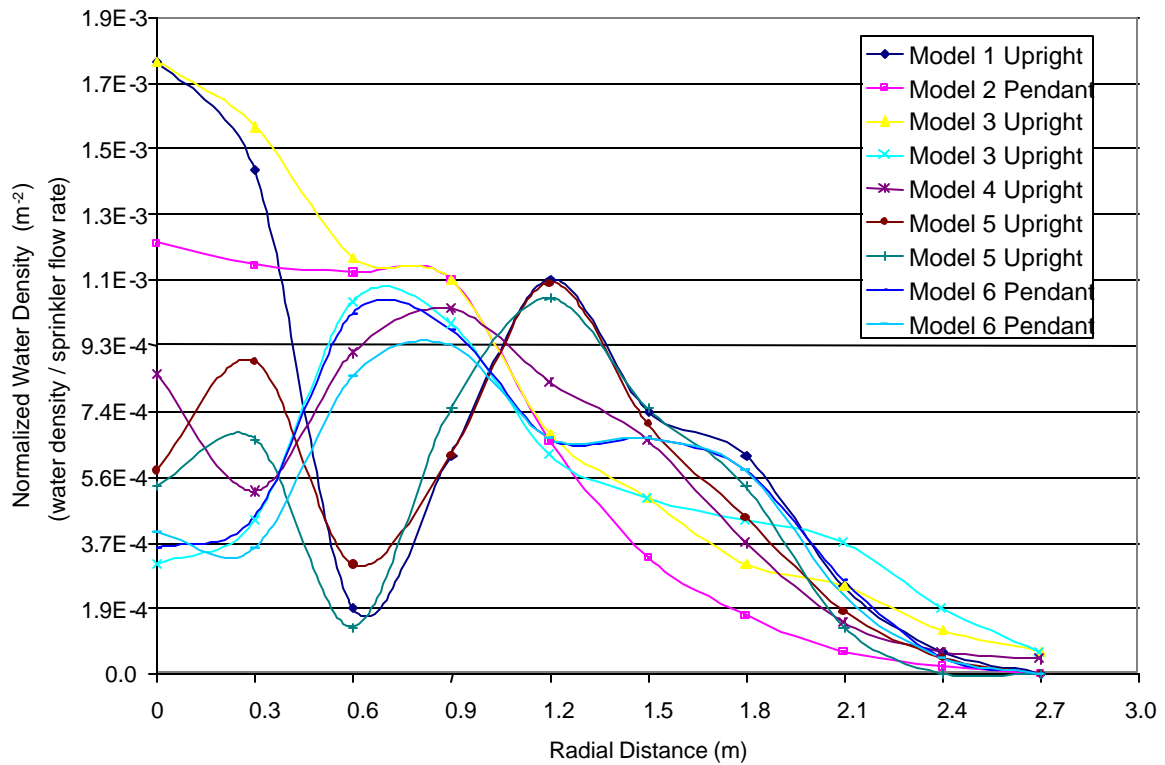
Figure 5. Delivered water flux as a function of radial distance from the fire.

The wide variation in the water distribution in Figure 5 for the different sprinklers demonstrates that sprinkler sprays are different for different sprinklers. Some sprinklers have high water flux in locations where other sprinklers have low water fluxes. For this reason, some sprinklers are more effective at controlling certain fires than others. In order for engineers to optimize sprinkler system designs they need to match a specific sprinkler with a optimal water pressure and mount it in a location where it would deliver the most water to the fire location.

1.5   Fire Environment

The heat from the fire is transferred to the sprinkler by radiation and convection. The primary radiation heat source is the flaming region of the fire. The convective heat is transferred upward from the fire via a buoyant plume. When the gas plume reaches a horizontal obstruction such as the ceiling it becomes a momentum driven flow called the ceiling jet, shown in Figure 1.

To be effective in reducing the combustion rate and the spread of the flames, the sprinkler droplets must traverse the distance from the sprinkler to the fire through the ceiling jet, fire plume and the flaming region.   Throughout the traverse, the droplets are losing momentum to the counteracting force of the fire plume and ceiling jet. Droplets are also losing mass due to evaporation.

The thermodynamic measure of fire size is the heat release rate also known as the fire power [9]. The size of typical fires in buildings range from several kilowatts to tens of megawatts. The heat release rate from fires is an unsteady phenomenon. For an uncontrolled fire, there is typically a growth phase, a steady burning phase, and a decay phase as the combustible material is fully consumed. It is important to note that the heat release rate from burning items can not easily be calculated analytically with accuracy.

Historically, the growth phase of fires has been generalized in terms of "t^2 fires", where the heat release rate grows with the square of time from the start of the fire. Fires

have been categorized as four different types, depending on the combustible materials

and fire conditions, according to Table 1 [10].

Table 1. Growth Rate for Standard t² Fires

Slow	$Q = \left(0.00293\dfrac{kW}{\sec^2}\right)t^2$	(1050 kW in 600 seconds)
Medium	$Q = \left(0.01172\dfrac{kW}{\sec^2}\right)t^2$	(1050 kW in 300 seconds)
Fast	$Q = \left(0.0469\dfrac{kW}{\sec^2}\right)t^2$	(1050 kW in 150 seconds)
Ultra-fast	$Q = \left(0.1876\dfrac{kW}{\sec^2}\right)t^2$	(1050 kW in 75 seconds)

The t² fire descriptions are empirical generalizations of the heat release rates from

measurements of real fires. The time for a fire to grow to 1050 kW is also indicated in

the table. This time varies by an order of magnitude depending on the type of fire.

Because each real fire has a different heat release growth rate, fire protection engineers

have found it convenient to design to generalized heat release curves. For example, the

engineer may check his fire protection design against medium, fast and ultra-fast fires to

assure that the design objectives will be met.

In order for the sprinkler spray to reach the location of the fire, it must penetrate

the buoyant stream of hot gases above the fire called fire plume as shown in Figure 1.

The fire plume is usually turbulent except for very small fires [11]. There are many

empirical correlations for calculating plume temperatures and velocities [11]. For

axisymmetric plumes, the correlations are based upon an analysis by Morton[12] in

which he showed that the buoyant plume radius, b, is proportional to the height, z, and

that the plume velocity, u, and the excess temperature in the plume over the ambient air,

ΔT are both functions of the convective heat release rate of the fire, Q_c, and the height, z,

as shown below

$$b \propto z \tag{1.2}$$

$$u \propto Q_c^{1/3} z^{-1/3} \tag{1.3}$$

$$\Delta T \propto Q_c^{2/3} z^{-5/3} \tag{1.4}$$

Researchers have found these relationships to be accurate above the mean flame

height of the fire[13]. The proportionality constants found by researchers for the plume

radius in (1.2) range from 0.15 to 0.18. The proportionality constants for the centerline

velocity in (1.3) range from 0.8 to 1.2 $m \cdot s^{-1} \cdot kW^{-1/3} m^{1/3}$. The proportionality constants

for the centerline temperature difference, $\Delta T = T_{CL} - T_\infty$, in (1.4) range from 21 to 30.5

$^\circ C \cdot kW^{-2/3} m^{5/3}$ [11].

The plume equations provide insight about the operating environment and the

design considerations for fire sprinklers. The plume width equation shows that in lower

ceiling areas the plume is relatively narrow and it would be unlikely that the sprinkler

would be located in plume region directly above the fire given the typical spacing

between sprinklers. Therefore, the spray would probably not travel through the plume

until it reached the immediate vicinity of the fire unless it happened to be right above the

fire. In high ceiling areas, such as warehouses and factories where the typical sprinkler

spacing is 3m by 3m, the sprinkler would almost always be located in the plume. Therefore the spray would have to penetrate through the entire height of the plume. In the high ceiling application, the sprinkler spray would need to contain a large fraction of large droplets that would not evaporate before reaching the fire, and the droplets would need to contain enough vertical momentum to counteract the opposing flow of the fire plume. In the low ceiling application, the droplet size required to reach the fire is much smaller because the droplets will be subject to the plume evaporation for a much shorter period. The droplets also do not need as great a vertical momentum because they need not travel as far vertically in the plume. The plume velocity equations further show that the plume velocities are typically on the order of 1 to 10 $m \cdot s^{-1}$ for most fires. The relation for the temperature of the plume suggests that there has to be a substantial fire before the sprinklers activate. For example, in a typical low ceiling area z=3m, the fire would be on the order of 100kW before a 74°C sprinkler would activate. In a in a typical high ceiling area z=10m, the fire would be on the order of 3000kW before a 74°C sprinkler would activate.

1.6   Scaling of Sprinkler Parameters

Appropriate dimensionless variables for sprinklers are given in Table 2.

Table 2. Sprinkler Scaling Parameters

Ratio of droplet diameter, d, to sprinkler dimension, d_s.	$\dfrac{d}{d_s}$	(1.5)
Ratio of liquid density, r, to air density, r_∞	$\dfrac{r}{r_\infty}$	(1.6)
Ratio of liquid viscosity, m, to air viscosity, m_∞.	$\dfrac{m}{m_\infty}$	(1.7)
Reynolds Number (ratio of momentum to viscous forces)	$\mathrm{Re} = \dfrac{r\,u\,d}{m}$	(1.8)
Weber Number (ratio of momentum to surface tension forces)	$\mathrm{We} = \dfrac{r\,u^2\,d}{s}$	(1.9)

Here u is the velocity, σ is the surface tension of the liquid, and the characteristic sprinkler dimension, d_s, is typically assumed to be the orifice diameter.

A key issue in fire sprinklers is the relation between the droplet diameter and the sprinkler orifice diameter. Orifice sizes for commercially available sprinklers are typically in the range $9 \le d_s \le 25$mm. The diameters for individual droplets are in the range $0 \le d_i \le 5000\mu$m. The diameters for mean diameter values in the spray (see Chapter 6) are typically in the range 200μm $\le d \le 1400\mu$m. Therefore, we expect that the nondimensional parameter defined by the droplet diameter to the sprinkler dimension would be in the range

$$0.008 \leq \frac{d_m}{d} \leq 0.156 \qquad (1.10)$$

The Reynolds number, *Re*, plays an important role in determining the drag of the air on the droplets and consequently on the trajectories of individual droplets. Figure 6 shows the Reynolds number for the range of velocities and drop diameters found in sprinkler flows. The kinematic viscosity of air at 300K was used for these calculations. The velocities in Figure 6 range from 0.1 to 20 m·s^{-1} representing the range velocities measured in sprinkler sprays. The five curves in Figure 6 represent the Reynolds numbers for the droplet diameters from 1μm to 5000μm, which encompasses the measured range of droplets sizes. It is clear that the Reynolds number for droplets created by sprinklers span several orders of magnitude of *Re*.
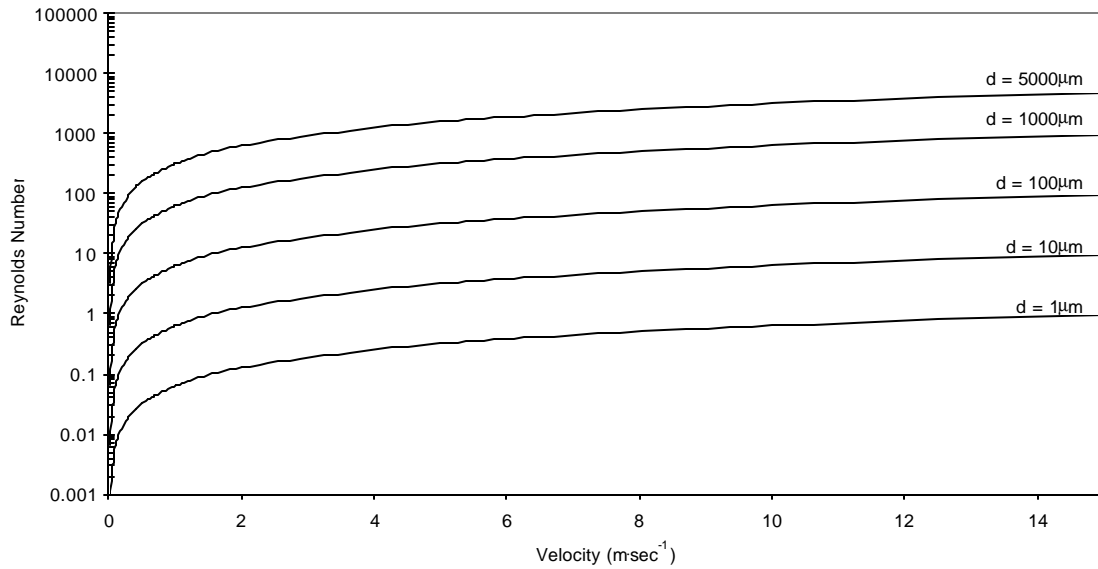
Figure 6. Reynolds Number for Various Drop Diameters and Velocities

Droplet size is typically related to the surface tension through the Weber number, *We*. For the sprinklers in this study $10^2 \leq \text{We} \leq 10^5$ depending on the velocity at the orifice and the orifice diameter.

The instability of a liquid jet was studied by Rayleigh [14], who showed that an infinite cylindrical jet of an inviscid liquid becomes varicose as it passes through air forming a series of connected globules at a characteristic distance, λ. This wavelength was theoretically found to be independent of the properties of the liquid and was found to be related to the diameter of the water jet, d_j, such that

$$\frac{\lambda}{d_j} \cong 4.51 \qquad (1.11)$$

By conservation of mass, equation (1.11) gives the diameter of the droplets, d_1, formed by the globule

$$\frac{\pi d_1^3}{6} = \frac{\pi d_j^2}{4} \lambda \qquad (1.12)$$

Weber [15] extended this work and analyzed the effects of viscosity as well as the surface tension forces and produced a relationship for a breakup of a liquid sheet into ligaments in equation (1.13).

$$\frac{\lambda}{d_{Lig}} = \pi\sqrt{2}\left(1 + \frac{3\text{We}_{Lig}^{1/2}}{\text{Re}_{Lig}}\right)^{1/2} \qquad (1.13)$$

where d_{Lig} is the ligament diameter, Re_{Lig} is the Reynolds number calculated for the ligament, and We_{Lig} is the Weber number for the ligament.

The diameter of the resulting droplets, d_1, can be calculated with the aid of equation (1.12).

$$d_1 = d_{Lig} \left(\frac{3p}{\sqrt{2}} \right)^{1/3} \left(1 + \frac{3We_{Lig}^{1/2}}{Re_{Lig}} \right)^{1/6} \tag{1.14}$$

Dombrowski and Johns [16] showed that for an expanding liquid sheet of uniform velocity, u, with finite viscosity, μ, that ligaments were produced at the edge of the sheet whenever the amplitude of the waves became greater than the thickness of the sheet. They further extended the analysis to derive an equation that can be used to relate the ligament diameter, d_L, to the orifice diameter, d, of the spray device

$$\frac{d_L}{d} = \frac{0.4807}{We^{1/3}} \left(\frac{r}{r_\infty} \right)^{1/6} \left(1 + 0.312 \frac{We^{5/3}}{Re} \left(\frac{r_\infty}{r} \right)^{4/3} \right)^{1/5} \tag{1.15}$$

Dundas [17] noted that the term to the one-fifth power on the right-hand side of equation (1.15) never exceeds 1.01 for sprinkler applications where orifice diameters are less than 25mm and water pressures are less than 550 kPa. Dundas then noted that the right hand bracket in equation (1.14) never exceeds 1.006 for sprinkler applications. Combining (1.14) and (1.15), Dundas could relate the sprinkler orifice size to the droplet diameters.

$$\frac{d_D}{d} = 2.77 We^{-1/3} \qquad (1.16)$$

This relationship has been widely used in sprinkler spray analysis because it allows the characteristic droplet size in the spray to be calculated using known parameters about the sprinkler. For the sprinklers in this study $10^2 \leq \text{We} \leq 10^5$. The Dundas equation (1.14) predicts that the droplets sizes in this study vary only by a factor of 10.

1.7 Droplet Trajectories

Analysis is conducted in this section to show that several sprinkler spray characteristics are a result of droplet trajectory. Although this analysis seems elementary, most of the conclusions reached here have not been discussed in the literature. The results of this analysis will be used as a basis of many of the conclusions in later chapters.

The trajectory of single droplet can be described with Newton's second law (1.17) [18]. The left hand side represents the change in momentum of the drop. The first term on the right hand side is the force of gravity on the droplet. The second term is the drag force that the surrounding air exerts on the droplet as it moves through the air [19]. This simple form of the force balance on a droplet omits several higher order correction terms such as the droplet buoyancy, added mass and the Basset History force that are inconsequential in this case.

$$\frac{d}{dt}\left(m_d \vec{u}_d\right) = m_d \vec{g} - \frac{1}{2} r C_d A_d \left(\vec{u}_d - \vec{u}_\infty\right)\left|\vec{u}_d - \vec{u}_\infty\right| \qquad (1.17)$$

Here m_d is the mass of the droplet, g is the acceleration due to gravity, r is the density of water, A_d is the projected area of the droplet, C_d is the drag coefficient, u_d is the velocity of the droplet and u_∞ is the velocity of the surrounding air. The quantities g, u_d and u_∞ are vectors. The drag coefficient is described by the following equation [20]

$$C_d = \frac{F_{drag}}{\frac{1}{2} r A_d \left(\vec{u}_d - \vec{u}_\infty\right)^2} \qquad (1.18)$$

where F_{drag} is the drag force.

Figure 7 shows the relation of the drag coefficient to the Reynolds number for rigid spheres for the range of Reynolds Numbers shown in Figure 6. The two dashed curves show analytical results for Stokes' and Oseen's solutions to the sphere drag problem. The data points represent experimental results. The solid curve represents an empirical correlation based upon the experimental data [20].
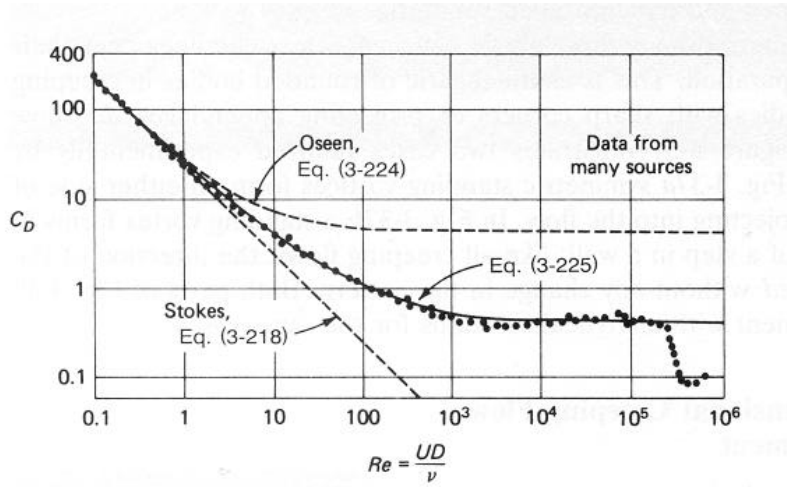
Figure 7. Drag coefficient for a solid sphere [20]

For flows around spheres where Re < 1, the drag coefficient can described using Stokes' sphere drag formula

$$C_d = \frac{24}{\text{Re}} \qquad\qquad \text{Re} < 1 \qquad\qquad (1.19)$$

For Reynolds numbers less than 10^5, White suggests that a curve fit based upon empirical results be used [20].

$$C_d = \frac{24}{\text{Re}} + \frac{6}{1+\sqrt{\text{Re}}} + 0.4 \qquad 0 < \text{Re} < 10^5 \qquad (1.20)$$

If the droplets are treated as solid spheres, the terminal velocity and the time to achieve the terminal velocity after leaving the sprinkler can be estimated. If the droplet

size is assumed to be constant and the air velocity is assumed to be zero equation (1.17)

can be rewritten as follows.

$$\frac{\partial u}{\partial t} = g - \frac{3 \boldsymbol{r}_\infty}{8 r \boldsymbol{r}} C_d u_d^2 \qquad (1.21)$$

When Stokes' sphere drag formula is used for Re<1, the terminal velocity, V_t, can

be found by solving equation (1.21) for the case when the droplet acceleration equals

zero.

$$V_t = \frac{2 r^2 g \, \boldsymbol{r}}{9 v \, \boldsymbol{r}_\infty} \qquad (1.22)$$

where v is the kinematic viscosity and r is the droplet radius. For Re<1, the velocity as a

function of time can be found analytically by solving (1.21).

$$u(t) = \frac{1}{9 \boldsymbol{n} \, \boldsymbol{r}_\infty} \left[2 g r^2 \boldsymbol{r} + e^{\left(-\frac{9 v \boldsymbol{r}_\infty}{2 r^2 \boldsymbol{r}} t \right)} \left(-2 g r^2 \boldsymbol{r} + 9 V_o v \, \boldsymbol{r}_\infty \right) \right] \qquad (1.23)$$

where V_o is the initial velocity of the droplet. When the empirical drag formula is used

for Re > 1, the equation for the terminal velocity is more complicated.

$$0 = g - \frac{3 \boldsymbol{r}_\infty}{8 r \boldsymbol{r}} \left[\frac{12 v}{r V_t} + \frac{6}{1 + \sqrt{2 r V_t / v}} + 0.4 \right] V_t^2 \qquad (1.24)$$

This is most easily solved numerically. For Re>1, equation (1.21) becomes

$$\frac{\partial u}{\partial t} = g - \frac{3\boldsymbol{r}_{\infty}}{8r\boldsymbol{r}}\left[\frac{12v}{r\,u} + \frac{6}{1+\sqrt{2\,r\,u/v}} + 0.4\right]u^2 \qquad (1.25)$$

This cannot be determined analytically and must be solved numerically.

Table 3 and Figure 8 show the terminal velocities calculated by solving equations (1.22) and (1.24). Assumptions that have been made are that the droplets are solid spheres of constant size, the temperature is 300K, and the velocity of the air is negligible.

Table 3. Terminal Velocities

Droplet Diameter (m)	Reynolds Number	Terminal Velocity, (m·s^{-1})
1.00E-06	1.89E-06	3.0E-05
1.00E-05	1.89E-03	3.0E-03
1.00E-04	1.57E+00	0.24691
0.001	227.1	3.564
0.002	751	5.89
0.003	1467	7.67
0.004	2336	9.16
0.010	9906	15.54

The sprinkler droplets leave the sprinkler at an initial velocity on the order of 1 to 15 m·s^{-1}. After leaving the sprinkler, the droplet velocities will approach their terminal velocity. From Table 3 and Figure 8, it is clear that droplets less than 1 mm diameter will slow down and droplets larger than 1 mm diameter will speed up in order to approach their terminal velocity.
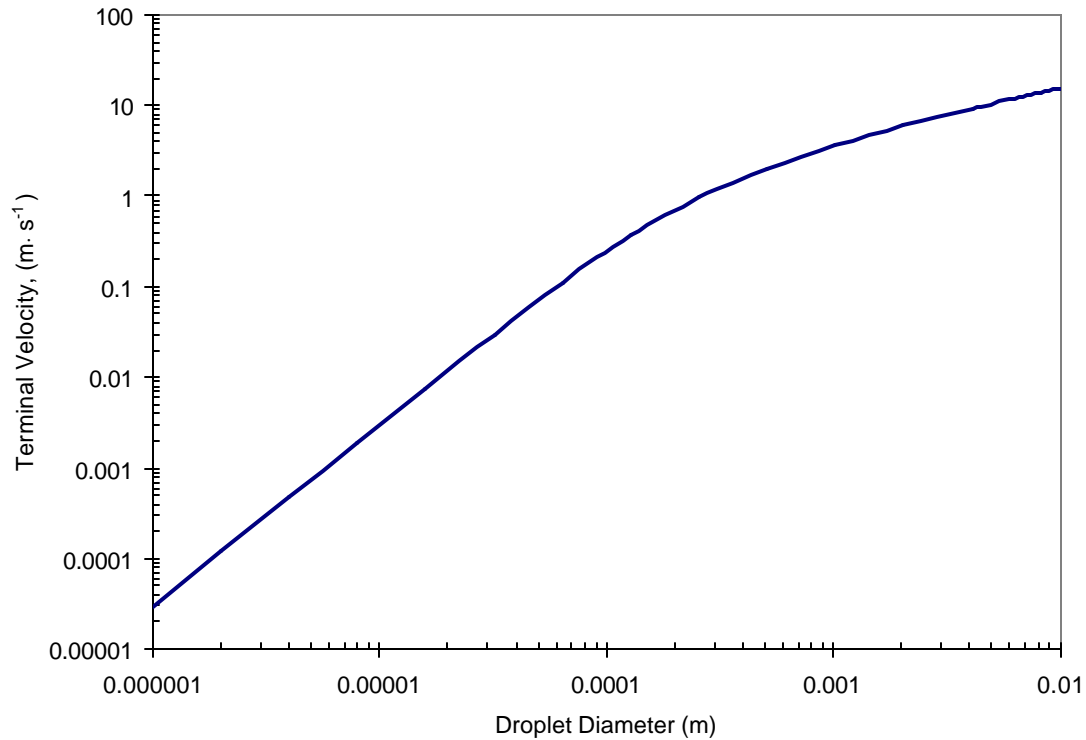
Figure 8. Calculated Terminal Velocity as a Function of Droplet Diameter

Figure 9 shows the calculated vertical velocity of 0.5 mm droplets as a function of time for a range of initial vertical velocities. The droplets have no initial horizontal velocity. They are assumed to have an initial downward vertical velocity at 0 seconds that is different from the terminal velocity. The graph was constructed based on a 4th order Runge-Kutta solution of equation (1.25). Figure 9 is interesting in that it shows that a 0.5mm droplet achieves its terminal velocity in about 0.5 seconds, regardless of its initial velocity.

Since the goal of the research was to characterize the sprinkler flows and since for practical reasons test measurements have to taken at some distance away from the

sprinklers, it is important to determine how far the droplets travel before reaching

terminal velocity.
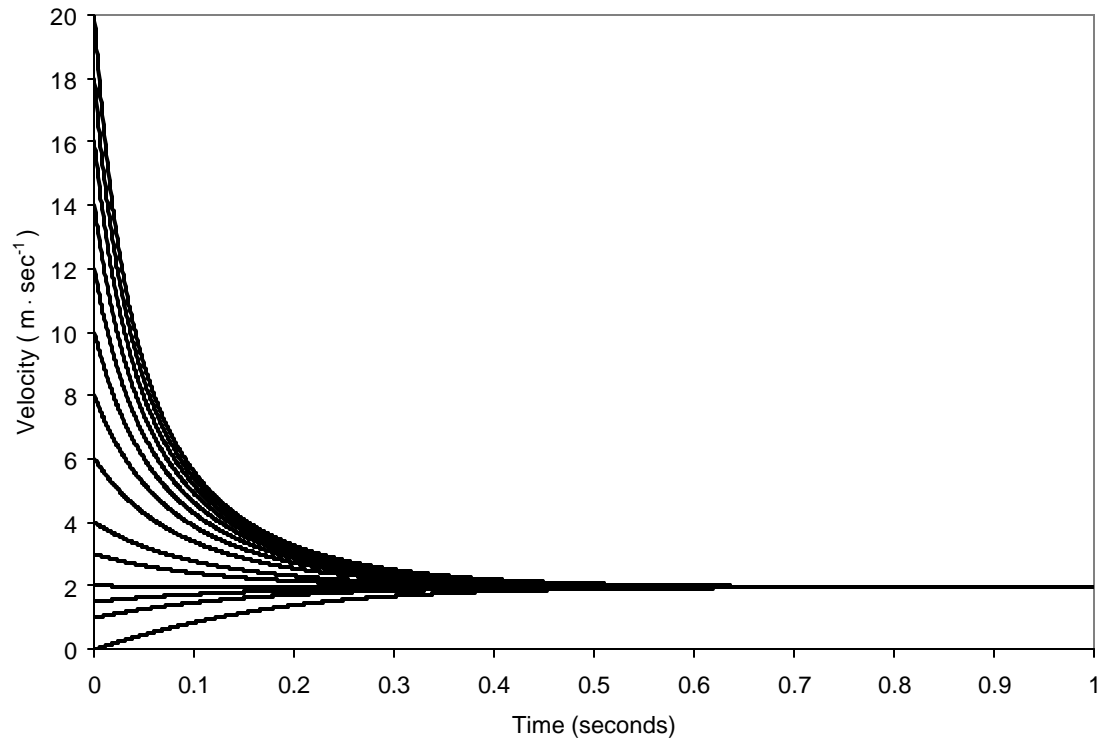
Figure 9. Vertical downward velocities of 0.5mm droplets with different initial vertical velocities

Table 4 shows the distance traveled when the droplets have achieved 95% of their

terminal velocity as a function of droplet diameter and initial velocity. All values were

calculated using a 4th order Runge-Kutta solution of equation (1.25). Assumptions that

have been made are that the droplets are solid spheres of constant size, the temperature is

300K, the velocity of the air is negligible and all velocity is in the vertical direction.

Table 4. Distance Traveled when Droplets Achieve 95% of Terminal Velocity (m)

Droplet Diameter	Initial Droplet Velocity					
	0.1 m/s	1 m/s	2 m/s	5 m/s	10 m/s	20 m/s
0.000001 m	3.53E-07	3.5E-06	6.96E-06	1.71E-05	3.35E-05	6.47E-05
0.00001 m	3.54E-05	0.000299	0.00057	0.00130	0.00237	0.00414
0.0001 m	0.002378	0.013203	0.0240	0.0512	0.0869	0.140
0.001 m	1.73	1.678333	1.47	1.77	3.43	4.83
0.01 m	13.0	13.9	14.7	16.4	16.2	18.7

It is evident from Table 4 that droplets smaller than 0.001m reach their terminal velocity very close to the sprinkler, whereas droplets larger than 0.001m may travel a significant distance before reaching their terminal velocity. Since the typical vertical dimension for fire sprinklers above the floor is on the order of 3 to 7m, it is quite likely that many of these larger droplets never reach their terminal velocity before hitting the floor or the burning commodity.

The theoretical results of the terminal velocity and distance required to achieve the terminal velocity are consistent with the experimental results that Chan [21] measured in a limited series of tests that were conducted on two ESFR type sprinklers. Figure 10 is a Figure from Chan's report showing the droplet velocity versus the droplet diameter. The solid line shows the experimentally-measured terminal velocities for individual droplets. The symbols show the experimental measurements of sprinkler droplet velocity 3.2m below the sprinkler. Clearly the droplets are at their terminal velocity at this position below the sprinkler.
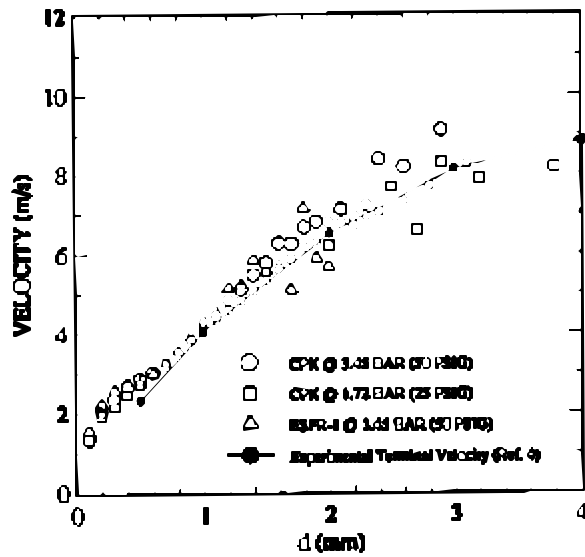
Figure 10. Comparison of Experimental Results to Terminal Velocity [22]

The fact that Chan found that droplet velocities measured on a horizontal plane 3.2m (10 ft.) below the sprinkler compared closely to the terminal velocities for individual droplets is also consistent with our analysis of distance required to achieve the terminal velocity.

An interesting aspect of the drag coefficient is that it couples the horizontal and vertical components of the droplet velocity. This is because the drag coefficient, C_d, is a function of the Reynolds number, which is a function of the magnitude of the vector sum of the horizontal and vertical components of the velocity. The drag coefficient, C_d, decreases as the Reynolds number increases (see Figure 7 and equation (1.20)). Therefore increasing either the horizontal or vertical velocity components will decrease the drag coefficient, which consequently effects the vertical velocity of a droplet.

This effect is illustrated in Figure 11 which shows the velocity versus time for 0.0001m droplets that have an initial horizontal velocity and a zero initial vertical velocity. The velocities were calculated using the droplet trajectory equation (1.17). The seven traces shown in Figure 11 are for different initial horizontal velocities. Figure 11 shows that for a 0.0001m droplet that the downward velocity can be substantially increased for a short time by the effects of the horizontal velocity.
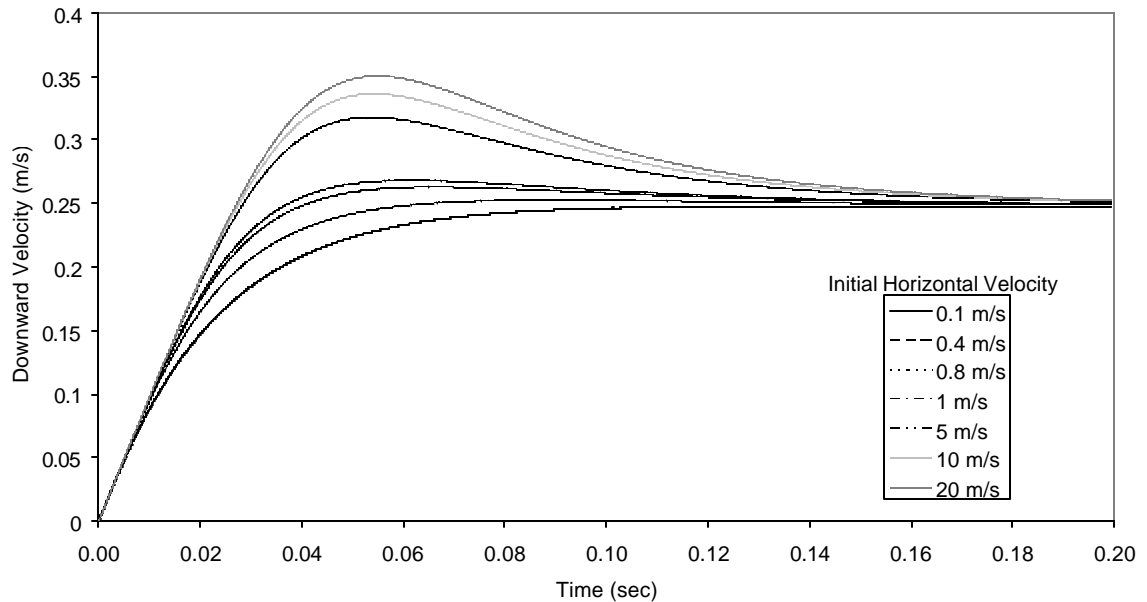
Figure 11. downward velocity of 0.0001m droplets falling from rest with an initial horizontal velocity

The dependence of the vertical distance that a droplet would fall before it achieves 95% of its terminal velocity on the initial vertical and horizontal velocities was also investigated using equation (1.17). This evaluation used initial vertical and horizontal velocities of 0, 0.1, 1, 2, 5, 10, and 20 m·s^{-1} on droplets of 10^{-6}, 10^{-5}, 10^{-4}, 10^{-3}, and 10^{-2} m diameters. For droplets with diameters less than or equal to 10^{-4}, the vertical

distance to achieve vertical velocity changed by less than 0.005 m from droplets with no horizontal component of velocity. For droplets with diameters greater than 10^{-4} changes in vertical distances on the order of 1 meter were observed in some cases. Thus, both the initial horizontal and vertical velocities need to be used to properly model trajectory.

The droplet trajectory equation (1.17) was solved to evaluate the effect of droplet diameter on horizontal travel distance. Figure 12 shows the horizontal distance as a function of droplet diameter that droplets would travel in 3m of vertical travel. The seven traces in Figure 12 are for different initial horizontal velocities. The initial vertical velocity was zero.
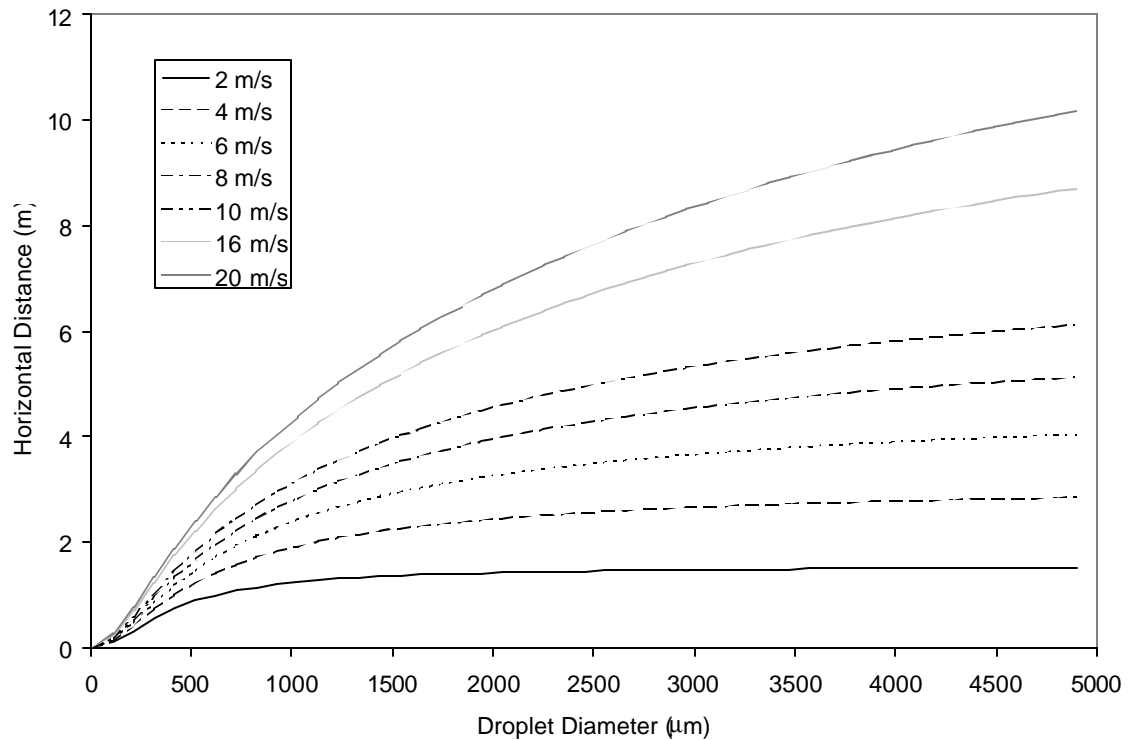
Figure 12. Horizontal travel distance 3m below the sprinklers as a function of droplet diameter for different initial horizontal velocities.

It is evident that larger droplets travel further horizontally than smaller droplets regardless of the initial horizontal velocity. For example, at an initial velocity of 4 m·s^{-1} a 500μm droplet will travel about 1m and a 1000μm droplet will travel almost 2m. When the initial velocity is increased to 8 m·s^{-1} the 500μm droplet will travel about 1.7m and the 1000μm droplet will travel over 3m. This effect seems reasonable given that the larger droplets have more initial momentum and a smaller drag coefficient. This relationship between the droplet diameter and the radial distance is further studied in Chapter 6.

1.8   Droplet Size

Sprinkler sprays are composed of droplets ranging in diameter by over two orders of magnitude. The number of droplets of each size depends on the sprinkler design, water pressure and location in the spray. In order to characterize these sprays statistical techniques are used to define parameters such as characteristic diameters and statistical size distributions.

The size of a spherical droplet is uniquely defined by its diameter. Equivalent diameters are determined by measuring a size dependant property of an arbitrary non-spherical droplet such as volume or surface area and relating it to the diameter of an equivalent spherical droplet. Examples of common equivalent diameters used in droplet analysis are shown in Table 5.

Table 5. Equivalent Diameters Defining Droplet Size [22, 23]

Symbol	Name	Definition	Formula
D_1	Diameter	Diameter of sphere	D
D_3	Volume Diameter	Diameter of sphere having same volume as a droplet	$V = \dfrac{\boldsymbol{p}}{6} d_1^3$
D_2	Surface Diameter	Diameter of a sphere having same surface as a droplet	$S = \boldsymbol{p} d_1^2$
D_{32}	Surface Volume Diameter (Sauter Diameter)	Diameter of a sphere having the surface to volume ratio as a droplet.	$D_{32} = \dfrac{d_3^3}{d_2^2}$
DV50	Volume Median Diameter	Half of a given volume of water is contained in droplets greater than this diameter and the other half in droplets smaller than this diameter	

In spray analysis, the mean values of these diameters are used as a primary indicator of the spray characteristics. For example, when the intended use of the droplet size information is to determine the mass of transported water, the mean diameter calculated from the volume, d_3, would be appropriate. For the sprinkler heat transfer function of removing heat from the fire plume to limit the number of activated sprinklers and to remove heat in proximity to the fire the Sauter mean diameter, d_{32}, is the key parameter. This parameter balances the convective heat transfer, which is a function of the droplet surface area, with the heating of the droplet water which is a function of the droplet mass (volume).

For sprinkler water distribution analysis, the volume median diameter, DV50, is the key droplet length scale. By definition, half of a given volume of water is contained

in droplets greater than this diameter and the other half in droplets smaller than this

diameter.

The equivalent mean diameters d_1, d_2 and d_3 for sprays with different size droplets

are calculated as ensemble averages as shown in equations (1.26), (1.27), and (1.28)

$$d_1 = \frac{1}{N} \sum_{i=1}^{N} d_i \tag{1.26}$$

$$d_2 = \sqrt{\frac{1}{N} \sum_{i=1}^{N} d_i^2} \tag{1.27}$$

$$d_3 = \sqrt[3]{\frac{1}{N} \sum_{i=1}^{N} d_i^3} \tag{1.28}$$

The Sauter mean diameter, d_{32}, is derived from the volume diameter and the

surface diameter as shown in (1.29)

$$d_{32} = \frac{d_3^3}{d_2^2} \tag{1.29}$$

The volume median diameter, DV50, for a spray with different sized droplets is

calculated by finding the droplet size below which half of the volume of water is

contained. This is accomplished by first calculating total volume of water, V, contained

in the droplets by summing the volumes of all droplets. The droplet diameters and their

associated volumes are then sorted in ascending order. The cumulative volume by

droplet size is then calculated for each droplet size. The DV50 diameter is chosen as the

diameter at which the cumulative volume is one half of the total water volume. When

one half of the total water volume is not located at a measured droplet diameter, linear interpolation is used to calculate DV50.

Although there is currently no physical explanation for this, it has been found that the droplet size distribution sometimes follow a well behaved function [24] known as the 'droplet distribution function', ddf. Faeth [25, 26] and Chow [27] have reviewed different spray modeling approaches and documented empirically based ddf functions. The most common distribution functions used to describe sprays are the log-normal distribution function and the Rosin-Rammler distribution function.

The log-normal distribution is given by

$$y = \frac{1}{d\boldsymbol{s}_{\ln}(2\boldsymbol{p})^{1/2}} \exp \frac{-\left[\ln(d/d_m)\right]^2}{2\boldsymbol{s}_{\ln}^2} \tag{1.30}$$

where y is the probability of a droplet of size d, $\boldsymbol{s}_{\ln}$ is the variance of the log-normal distribution, and d_m is the median droplet size. Any droplet size measure can be used for d_m, but typically for droplet studies, the median volume diameter, DV50 is used. The units of d, d_m, and σ are typically μm for droplet studies. The Rosin-Rammler distribution is given by

$$y = \boldsymbol{g}\,\boldsymbol{b}\,\frac{d^{\boldsymbol{g}-1}}{d_m^{\boldsymbol{g}}} \exp\left[-\boldsymbol{b}\left(\frac{d}{d_m}\right)^{\boldsymbol{g}}\right] \tag{1.31}$$

where β and $\boldsymbol{g}$ are a constants that depend on the sprinkler spray.

Figure 13 shows an example of the shape of the log-normal and Rosin-Rammler droplet distribution functions. Both functions were calculated using a median diameter of 800μm and a standard deviation, σ_{ln}, of 0.6. The additional constants used for the Rosin-Rammler were 0.7 and 1.6 for β and γ respectively. The Rosin-Rammler distribution is significantly more symmetric about the mean than the log-normal and it has a much smaller range of droplet sizes. The log-normal has fewer of the smallest droplets (droplets less than 100 μm for this scenario) and many more of the larger droplets.
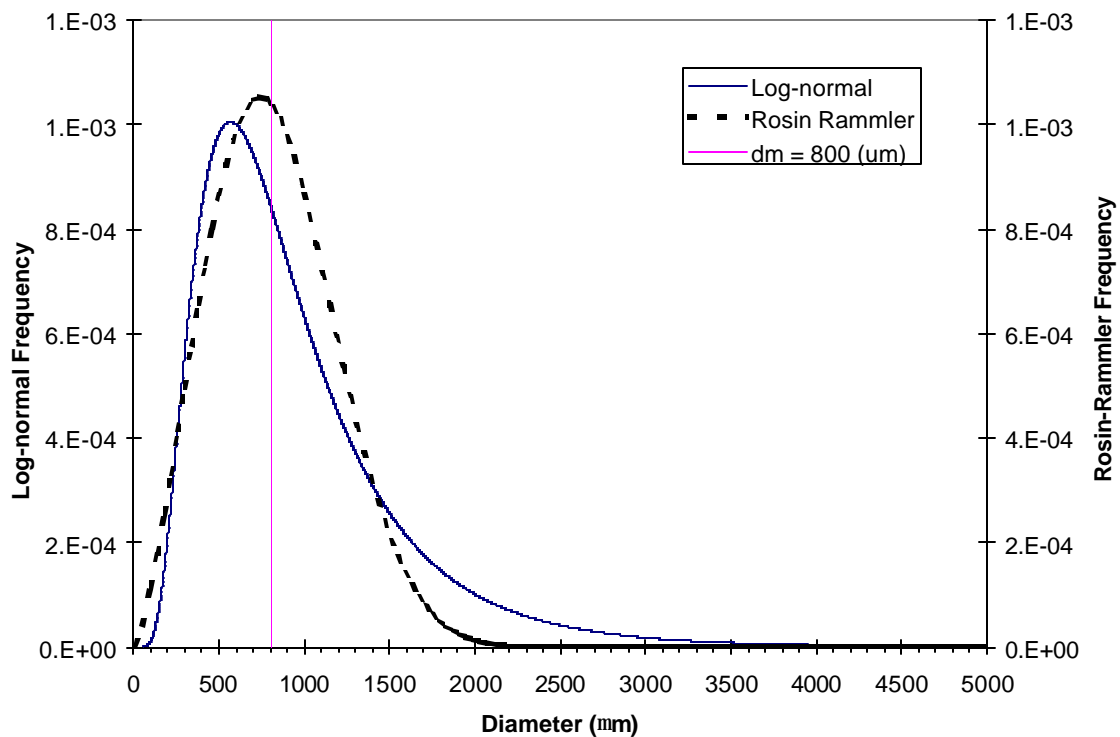
Figure 13. Typical log-normal and Rosin-Rammler droplet distribution functions dm=800μm, s_{ln} = 0.5, b = 0.7 and g= 1.7.

The cumulative volume fraction, CVF, is the integral of the droplet distribution function. It is useful for defining the fraction of the total water volume that is carried by

water of given diameters. An analytical solution could not be obtained for the log-normal equation (1.30) so it was calculated numerically. The Rosin-Rammler equation (1.31) can be integrated as

$$CVF_{RR} = 1 - \exp\left[-\boldsymbol{b}\left(\frac{d}{d_m}\right)^{\boldsymbol{g}}\right] \qquad (1.32)$$

Figure 14 shows the CVF functions for the log-normal and Rosin-Rammler functions using the same values as those for Figure 13. A vertical line showing the median diameter, d_m, has been added to the chart. Notice that the two functions intersect at the median diameter. Below the median diameter the Rosin-Rammler always has a smaller CVF than the log-normal except for the smallest droplets. Above the median diameter, the Rosin-Rammler always has a greater CVF.
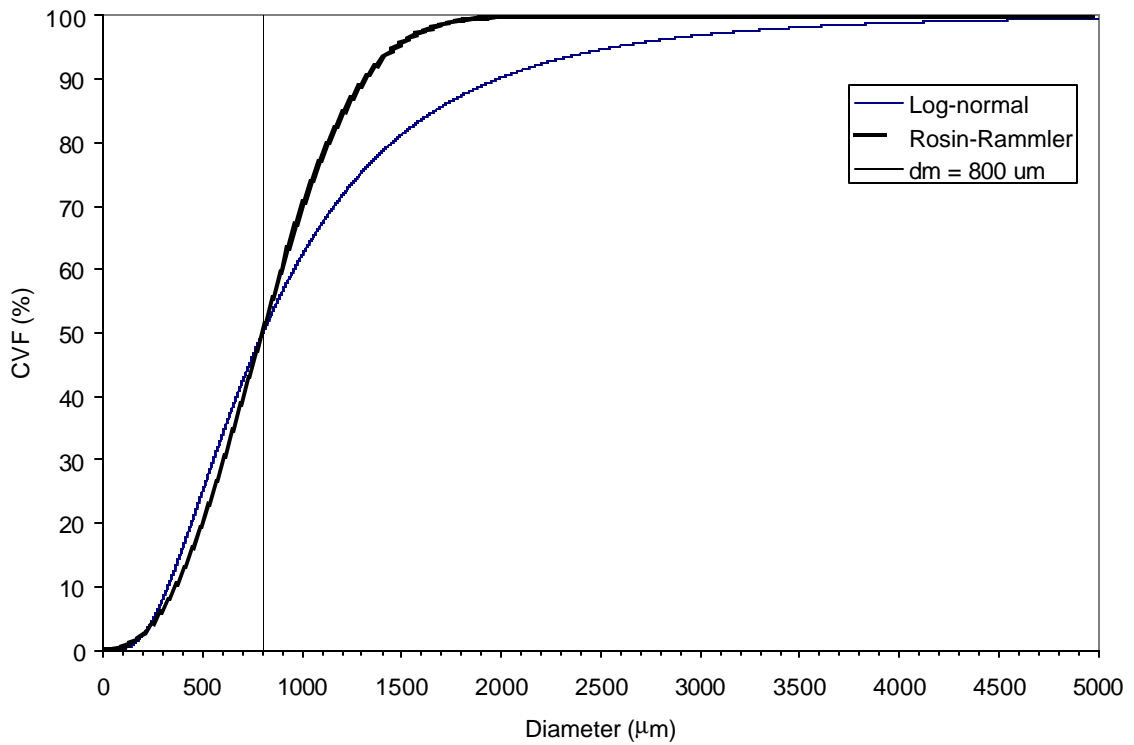
Figure 14. Typical CVF for log-normal and Rosin-Rammler with dm=800 μm, s_{ln} = 0.5, b = 0.7 and g = 1.7.

A different technique for plotting the CVF is shown in Figure 15 using the same data as in Figure 14 but plotting with a normal probability scale for the CVF and a log scale for the diameter. Plotted in this manner the log-normal CVF function is a straight line and the Rosin-Rammler distribution is a curve that intersects the log-normal at the median diameter.
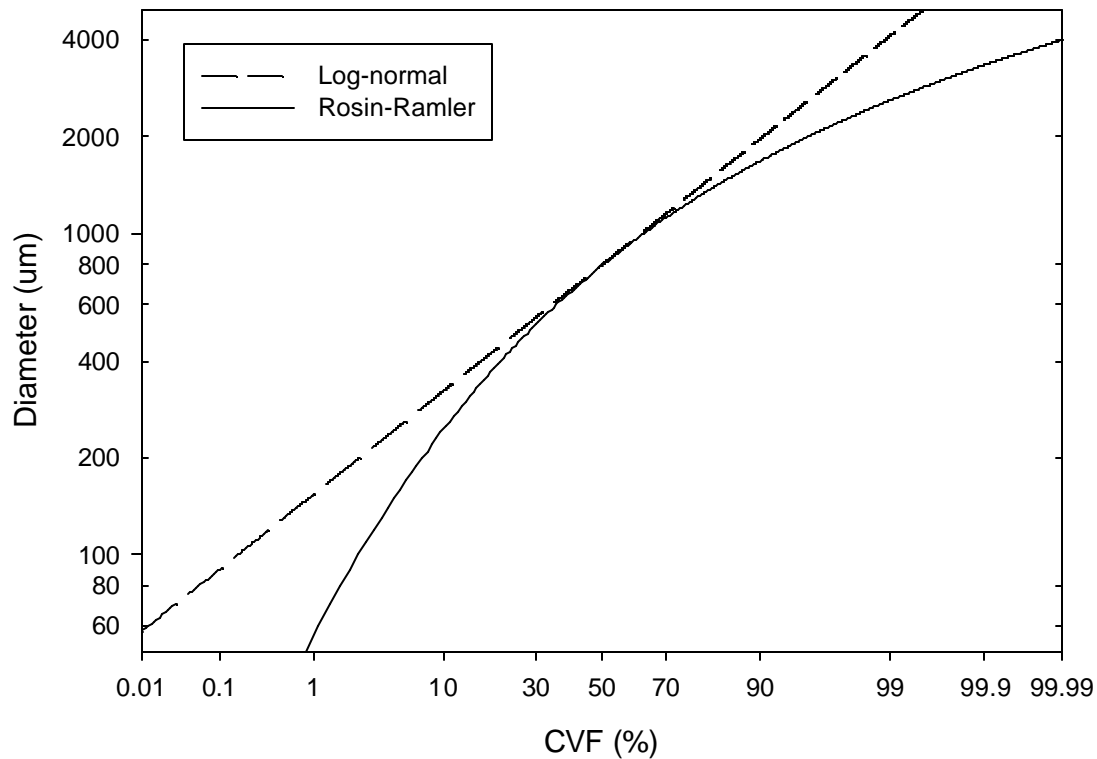
Figure 15. Typical CVF for log-normal and Rosin-Rammler dm=800mm, s_{ln} = 0.5, b = 0.7 and g = 1.7.

Hayes[28] compiled a literature survey of existing sprinkler droplet data and found few existing studies on real sprinklers. The few existing sprinkler droplet experiments that have been conducted on real sprinklers have been conducted as distances of at least 1m from the sprinkler and therefore do not provide the information about initial spray characteristics near the sprinklers. Furthermore, most of the studies only present histograms of droplet counts and sometimes a table of mean droplet diameters. All of the studies, except those by Widmann [29,30,31] and Gandhi [32,33], who used the same equipment as was used in this study, were conducted using equipment that is crude by today's standards. Consequently, it was determined that there was no

existing research that would provide detailed information about droplet sizes near the sprinklers.

Only one study by You [34] provides droplet size distribution functions calculated for fire sprinklers. You's experiments were limited to two sprinklers with the same orifice size and the measurements were taken along horizontal planes 3.05 or 6.10m below the sprinklers. He found that the data conformed to a log-normal distribution below the volume median diameter, DV50, and a Rosin-Rammler above DV50. The log-normal standard deviations was in the range $0.56 \leq \sigma_{ln} \leq 0.78$ and the Rosin-Rammler constants were in the ranges $0.61 \leq \beta \leq 0.70$ and $1.54 \leq \gamma \leq 1.78$. An example of the CVF function using combined distributions based You's experimental results is shown in Figure 16.
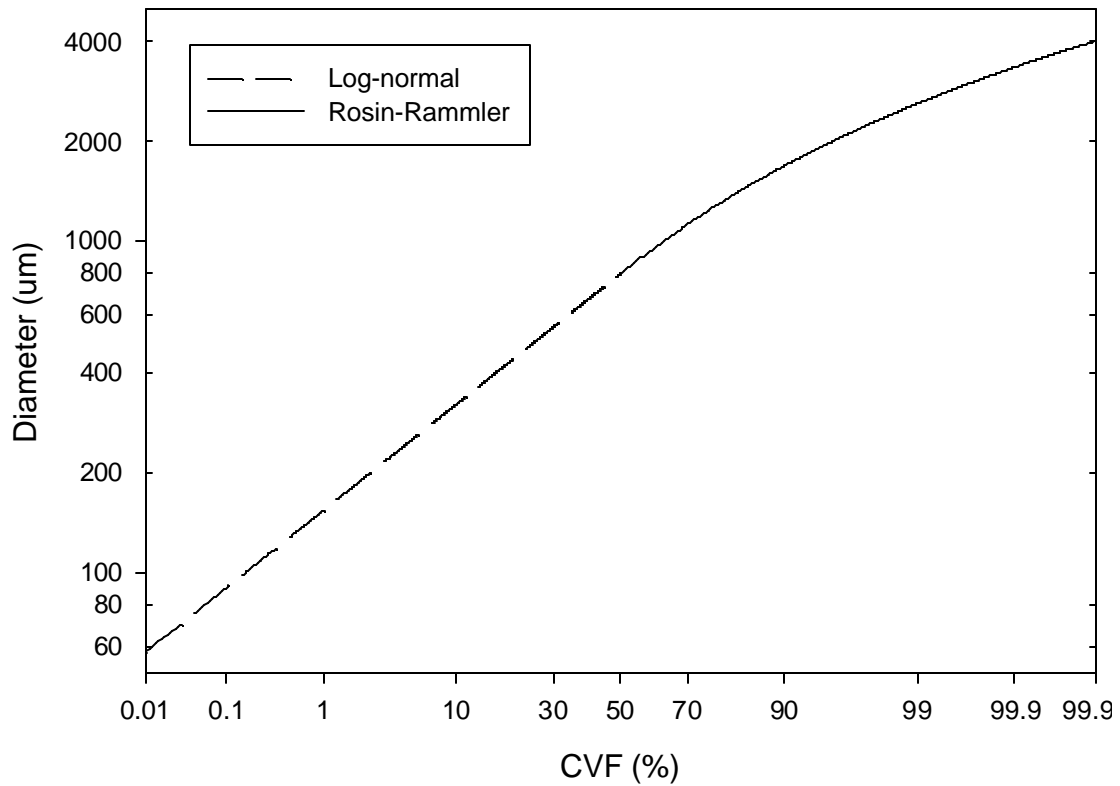
Figure 16. You's combination log-normal and Rosin-Rammler CVF with dm=800μm, s_{ln} = 0.5, b = 0.7 and g= 1.7.

To date, fire sprinkler droplet distributions have been based upon You's limited experiments. However, the very limited scope of these experiments makes it unlikely that they would describe a wide variety of commercially available sprinklers.

1.9   Research Program

The goal of the research was to measure the sprinkler spray characteristics required to calculate sprinkler effectiveness using computer models. The spray characteristics of interest are velocity, *V*, size, *D*, and water flux, *F*, of the droplets the leaving the sprinklers. The characteristics that were measured as part of this research are a function of the sprinkler design as well as several other factors

$$d = d\left(Sprinkler,\ Flow\ Rate,\ \boldsymbol{q},\ \boldsymbol{f}\right)$$

$$u = u\left(Sprinkler,\ Flow\ Rate,\ \boldsymbol{q},\ \boldsymbol{f}\right) \tag{1.33}$$

$$\dot{m}'' = \dot{m}''\left(Sprinkler,\ Flow\ Rate,\ \boldsymbol{q},\ \boldsymbol{f}, N\right)$$

where *d* is the statistical droplet size distribution, u is spray velocity, $\dot{m}''$ is the water flux and N is the number density of droplets. All of these factors are functions of the sprinkler design, the flow rate of water through the sprinkler, the elevation angle, $\boldsymbol{f}$, and azimuthal angle, $\boldsymbol{q}$, and the radial distance from the sprinkler.

The spray characteristics were measured near a variety of real fire sprinklers with realistic water flow rates using two laser based measurement techniques that provided information about the spray velocity, droplets sizes, and water flux.

The first series of experiments were conducted using particle image velocimetry (PIV) to provide information about sprinkler droplet velocities. The purpose of this series of experiments was to measure the velocities and also to determine when the stream flow exiting the sprinkler evolves into a fully developed droplet flow. A schematic of the PIV measurement locations is shown in Figure 17. The rectangular box indicates the region in which the sprinkler spray was imaged with PIV. The sprinkler was rotated with respect to the PIV region to provide data about the spray as a function of azimuthal angle, θ.
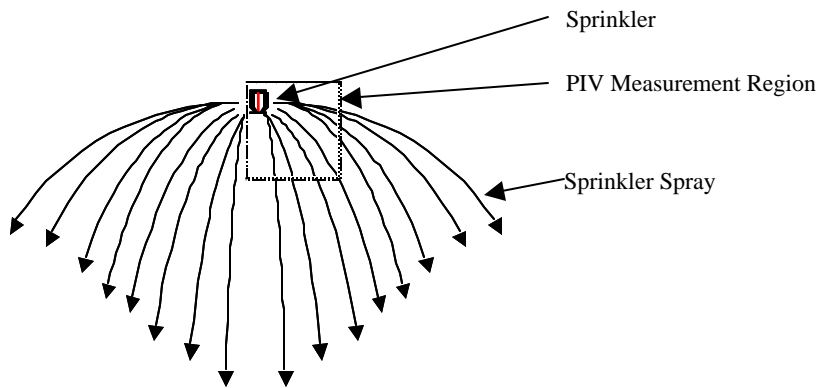
Figure 17. Particle image velocimetry test scenarios

The second series of experiments was conducted using phase Doppler interferometry (PDI). PDI provides extremely detailed information about the droplet sizes. The measurement locations for the PDI determined from the results of the PIV experiments. A schematic of the PDI measurement locations is shown in Figure 18.
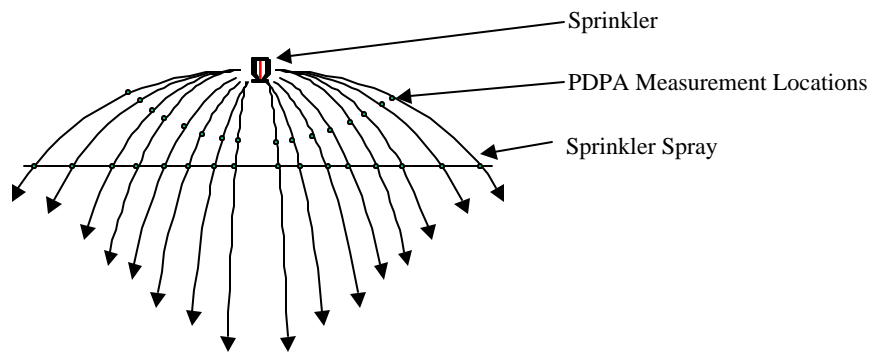
Figure 18. PDI test scenarios

The results of the PIV and the PDI measurements were then evaluated. The PIV results provided broad maps of droplet velocity. The PDI results provided point measurements of droplet size distributions. The combination of these results were used to develop a characterization of the sprinkler spray that has been used to derive a realistic model of sprinkler spray.

2 Experimental Methods

The spray characteristics were measured near a variety of real sprinklers at realistic water flow rates. Two complementary laser-based systems were used for experiments characterizing the droplet size and velocity distributions. Underwriters Laboratories has a state-of-the-art phase Doppler interferometry (PDI) system which was used to measure droplet sizes, and Northwestern University has a sophisticated laser sheet particle image velocimetry (PIV) system which was used for flow visualization and to measure spray velocity. Both systems are ideal for the study of the different aspects of the size and velocity of droplets.

2.1 Phase Doppler Interferometry

The phase Doppler interferometry method is based on light scattering interferometry. Measurements are made in a small, non-intrusive optical probe volume defined by the intersection of two laser beams as shown in Figure 19. A spherical particle or droplet passing through the probe volume scatters light from the beams. The resulting interference fringe pattern is collected at an off-axis receiving lens. The lens projects a portion of the fringe pattern onto three detectors. Each detector produces a Doppler burst signal with frequency proportional to the particle velocity, which is the same technique as is used in a laser Doppler anemometer. But the Doppler burst signals from the different detectors are phase shifted. This phase shift is proportional to the size of the particles. Thus, a PDI system measures the particle velocity and size

simultaneously. A unique aspect of PDI is that both the droplet size and velocity

measurements require no calibration, since both depend only on the laser wavelength and

the optical configuration. The probe volume can be traversed to different positions in the

flow field for spatial mapping of the droplet velocity and size distributions. The problem

with PDI is that it is quite difficult to set up and align the lasers and detectors.
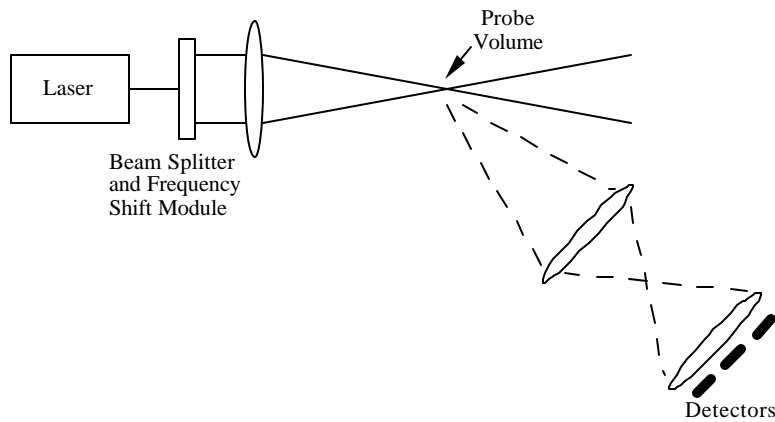
Figure 19. Sketch of PDI system

The experiments were conduced using a 2-component phase Doppler

interferometer with Real-time Signal Analyzer (RSA) available from TSI Inc. A 300

mW air-cooled argon ion laser operating in multi-line mode was used as the illumination

source, and the green (λ = 514.5 nm) line was used to measure the axial velocity and

droplet size. The transmitting optics were coupled to the beam conditioning optics using

fiber optic cables which permitted the transmitting optics to be located in the spray. The

front lens on the transmitting optics had a focal length of 1000mm. The measurements

were made at the intersection of the two laser beams in a measurement volume

approximately 0.1 m^3. The PDI system is capable of measuring particle sizes from 0.5

to 10,000μm depending on the configuration. The system has a dynamic size range of 50:1 at any one configuration with 4096 uniform size classes over the full range. The manufacturer suggests the size accuracy is 1% based on monodisperse drop measurements, comparison to other techniques, and data repeatability.

2.2   Laser Sheet Experiments

Although PDI can provide very accurate measurements of the velocity and size of droplets, the measurement occurs at a single point in the flow. This limitation is overcome by using Particle Image Velocimetry, which is capable of measuring the droplet motion in an entire plane of the flow. In PIV a sheet of high-intensity laser light is positioned within the flow field. A video camera is aligned perpendicular to the laser sheet so that it can image the droplets when they are illuminated by a flash of laser light that is only a few nanoseconds long as shown in Figure 20. Using a sequential pair of images of droplets, the velocity for any droplet could be determined if the same droplet can be identified in both images. This is usually not possible, so the statistical average of the displacement of many droplets in the same region of the imaged velocity field is determined using Fourier-based cross-correlation methods. In this way, a grid of velocity vectors for the droplets in the plane of the laser sheet can be determined simultaneously. The advantage of PIV over PDI is that PIV allows the determination of the velocity of particles over a plane of the flow rather than at a single point. PIV, however, does not typically provide information about the particle size.
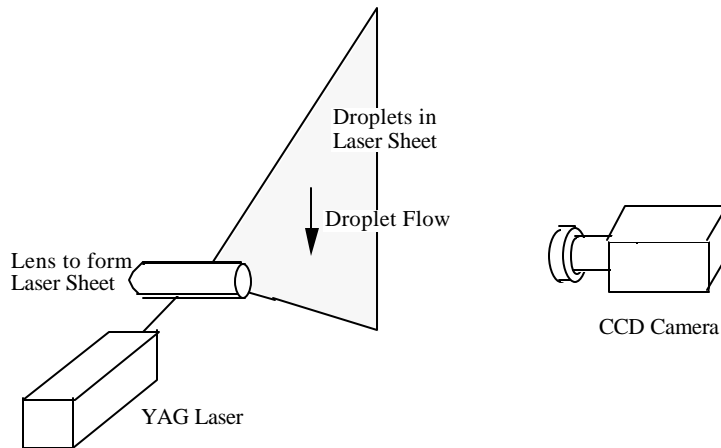
Figure 20. Sketch of PIV setup

The experiments were conducted using a Particle Image Velocimetry (PIV) system available from TSI, Inc. The illumination source was two solid state Nd:YAG pulsed lasers. The pulse duration was approximately 6-7 ns, and the time between paired pulses was 150 µs. The average energy output was 25mJ and the laser sheet thickness was approximately 0.001m. The lasers were mounted approximately 1m from the measurement region. A TSI model 10-30 CCD camera was used. The camera utilized an 8bit gray scale CCD with a 1000 by 1016 pixel resolution. The camera had a maximum rate of 30 frames per second controllable by a trigger pulse. The camera was equipped with a Nikon Micro-Niccor AF 60mm F/2.8 lens. The F stop on the lens was adjusted during each experimental set-up to maximize the visible drops while not allowing the laser illumination to saturate the image. The camera was mounted approximately 2m from the laser sheet. The laser pulses and CCD camera were controlled using a TSI model "LaserPulse" synchronizer.

The image system was calibrated whenever a component of the PIV system was moved and at the beginning of each day's testing. The calibration procedure consisted of mounting a ruler in the image region parallel with the location of the laser sheet. A single image was then captured with the CCD camera. The pixel locations corresponding with the longest distance visible on the ruler was then used to calculate the pixel resolution. The average region size in the laser images was 300 by 300mm corresponding to a resolution of 0.300 by 0.295 mm/pixel. The maximum region size used for some large orifice sprinklers was 390 by 390 mm corresponding to a resolution of 0.390 by 0.384 mm/pixel.

2.3   Test Facility

The experiments were conducted at the sprinkler spray measurement facility at Underwriters Laboratories in Northbrook, Illinois. This facility is located in a 9m by 7m test room with a pitched roof design from 5.5 to 6.7m in height. Centered in this facility is an elevated circular traverse 3.6m in diameter that can be rotated along the central axis. A 3m long horizontal branch line is suspended below the circular traverse approximately 4m above the floor. Sprinklers are mounted to the branch line along the axis of the circular traverse. Using this system, the azimuthal angle of the sprinkler can be positioned within 1 degree. Water to the sprinkler is provided by one of three pumps providing flow rates up to 0.038 m^3s^{-1} (600gpm).

The PDI and laser sheet equipment were mounted on a two axis traverse. The traverse has approximately 3m of movement in both the horizontal and vertical axis. The traverse was equipped with digital encoders and an electronic readout of position accurate to 0.01mm. For the sprinkler experiments, the traverse was positioned so that the origin of measurements was located at the center of the sprinkler orifice. In this manner, the exact measurement location with respect to the sprinkler was always known.
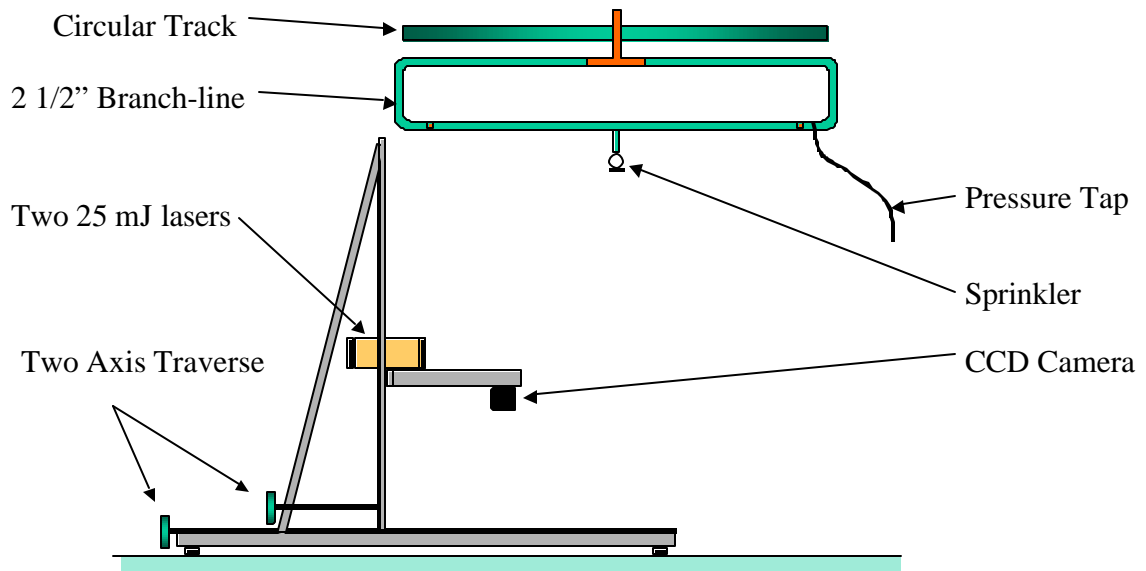
Figure 21. Test setup

2.4   Coordinate System

For purposes of the analysis a spherical coordinate system was used with the sprinkler at its origin as shown in Figure 22[2]. The azimuthal angle, $\theta=0°$ is parallel to the sprinkler frame arms. The elevation angle, $\phi=0°$ is vertically downward. This

convention for ϕ means that for pendant sprinklers water flow through the orifice is at $\phi=0°$ and for upright sprinklers water flow through the orifice is at $\phi=180°$.
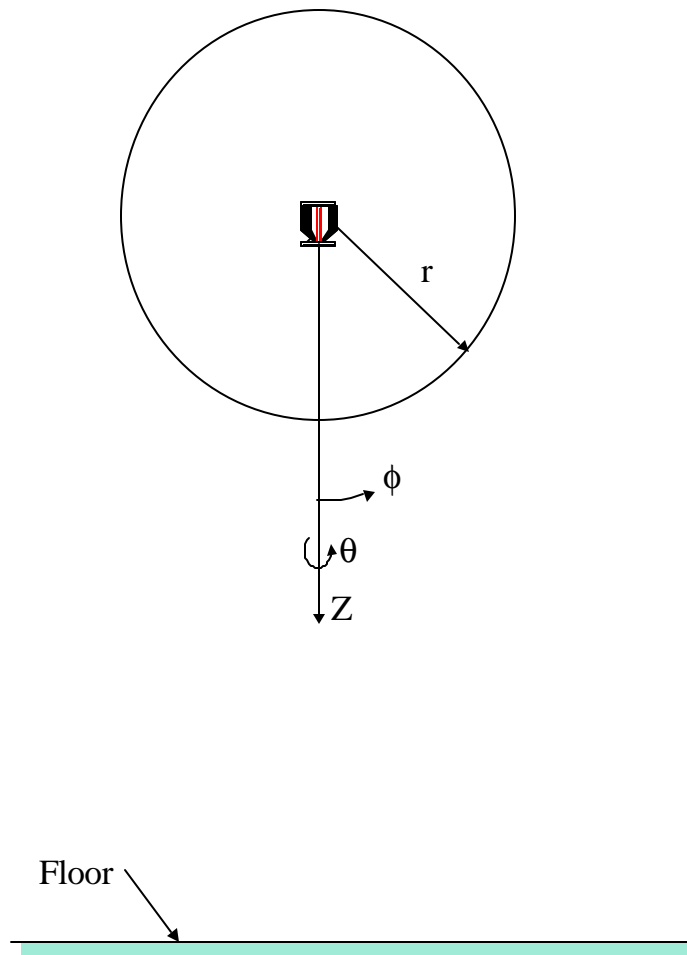
Figure 22. Coordinate System

---

[2] For research purposes the origin location is located at the virtual origin of the droplets (described in section 5.3), but for general engineering purposes the origin can be assumed to be at the sprinkler orifice without materially effecting spray calculation results

3   Sprinklers

Sprinkler designs representing a cross-section of commercially available sprinklers were utilized for these experiments including upright style and nine pendant style sprinklers as shown in Figure 23.   Sprinkler with orifice sizes ranging from 9.5 to 25.4mm were used representing flow coefficients from 40 to 363 $\ell/\min/\sqrt{bar}$, respectively.

Figure 23. Overview of sprinklers used in this study

A standardized naming convention was used for the sprinklers that includes the style, orifice diameter, and sprinkler model. The convention is as follows:

U15A

    └ A, B, C sprinkler model

    Orifice diameter (mm)

    Sprinkler type
    U = Upright
    P = Pendant
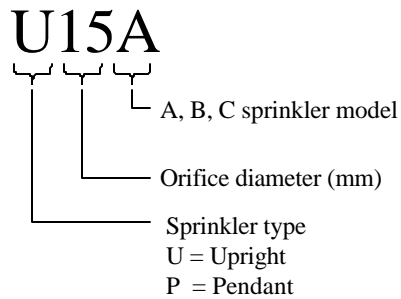
Figure 24 and Figure 25 show representative upright and pendant sprinklers with dimension lines with common dimensional features of sprinklers. Table 6 provides the actual dimensions for the sprinklers used in this study.

I	Deflector Notch Width
J	Deflector Notch Depth
K	Number of Notches
L	Deflector Thickness
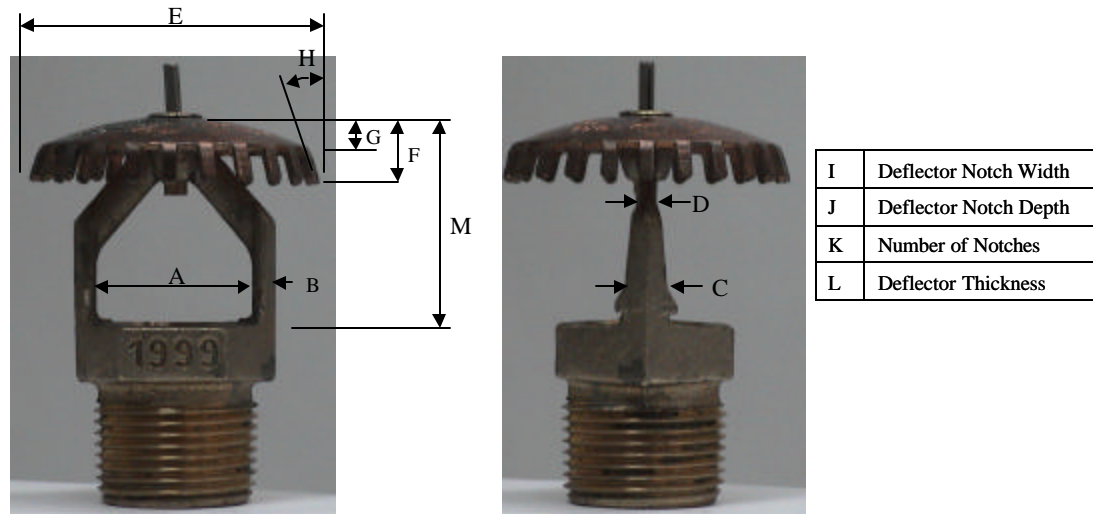
Figure 24. Upright sprinkler with dimensions
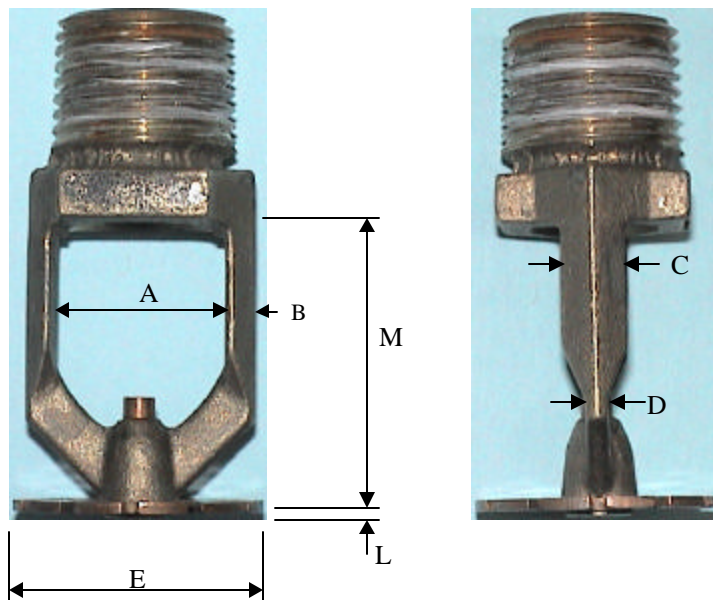
I	Deflector Notch Width
J	Deflector Notch Depth
K	Number of Notches

Figure 25. Pendant sprinkler with dimensions

Table 6. Sprinkler Specifications (all dimensions in mm)

Code	Orifice	K[3]	Frame Arm Distance (A)	Frame Arm Thickness (B)	Frame Arm Width 1 (C)	Frame Arm Width 2 (D)	Deflector Width (E)	Deflector Height (F)	Deflector Rise to Center (G)	Angle (H)	Deflector Notch Width (I)	Deflector Notch Depth (J)	Number of Notches (K)	Deflector Thickness (L)	Height of Deflector over Orifice (M)
P10A	9.5	40	19	4	9	4	30	24	NA	NA	2	4	16	1	33
P11A	10.9	50	18	4	6	3	23	1	NA	NA	2	5	16	1	35
P13A	12.7	79	20	6	8	4	32	1	NA	NA	1	6	16	1	32
P13B	12.7	81	23	6	8	4	27	1	NA	NA	2	6	12	1	38
P14A	13.5	115	25	4	6	3	25	1	NA	NA	3	4	16	1	33
P16A	15.9	161	25	4	6	3	27	1	NA	NA	3	5	16	1	33
P25A	25.4	363	30	10	8	4	44	2	NA	NA	23	14	16	2	62
U16A	15.9	161	25	4	6	3	47	11	6	18	3	5	24	2	34
U16B	15.9	161	24	9	7	5	46	10	4	15	4	5	24	1	43
U25A	25.4	363	30	10	8	4	68	10	6	17	6	7	20	1	64
U25B	25.4	363	30	10	8	4	78	16	15	6	6	6	18	1	63
U25C	25.4	363	30	10	8	4	67	21	9	20	6	4	16	1	67

Note NA = not applicable

---

[3] The Sprinkler orifice coefficient, k, is reported in $\ell/\min/\sqrt{bar}$

4   Laser Sheet Image Results

Figure 26 and Figure 27 show samples of the CCD images of the sprinkler spray for different sprinklers taken during the laser sheet experiments. The CCD images have been processed to reverse the black and white in order to aid in the presentation. The black indicates water droplets.

The different pendant sprinklers shown in Figure 26 have a variety of spray patterns. The flow of water out of the orifice and the frame arms are visible in the upper left corner of the images. For the P13A the ligaments are primarily horizontal in the same plane as the sprinkler deflector. The largest droplets are seen primarily to the side of the sprinkler and almost no large droplets are evident below the sprinkler. The P13B sprinkler has a uniform distribution of droplets at all elevation angles and large droplets are evident throughout the spray. The spray from the two 16mm orifice sprinklers (P16A and P16B) clearly have different water distributions. The P25A sprinkler applies most of the water downward rather than laterally. The P10A sprinkler has a relatively sparse spray directly below the sprinkler. However, regions with large diameter droplets are evident at elevation angles greater than approximately 30°.

54
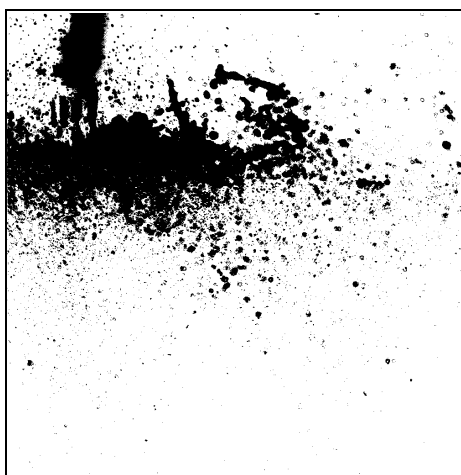
P13A
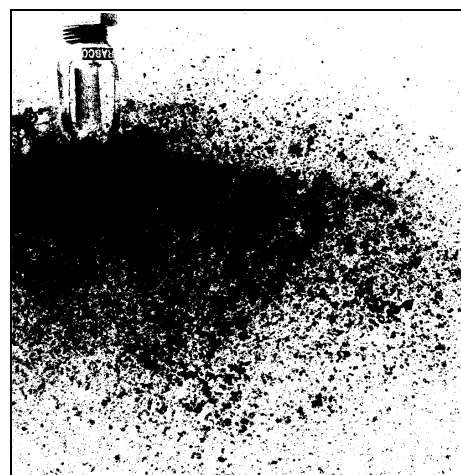
P13B

P16A
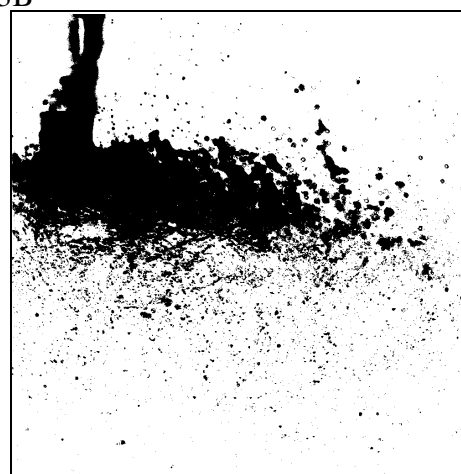
P16B
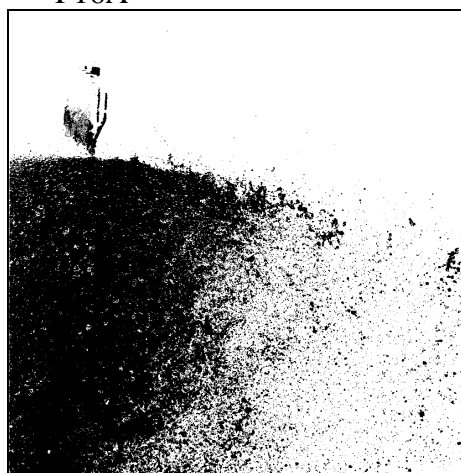
P25A
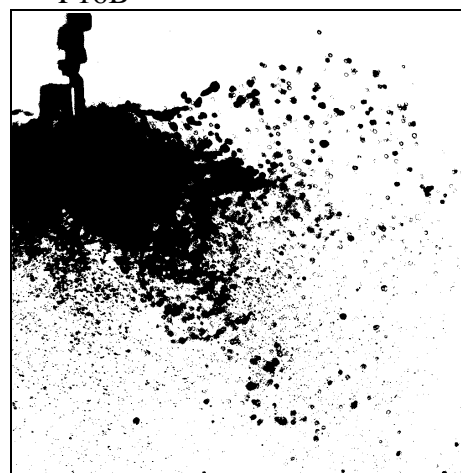
P10A

Figure 26. Laser sheet images – pendant sprinklers

The upright sprinklers in Figure 27 also demonstrate a difference in spray characteristics. The broad vertical line is the water feed pipe with the sprinkler mounted at its upper end. The three 25mm orifice sprinklers were constructed from the same body and different deflectors. The spray from the U25B has a clearly defined upper edge at about ϕ=60° whereas the U25A and U25C have clearly visible spray to much higher elevation angles. The spray from the U16A sprinkler appears to be concentrated at elevation angles from ϕ=30° to 60°.

U25A

U25B

U25C

U16A
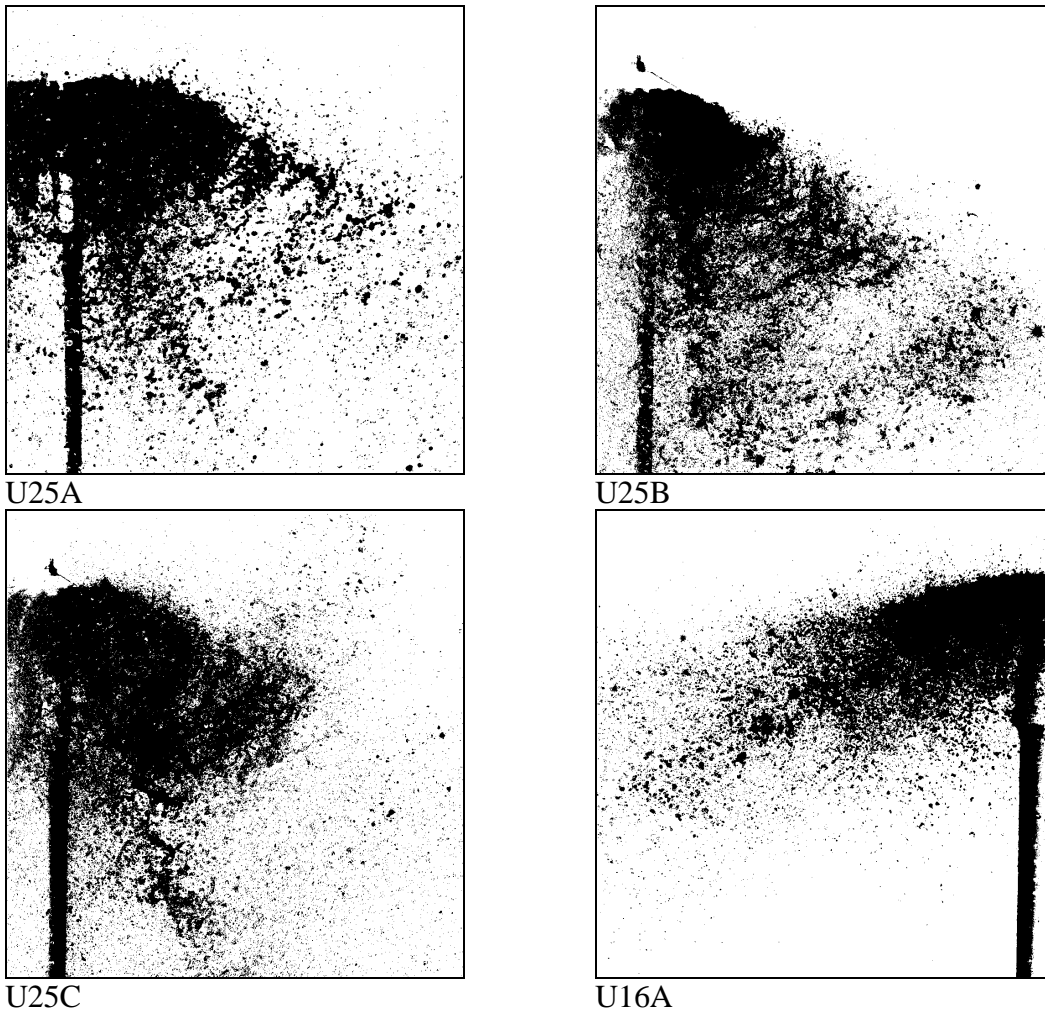
Figure 27. Laser Sheet Images – Upright Sprinklers

It is important to note that the spray looks different for each sprinkler and that the spray characteristics are different in different regions of each spray. For each sprinkler the water density leaving the sprinkler is dependent on the location relative to the sprinkler. The locations where large versus small droplets are visible also depend on the sprinkler design.

5 Spray Velocity

5.1 *Particle Image Velocimetry (PIV)*

The basic principle of PIV is to illuminate a seeded flow-field with two pulses of laser sheet light and record the particle images with a camera. The average displacement of the particles in small regions of the images is calculated using correlation methods. The average velocity in that small region is then calculated by dividing the average displacement by the time between of the laser pulses [35, 36, 37, 38].

PIV images can be recorded with CCD or photographic cameras. Photographic cameras using medium format film provide superior resolution with practical resolutions at least 10 times greater than that of CCD cameras. Photographic film can also provide color information that can be useful in identifying particles of different types, whereas most CCD cameras designed for PIV are limited to gray scale. CCD cameras' greatest advantage is speed. The images from CCD cameras are immediately transferred to a computer. As a result, the quality of the test setup can be assessed very quickly. Photographic film must be processed before image quality can assessed, substantially increasing test setup time. CCD cameras are fast enough to record the image from each laser pulse as a separate image. This allows the use of cross-correlation PIV analysis techniques instead of auto-correlation techniques that must be used for photographic cameras where sequential laser pulses are recorded in the same image [39]. Auto-correlation techniques result in an ambiguity so that although the direction of the velocity

58

is known, its sense is not. Cross-correlation techniques avoid this ambiguity, because each laser flash is recorded in a separate image. The speed of CCD cameras also allows enough tests to be conducted in a reasonable time to allow statistical analysis of the data. A CCD camera was used for the PIV experiments in this study.

Unlike typical applications of PIV where tracer (or seed) particles are added to the flow, we have found that in sprinkler sprays, the droplets themselves can act as tracer particles [40]. The two techniques that can be used to illuminate liquid droplets by a laser sheet are scattering and fluorescence. For scattering untreated water is used. The light that is scattered from the droplets is recorded in the image. But because the amount of scattered light depends on where the laser sheet intersects the droplet, the droplet size cannot be accurately measured. For the fluorescence technique the water is pretreated with a fluorescing dye. When a droplet is illuminated by the laser sheet the entire volume of the droplet is clearly visible even if the laser sheet does not intersect the droplet at its diameter. Although it has been demonstrated that fluorescing droplets provide a more useful signal for determining droplet size [41,42], a scattering illumination technique was used for this study because: 1) it was adequate to measure droplet velocities, 2) a phase Doppler interferometry, PDI, system was available for measuring droplet sizes, 3) the CCD camera resolution did not allow the measurement of the small droplets (less than 200 micron) regardless of the illumination technique.

The PIV cross-correlation analysis was conducting using commercial software provided by the PIV equipment manufacturer [43]. This software controlled the image

acquisition and synchronized the lasers as well as conducting the PIV analysis. The PIV software was operated with the recommended settings with only the number of interrogation regions and timing of the image pairs varied by the user as described below. The PIV analysis was conducted using sub pixel resolution by means of a Gaussian surface fit that resulted in a velocity calculation error of less than 5% for velocities greater than 4 $m \cdot sec^{-1}$. The PIV software was equipped with a variety of tools for cleaning and analyzing the PIV results. These tools were not used because they were not well documented and they did not allow a sufficient level of control.

Each image was subdivided into a series of interrogation regions in the form of a Cartesian grid. The best size for the grid was determined by trial and error. As the size of the interrogation region decreased, the number of droplets in each interrogation region decreased. Too few droplets in the interrogation region resulted in the inability of the cross-correlation to calculate a displacement. For most sprinklers a 19 pixel by 20 pixel grid with a spot size of 64 was found to consistently produce acceptable results. This corresponds to an interrogation region overlap of 160%. For the largest orifice sprinklers, 25mm, it was found that a grid of up to 25 pixels by 25 pixels with a spot size of 64 would provide good results. This corresponds to an interrogation region overlap of 128%.

The timing of the laser pulses was chosen to maximize the amount of information gained from each image pair. It was found through experimentation that an average drop displacement 1 to 10 pixels between images in a pair produced good vectors. This

amount of displacement could be obtained with laser pulse timing in the range of 150μs to 300μs depending on the velocity of the spray. The timing between the laser pulse pairs was set to assure that the same droplets would not be visible in consecutive image pairs.

Figure 28 provides an example of the image pairs and the vectors calculated using PIV for a test conducted with P10A sprinkler at an azimuthal angle $\theta=30°$ with respect to the frame arms and a water pressure of 48 kPa. The two images were taken 150 μs apart. The sprinkler is clearly visible in the upper left quadrant. Close study of the two images shows that the droplets are slightly displaced away from the sprinkler in the second image. The vector plot shows that the fastest spray is moving downward at an angle of about 45° from the sprinkler. The spray below the sprinkler is moving straight down at a slightly slower velocity. The droplets at the elevation of the sprinkler and above are moving at a much slower velocity.
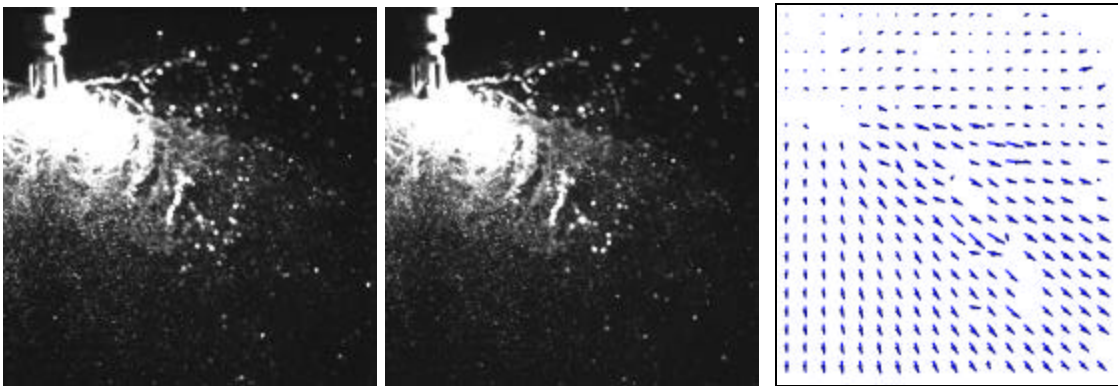
Figure 28. Two sequential CCD images and the resulting PIV vector field for a P10A sprinkler at an azimuthal angle $\theta=30°$ and a water pressure of 48 kPa

5.2   Vector Cleaning Techniques

Because the cross-correlation technique used for particle image velocimetry is purely mathematical in nature, it does not do a "reality check" on the physical domain for which the calculation is being conducted. As a result, the velocity vectors calculated by the particle image velocimetry are sometimes wrong. Non-physical velocities commonly occur in regions where there are not enough droplets for cross correlation analysis to be accurate. In these sparse regions of the flow, the statistical velocity may be based on one or two droplets that may not be statistically related to one another. For instance, if there are only two droplets in an interrogation region in the first image and both leave the region while another droplet enters in the seconds image, the cross correlation will provide an erroneous displacement. For this reason, the vectors calculated by the PIV methodology must be individually evaluated for their accuracy. The resulting weeding out of the bad vectors is called "Vector Cleaning".

Figure 29 shows an example of the raw vectors that are produced by the PIV cross-correlation algorithm. The vectors are from two sequential images in a test with a P13 sprinkler at 59 kPa water pressure. The location of the sprinkler corresponds to the upper left quadrant of the image and can be located by extending all the vectors back to a common origin. The vector plot in Figure 29 has four obviously bad vectors. The bad vectors are of a different magnitude than the typical vectors in the plot, and the bad vectors are oriented in a different direction than the nearby vectors.
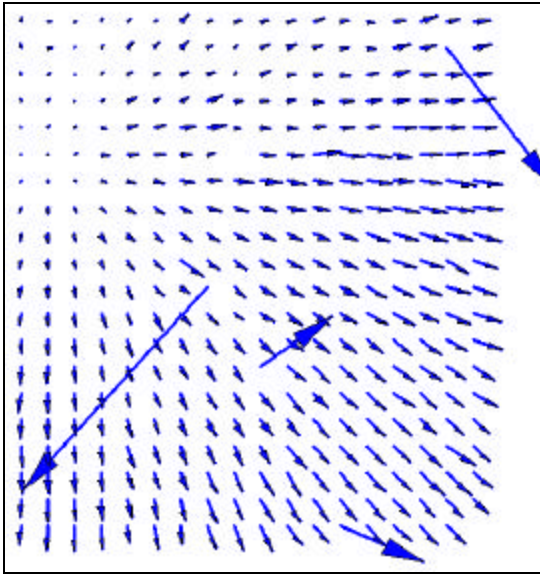
Figure 29. PIV vector field before vector cleaning

Although manual deletion of bad vectors from the vector field is possible, the large number of images makes manual cleaning overwhelming. Consequently, three techniques for automatically cleaning the vectors were used. Two of the cleaning techniques utilized the magnitude of the vectors, and the third used the direction of the vector.

The first and simplest vector cleaning technique was to delete any vectors with magnitudes that were unrealistically high. The cutoff level of the velocity magnitude was determined by calculating the median velocities for each vector field for a series of tests using a variety of sprinklers and pressures. This analysis showed the median velocities were typically in the range of 0 to 12 $m{\cdot}s^{-1}$. Using the results of this preliminary analysis as a basis, vectors greater than 18 $m{\cdot}s^{-1}$ were eliminated from the vector field.

The second vector cleaning technique was made possible because 200 PIV images were obtained for each experimental condition. Therefore, 100 vector measurements were available for each PIV interrogation region. Vectors were eliminated with magnitudes that were more than 2 standard deviations from the mean at each location. This vector cleaning technique was judged valid because visual observation of the vector fields did not show wide variations in velocity. This vector cleaning technique was only used after the unrealistically high velocities were removed using the first cleaning technique to avoid problems that might occur due to several bad vectors localized in one region.

The third vector cleaning technique was based on the assumption that the droplets near the sprinkler, where the measurements were made, would always be moving away from the sprinkler. For this third technique, the direction of a vector was compared to the direction of a line drawn from the center of the sprinkler orifice to the center of that PIV interrogation region. If the direction of the velocity vector differed from the line to the orifice by more than ±45°, the velocity vector was deleted.

All three of these vector-cleaning techniques provided acceptable results. In the analysis of the spray within 1m of the sprinkler, the first and third techniques were the only cleaning techniques that were necessary. After the first and third techniques were used, the second technique did not remove any additional vectors. For spray analysis more than 1 meter away from the sprinkler, all three cleaning techniques were necessary to remove all bad vectors.

The number of bad vectors removed by the vector cleaning technique depended on both the water flow rate through the sprinkler and the location of the velocity vector in the flow field. In locations where there were high concentrations of water, the number of bad vectors was typically less than 10%. In regions at the edges of the spray field, the number of bad vectors was as high as 80%. Outside the spray field, such as regions above the deflector, the rejection rate approached 100% since no droplets were present. Any vectors remaining in these regions were eliminated manually.

After the vector cleaning process was completed for the 100 vector sets obtained for ach condition, the ensemble average droplet velocity was calculated for each interrogation region using the remaining vectors. This array of average vectors was then used as the velocity field for subsequent analysis for that test configuration.

In order to understand the variations in measured velocity, the standard deviation of the ensemble average at each vector location was calculated. For example, the U25A sprinkler at 103 kPa had an average standard deviation of 0.39 m·sec^{-1}. For the U10A sprinkler at 220 kPa, the average standard deviation was 0.67 m·sec^{-1}. The standard deviation was found remain relatively constant at magnitudes less than 0.7 m·sec^{-1} in almost all locations in the spray for all sprinklers regardless of sprinkler type and spray velocity. In other words, if the standard deviation in the velocity was 0.5 m·sec^{-1}, the standard deviation would remain at approximately 0.5 m·sec^{-1} regardless of whether the spray velocity a that location was 1 m·sec^{-1} or 10 m·sec^{-1}. The standard deviation was

found to have the greatest magnitude near the edges of the spray envelope and smaller in dense portions of the spray.

The variations in velocities at individual locations were produced by a combination of real variation in the spray velocity and by measurement errors. The average standard deviations were found to increase as the water pressure increased as shown by the examples above. Since increases in standard deviation coincide with the changes in test parameters it is logical to assume that much of the observed standard deviation is a product of real variations in the velocities.

5.3 Virtual Spray Origin

Initial review of the spray velocities (e.g. Figure 28 and Figure 29) suggests that the sprinkler spray could be treated as a nearly radial flow with the origin located at the sprinkler. The velocities were converted to the spherical coordinate system by converting the Cartesian components of the velocities to radial and angular velocity components. The radial, u_r, and angular components, u_ϕ, of velocity were calculated in $\phi=3°$ increments with the center of the orifice as the origin and using linear interpolation between Cartesian PIV grid and the new polar grid at any particular elevation angle.

Figure 30 shows a vector plot of u_r and u_ϕ, 200mm from the orifice of the P10A sprinkler at an azimuthal angle $\theta=0°$ and a water pressure of 221 kPa. The axes represent the vertical and horizontal position in the PIV image. The u_r vectors are the long vectors.

The u_ϕ velocities are represented by the very short vectors orthogonal to and originating from the base of the u_r vectors.
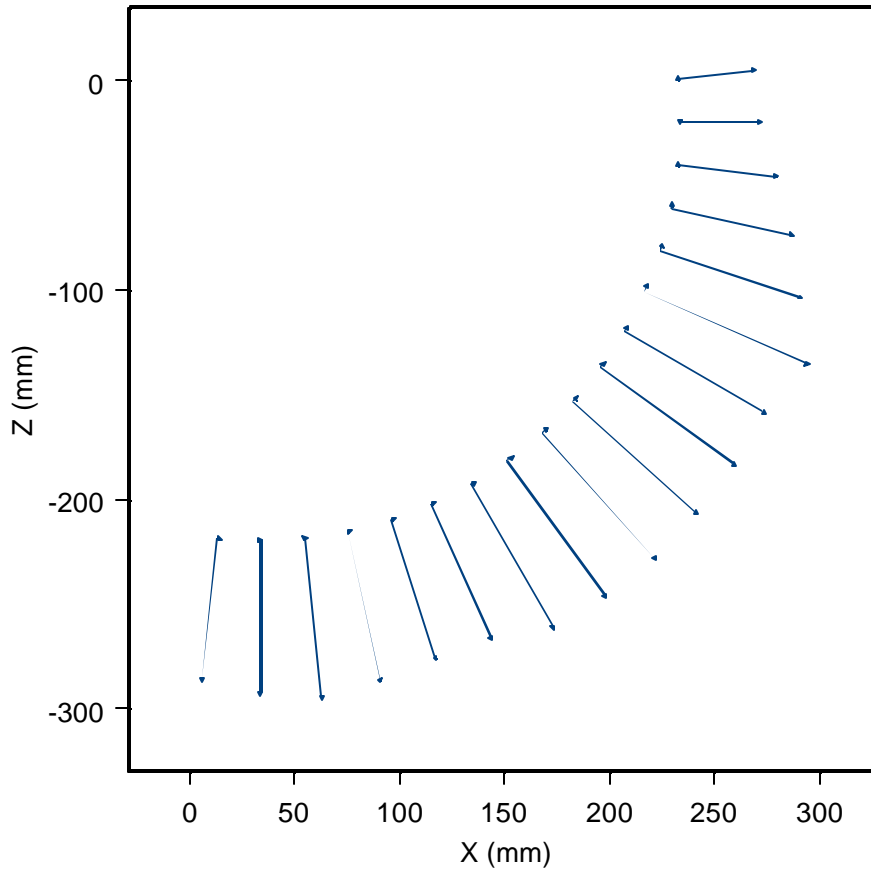
Figure 30. Vector Plot of u_r and u_ϕ for P10A sprinkler at 221 kPa

Evaluating the results of the conversion of the velocities to the spherical coordinate system (e.g. Figure 30) reinforces the idea that the droplet flow is primarily radial because the magnitude of the radial component is always much greater than the ϕ component.

Being able to treat the velocity as a purely radial flow allows later analysis to consider the sprinklers as point sources. This simplification to point sources greatly

reduces the complexity of sprinkler spray analysis. For this reason, the conversion from the PIV Cartesian velocities to the velocities in polar form was conducted in a manner that would maximize the radial components of the velocity and minimize the angular components using the following procedure.

A value, E, was calculated that characterized the magnitude of the angular components of the velocities

$$E(r) = \sum_f \sum_q u_f^2 \tag{5.1}$$

where u_f was summed for one radius (typically 0.2m) for all velocities at all azimuthal angles, θ, and elevation angles, ϕ.

The origin location was then iteratively shifted along the axis of the orifice until the location with the minimum angular velocity components as exemplified by minimum E, was found. This location where the angular component of velocity was minimized was defined as the Virtual Spray Origin.

The virtual spray origin was always located between the orifice and the deflector for pendant sprinklers and between the orifice and 0.05m above the deflector for upright sprinklers. The radial velocities calculated from the virtual spray origin were at least 20 times larger than angular velocities except in the regions with small velocity. This indicates that the flow is nearly purely radial near the sprinkler.

The radial spray velocities parallel to the frame arms of the P10A sprinkler are shown in Figure 31. The Figure shows radial velocities calculated at 7 radial distances ranging from 0.05m to 0.2m from the virtual spray origin. The radial velocities calculated at all radii demonstrate a dependence of u_r on the elevation angle, ϕ, as evidenced by the changing lengths of the vectors with position. The dependence of the radial velocities on radial position is stronger near the sprinkler than further away. Likewise there is some dependence of the radial velocity on radial position near the sprinkler, but less further from the sprinkler. The region with the strong radial dependence is where the water is breaking up into drops as shown in Figure 26. After the water has broken into a fully developed spray, the radial velocities are fairly uniform with respect to radial distance. For the sprinklers in this study, the change in the radial velocity was negligible for radial distances greater than 0.2m.
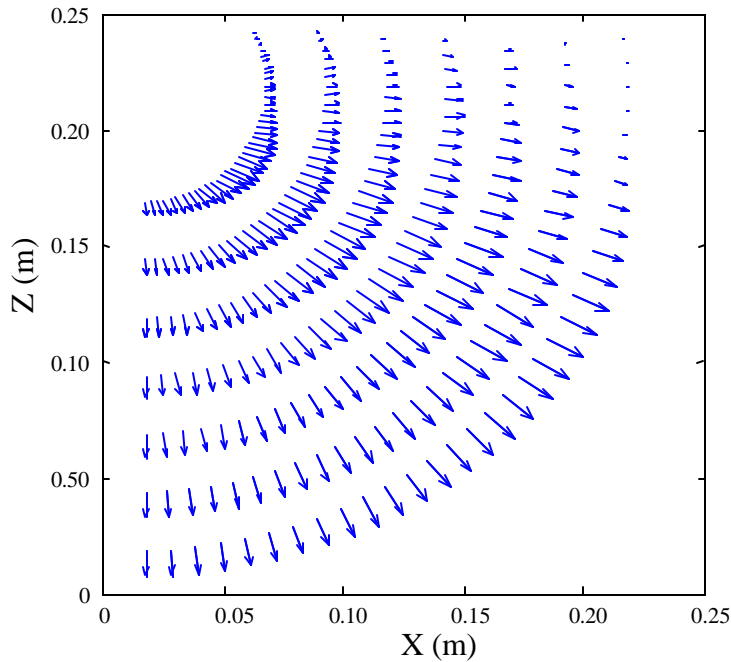
Figure 31. Vector plot of radial velocities of the P10A sprinkler at φ=0°. The radial velocities are shown at r = 0.05, 0.075, 0.100, 0.125, 0.150, 0.0175 and 0.200m from the virtual spray origin.

5.4 Radial Velocities

The radial velocity results measured using PIV are presented in a polar chart format, an example of which is shown in Figure 32 for a P13B sprinkler. This chart format was chosen because it provides an intuitive method of representing the results. The small circle in the center of the chart represents the virtual spray origin. The polar chart extends from an elevation angle $\phi=0°$ directly below the sprinkler to $\phi=120°$ slightly above and to the right of the sprinkler. The curves indicate the magnitude of the radial velocity from 0 to 14 $m \cdot s^{-1}$.

Figure 32 shows the radial velocity profile at an azimuthal angle of $\theta=30°$ from the sprinkler frame arms. At this azimuthal angle the sprinkler exhibits a bimodal velocity profile with local maxima of 11.0 and 10.9 m·s^{-1} at elevation angles of $\phi=36°$ and $\phi=71°$ respectively. The velocity varies by more than a factor of 3 from minimums of 5.4 and 3.5 m·s^{-1} at $\phi=0°$ and $\phi=99°$, respectively.
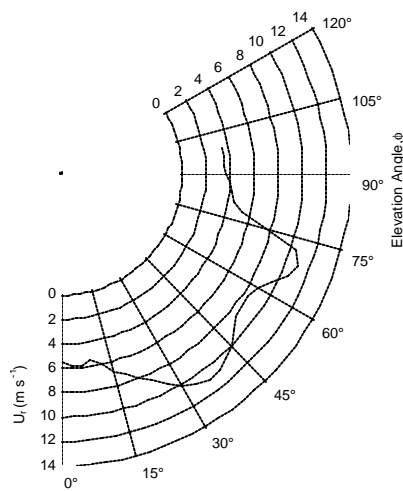
Figure 32. Radial Velocity at Azimuthal angle $\theta=30°$ for Sprinkler P13B at 131 kPa

The radial velocities of the pendant and upright sprinklers at a radial position 0.2m from the virtual origin are shown in Figure 33 and Figure 34, respectively. Each graph in Figure 33 and Figure 34 show 19 sets of radial velocities corresponding to azimuthal angles $\theta=0°$, 5°, 10°, ….., 90°, for 12 different sprinkler and pressure conditions. Presenting all the data for all azimuthal angles makes the graphs a bit cluttered, but it provides a quick visual representation of the sprinkler flow in terms of the general velocity profile and the spread of the data with respect to the azimuthal angle.

P10A (221 kPa) P13A (59 kPa) P13B (131 kPa)

P14A (48 kPa) P16A (48 kPa) P25A (103 kPa)
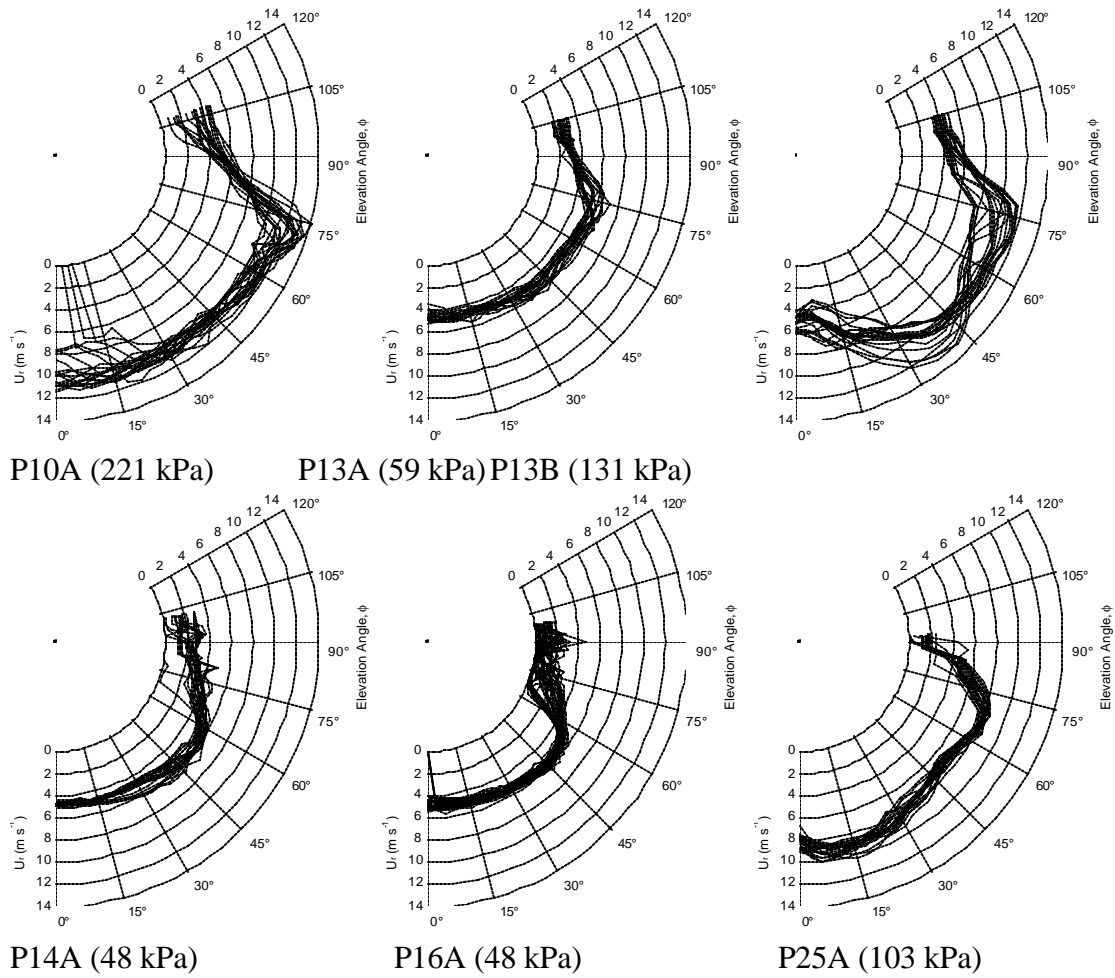
Figure 33. Radial velocities of pendant sprinklers
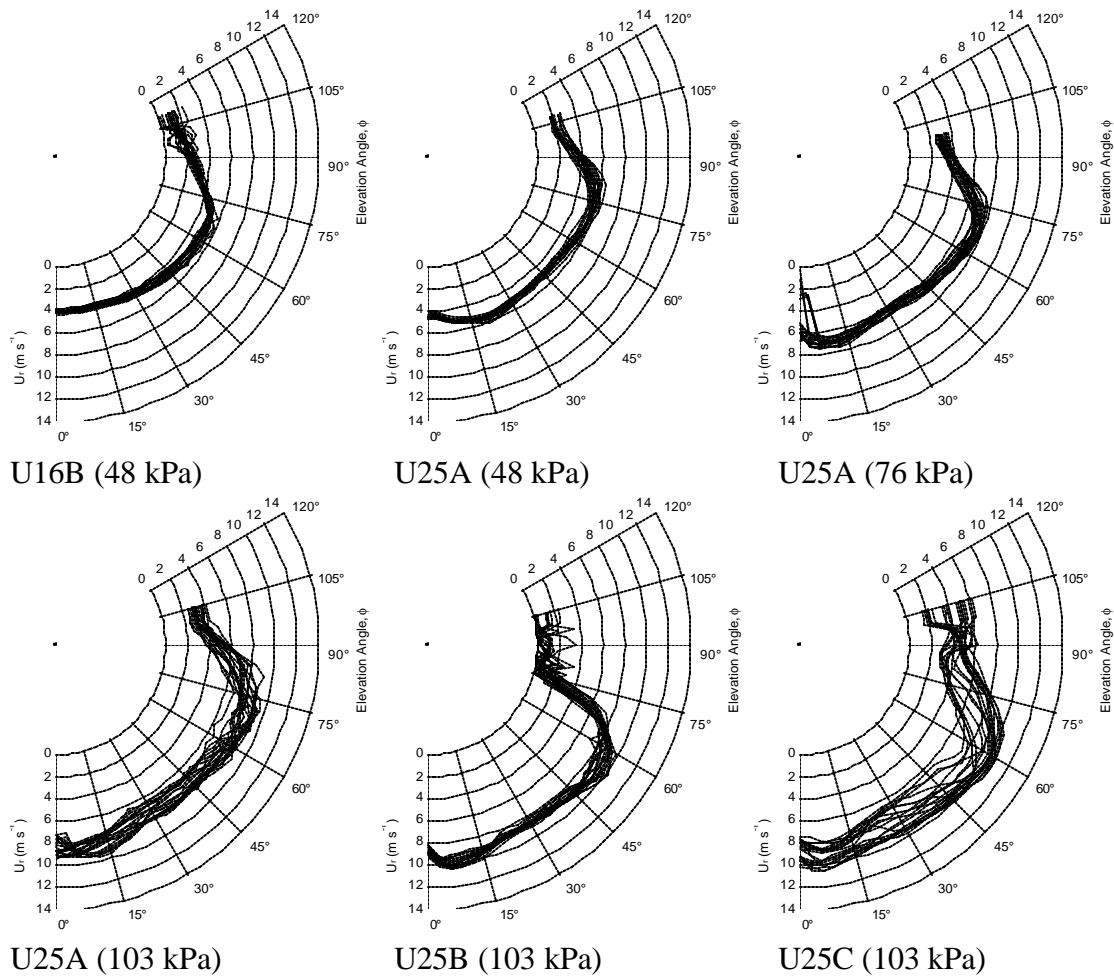
Figure 34. Radial velocities of upright sprinklers

From Figure 33 and Figure 34 it is clear that there is substantial variation in the radial velocity profiles. The shapes of the velocity profiles vary with sprinkler type [pendant (P) or upright (U)], pressure, and deflector design. For instance, some sprinklers have a bimodal velocity profile (P13B), while others do not. Some sprinklers display substantial variation in the radial velocity profile with azimuthal angle θ (P13B and U25C), while others appear to have a nearly axisymmetric spray (U16B and U25A). In most cases, the radial spray velocity diminishes above an elevation angle of $\phi = 75°$,

although in some cases this occurs at a smaller elevation angle (P14A, P16A, U25B). In most cases, the radial velocity directly below the sprinkler is near the maximum velocity. However, some sprinklers (P13B, P25A, U25A, U25B and U25C) have a somewhat lower velocity at $\phi = 0°$. Several different approaches to analyzing the sprinkler spray radial velocity profiles shown in Figure 33 and Figure 34 will be discussed in the following sections.

5.5 Maximum and Average Spray Velocities

The maximum radial velocity over all of the sprinklers ranged from 5.8 to 14.1 $m \cdot s^{-1}$. The maximum velocity was calculated using two methods. The first method was to simply find the maximum velocity. The second method was to find the maximum average velocity using a three point running average of the radial velocities as a function of elevation angle. The purpose of the running average was to eliminate effects from single non-representative values. The difference between the two methods averaged only 2.8%.

The maximum and average maximum velocities for sixteen experiments are shown in Figure 35. The bar chart shows the velocity on the vertical axis and the tests located on the horizontal axis. The tests are ordered by sprinkler type, then orifice size and then by water pressure. The pendant sprinklers are grouped on the left and the upright sprinklers on the right. For example the first three sets of data represent the

maximum velocities for the P10A sprinkler at water pressures of 48, 138, and 221 kPa. This blocking method of ordering the data facilitates the visual identification of trends.

Figure 35 reveals several facts about the maximum radial velocities. There is a difference between the maximum and average maximum although it is always small. This indicates that localized areas of high velocity do not exist. As expected the maximum velocity increases with pressure as shown by the three pressures tested with the P10A and the three pressures with the U25A sprinklers. The maximum velocity is effected by the deflector as demonstrated by the tests of the U25A, U25B, and U25C sprinklers tested at 103 kPa.
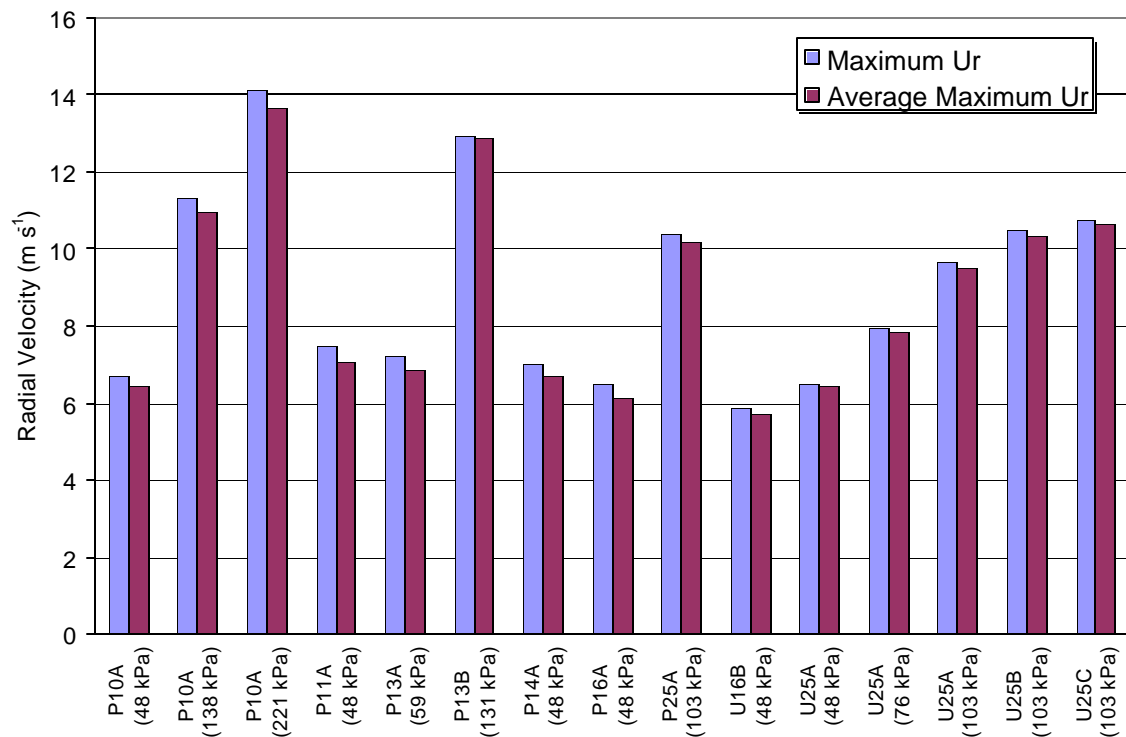
Figure 35. Maximum Velocities

The location of the maximum velocities was also considered. Figure 36 shows the elevation angle where the maximum and average maximum velocities were measured. It is interesting to note the wide range of elevation angles, $6°=\phi=78°$, where the maximums were observed. Despite their very different designs, the large range of elevation angles occurred for both upright and pendant sprinklers with no clear difference between the elevation angles of the pendant and upright sprinklers. It is also worth noting that the elevation angle of the maximum and average maximum velocities closely coincided for all experiments, which again confirms that localized areas of high velocity do not exist.

A functional relationship that can be observed in Figure 36 is between elevation angle of maximum velocity and the pressure and sprinkler style.   For the pendant style P10A sprinkler that was tested at pressures of 48, 138 and 221 kPa, the elevation angle of the maximum radial velocity clearly increases with increasing pressure. For the upright style U25A sprinkler that was tested at 48, 76 and 103 kPa, the elevation angle of the maximum velocity trends downward as the pressure increases. This effect could be caused by the deflector "deflecting" the spray more as the water velocity increases. For example, in an upright sprinkler the water jet from the orifice is initially moving vertically upward. When the water jet impacts on the deflector almost all of the upward momentum in the jet is deflected horizontally and downward.   What these test results show is that as the water pressure increases, the deflector becomes more efficient at reversing the direction of the spray. As a result, for upright sprinklers the elevation angle

for the maximum velocity moves downward and for a pendant sprinkler the elevation angle for the maximum velocity moves upward.
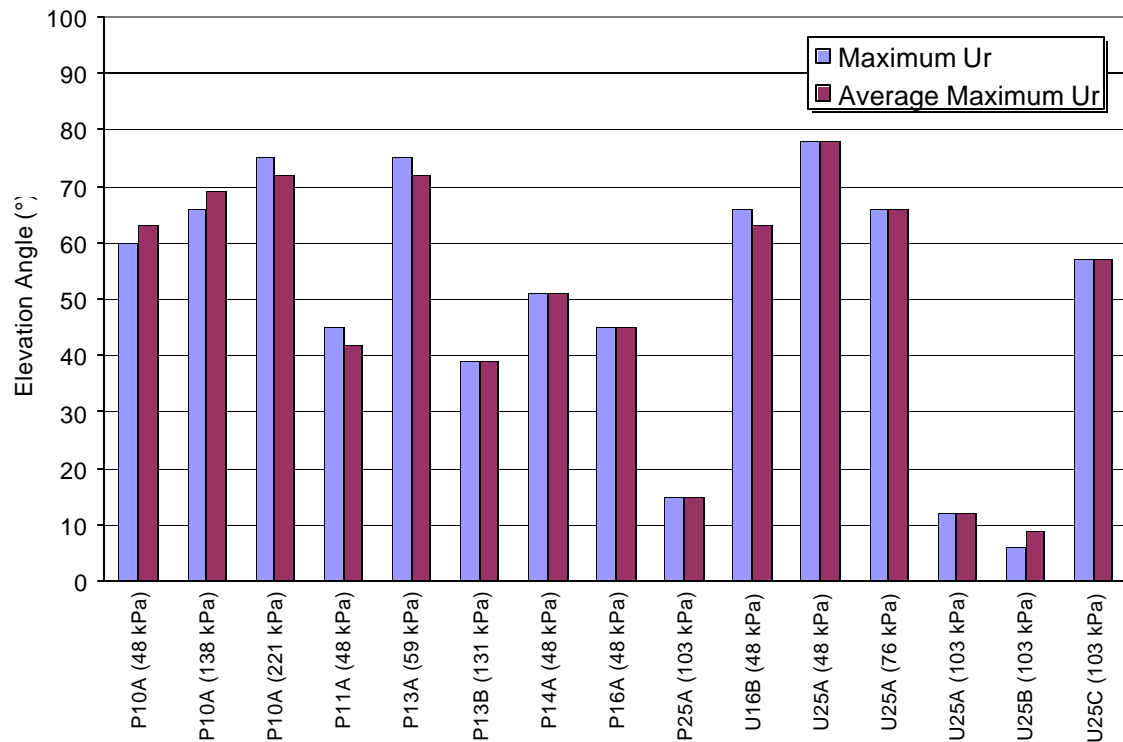
Figure 36. Elevation angle of maximum velocities

The azimuthal location with respect to the sprinkler frame arms of the maximum velocities is shown in Figure 37. The location of the maximum velocities range from parallel, $\theta=0°$, to nearly perpendicular, $\theta=90°$, to the frame arms. There is again no clear distinction between upright and pendant style sprinklers. In two cases (P10A/138 kPa and U25A/48 kPa), there are differences between the maximum and average maximum locations, which upon closer study proved to be caused by a large region of nearly uniform radial velocity. Thus, the maximum velocity is not strongly dependent on azimuthal position in these two cases.
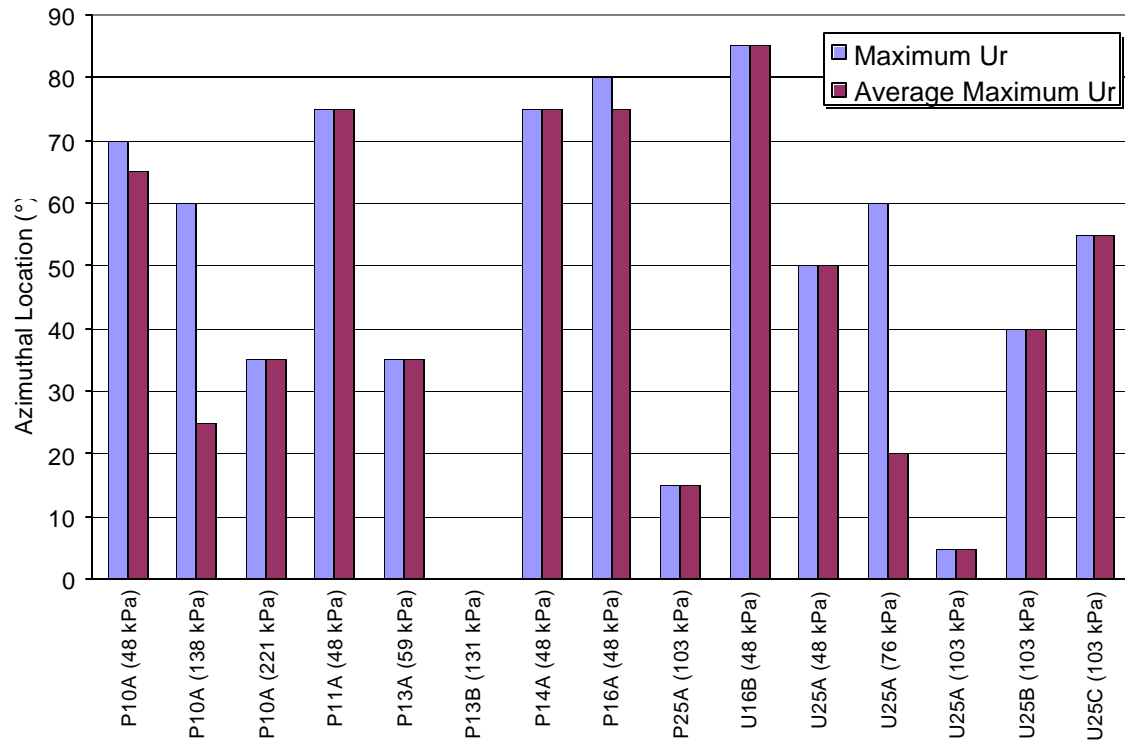
Figure 37. Azimuthal Location of Maximum Velocities

The average velocities in the flow field were also evaluated. The average velocity was calculated using a weighted average of the non-zero velocities. The average was weighted using the azimuthal arc length at the different elevation angles to account for the fact that the azimuthal velocity near $\phi = 0°$ corresponds to only a small portion of the spray while that at $\phi = 90°$ accounts for a very large portion.

The average velocities are presented along with the maximum velocities and the velocity of the water through orifice in Figure 38. The orifice velocity is included in the analysis because it is the initial velocity of the water before the water impacts on the deflector. The orifice velocity is also the only velocity in the system that can be calculated using known characteristics of the sprinkler. The orifice velocity is the

average water velocity through the sprinkler's orifice and is calculated by dividing the volumetric flow rate by the area of the orifice. The average velocity is always less than the other two velocities.

The orifice velocity is higher than the maximum velocity in ten of the sixteen experiments. The fact that the maximum radial velocity of the droplets is sometimes higher than the orifice velocity for some pendant sprinklers was not expected. The physics of the flow suggest that the deflector will significantly reduce the water jet's momentum, which should reduce the average water velocity. The fact that locations exist with velocities higher than the orifice velocity suggests that the deflector creates localized regions of high pressure and velocity. An example of how this might occur is when the water is moving from the center of the deflector of a pendant sprinkler toward the outer edge and meets the edge of the deflector. A localized region of high pressure would be expected to form behind the deflector. The water must either change direction to pass the deflector, or when a notch is present, it would be accelerated through the notch.
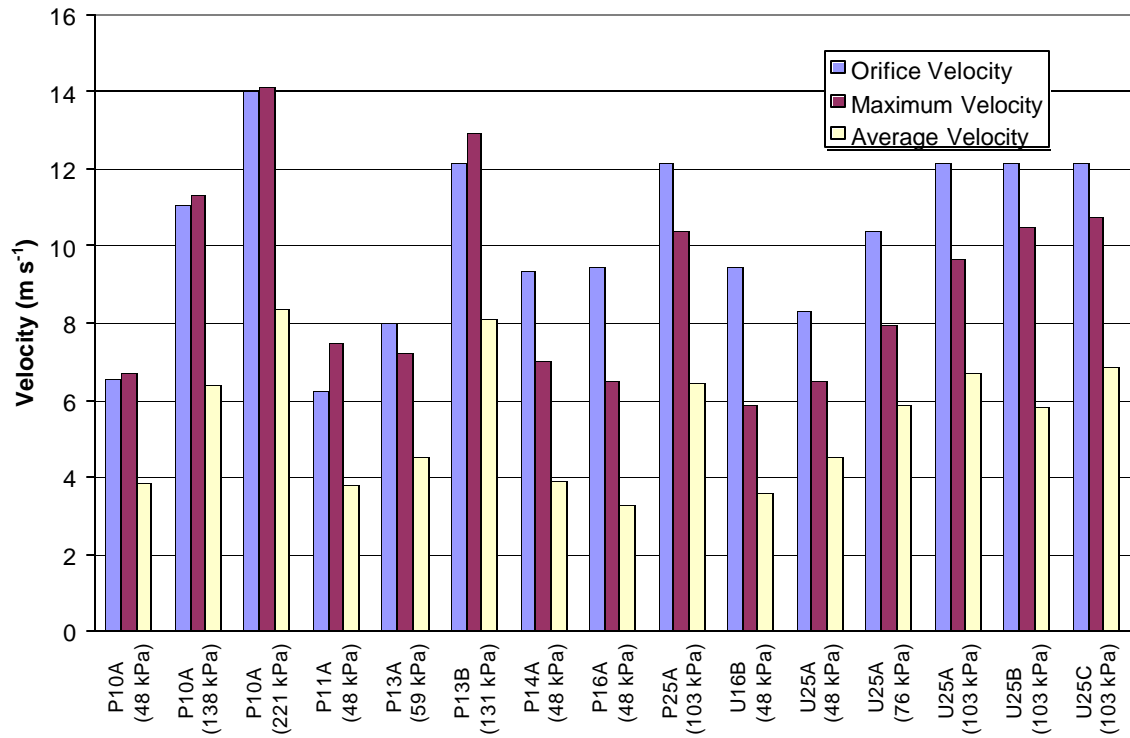
Figure 38. Maximum, Average and Orifice Velocities

In order to determine if there is a functional relationship between the different velocities, the ratios of the velocities were computed. Figure 39 presents the ratios of 1) Maximum Velocity to Orifice Velocity, 2) Average Velocity to Orifice Velocity and 3) Maximum Velocity to Average Velocity.
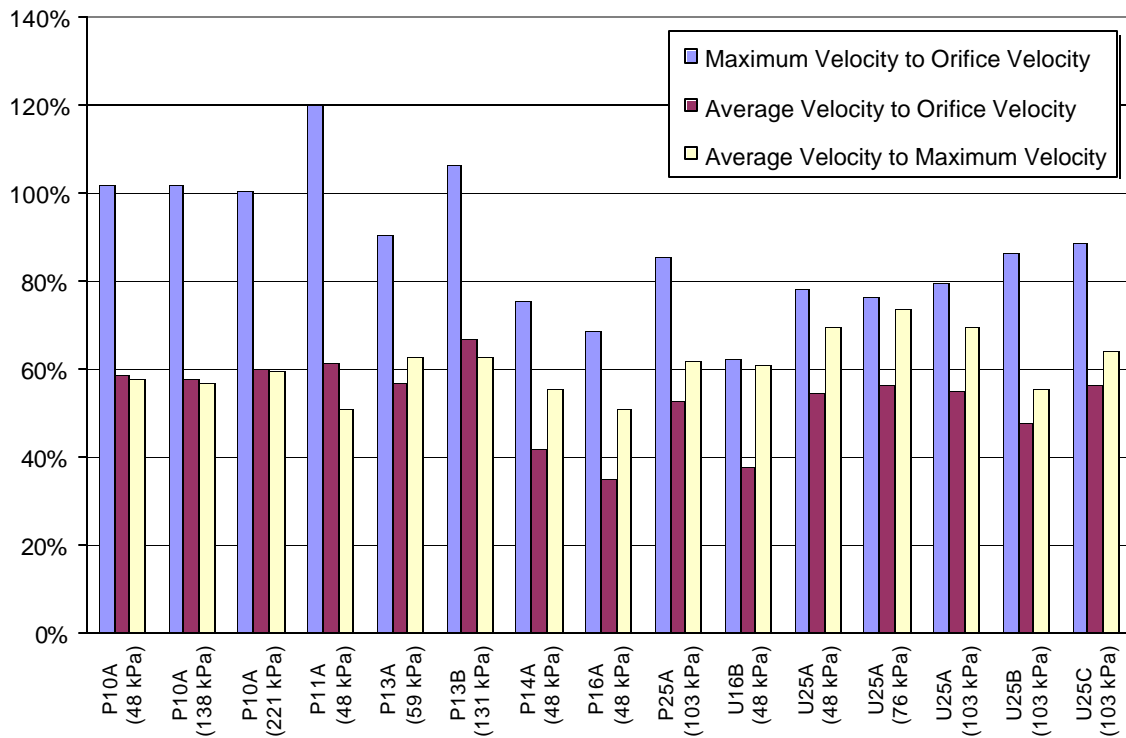
Figure 39. Ratios of Velocities

The ratio of the average velocity to the maximum velocity had a mean of 61% and a standard deviation of 6%. A statistical test demonstrated that the data is randomly distributed about the mean with a normal distribution.

The ratio of the maximum velocity to orifice velocity reveals several interesting items. Initial review of Figure 39 reveals the ratios are near 100% for many pendant sprinklers and none are near 100% for upright sprinklers. A t-test comparison of the ratios for pendant sprinklers versus upright sprinklers at a 95% confidence interval indicates that there is a significant difference between this ratio for pendant and upright sprinklers.

The ratio of the average velocity to the orifice velocity had an overall average of 53% with a standard deviation of 8%. The mean ratios for pendant versus upright sprinklers were 54% and 51%, respectively, with an overall standard deviation of 8%. A t-test indicated that there was not a significant difference between pendant and upright sprinklers for this ratio. This result suggests that a quick estimate of the average radial droplet velocity for a sprinkler would be about half of the velocity at the orifice.

While these three ratios do not demonstrate strong functional relationships between sprinklers, they are nearly constant for individual sprinklers. For example, the P10A sprinkler was tested at three water pressures and the three ratios remain essentially constant. The U25A sprinkler was also tested at three water pressures and has similar ratios for the three pressures.

There is evidence that the constant ratio behavior for individual sprinkler is influenced by the sprinkler deflector. Comparison of the ratios for the U25A, U25B, U25C and P25A sprinklers, which were constructed from the same sprinkler bodies and different deflectors, show substantial variation in the ratios. Likewise, the ratios for the P16A and U16B sprinklers, which were also constructed from the same sprinkler body, also show variation in the ratios.

5.6   Effect of Pressure on Radial Velocity

Tests were conducted to evaluate the effect of water pressure on the water spray characteristics. An example of the effect of water pressure on radial velocity is shown in

Figure 40. Figure 40 presents the average velocity as a function of pressure for the P10A

and U25A sprinklers, respectively. The average velocity is the ensemble averaged

velocity profile over all of the measurements at various azimuthal angles. As expected,

the velocity of the spray increased as the water pressure increased. Note the similar shape

of all three profiles for each sprinkler.

P10A   U25A
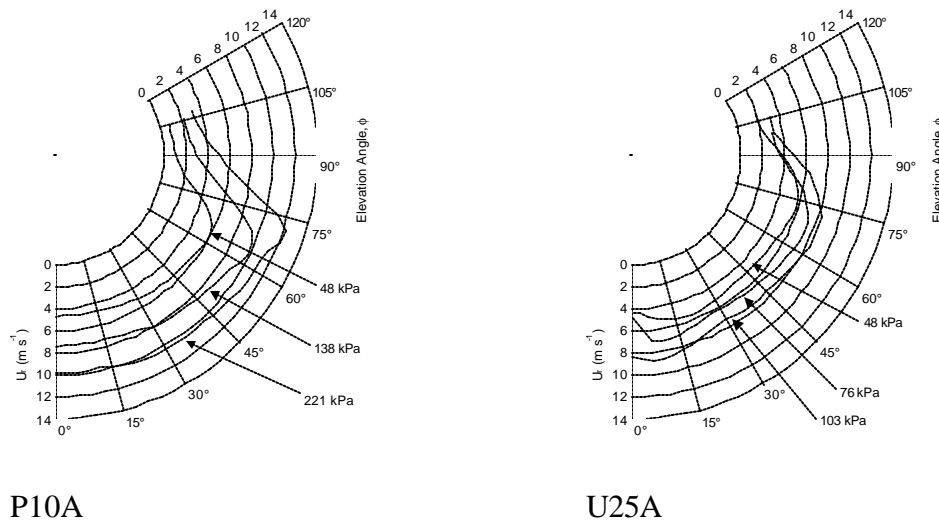
**Figure 40. Average Spray Velocities for the P10A and U25A sprinklers at three
           pressures**

A closer examination of the radial velocities as a function of pressure at

individual azimuthal angles is presented in Figure 41 for the P10A sprinkler at $\theta=0°$, $30°$,

and $60°$. As expected, the overall shapes of the velocity profiles are slightly different at

the different azimuthal angles. However, it is clear that the shapes of the radial velocity

profiles at the three pressures is similar at any particular azimuthal angle. To illustrate

this, at $\theta=30°$ all the velocity profiles have a minimum at $\phi=105°$ and reach a maximum

at approximately $\phi=75°$. The radial velocities then decrease slightly until the point

directly below the sprinkler.

$\theta=0°$ $\theta=30°$ $\theta=60°$
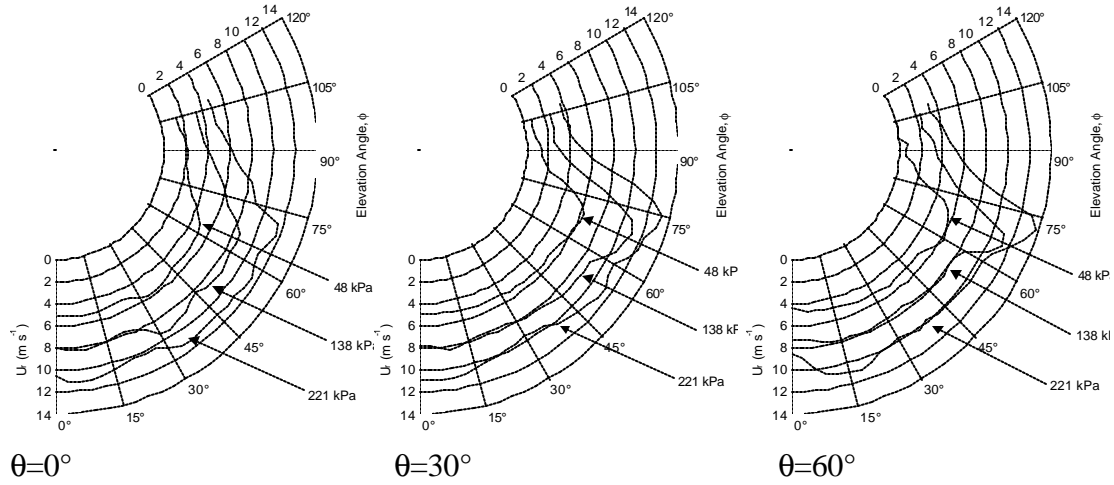
Figure 41. Radial Velocities for P10A Sprinkler at Three Pressures

For the range of pressures used in real world applications of sprinklers, the flow

rate through the sprinkler orifice has been found to be proportional to the square root of

the pressure [44]. This functional relationship is derived from Bernoulli's equation, and

has been confirmed over many experiments by various listing agencies. Using

Bernoulli's equation, the relationship between the velocity and pressure is

$$U \propto \sqrt{\frac{P}{r}} \tag{5.2}$$

If a functional relationship exists between the spray velocity and the water

pressure, a reasonable first approximation would be to assume that the spray velocity

follows the same functional relationship as the orifice water velocity. Therefore, the

radial velocities for the experiments utilizing different water pressures was

nondimensionalized as

$$\bar{U}(\boldsymbol{f},\boldsymbol{q}) = u_r(\boldsymbol{f},\boldsymbol{q})\sqrt{\frac{\boldsymbol{r}}{P}} \qquad (5.3)$$

where $\bar{U}(\boldsymbol{f},\boldsymbol{q})$ is the nondimensionalized velocity at angle ϕ and θ, $u_r(\boldsymbol{f},\boldsymbol{q})$ is the radial velocity at angle ϕ and θ, $\boldsymbol{r}$ is the density of water, and P is the water pressure.

To evaluate if the relationship proposed in (5.3) is valid, the velocities for the P10A and U25A sprinklers at three different water pressures were converted to nondimensional form. The three non-dimensional experimental velocities, $\bar{U}(\boldsymbol{f},\boldsymbol{q})$, for each pressure at each ϕ and θ location were very similar. For the P10A and U25A sprinklers, the average standard deviation of $\bar{U}(\boldsymbol{f},\boldsymbol{q})$ was 7% and 6%, respectively. The correlation coefficient calculated for each data set was 97% and 99% for the P10A and U25A sprinklers, respectively.

Representative examples of the velocity nondimensionalized by the water pressure for the P10A and U25A sprinklers at $\theta = 45°$ are shown in Figure 42. Each graph shows four sets of data. The data closest to the origin is the standard deviation, σ, for the pressures measured at the elevation angle. The nondimensional velocity profile as a function of elevation angle, $\bar{U}(\boldsymbol{f})$, is represented by the dark curve. The two curves on either side of the velocity profile represent the error for the different pressures for the velocity profile. $\bar{U}(\boldsymbol{f})\pm\boldsymbol{s}$.
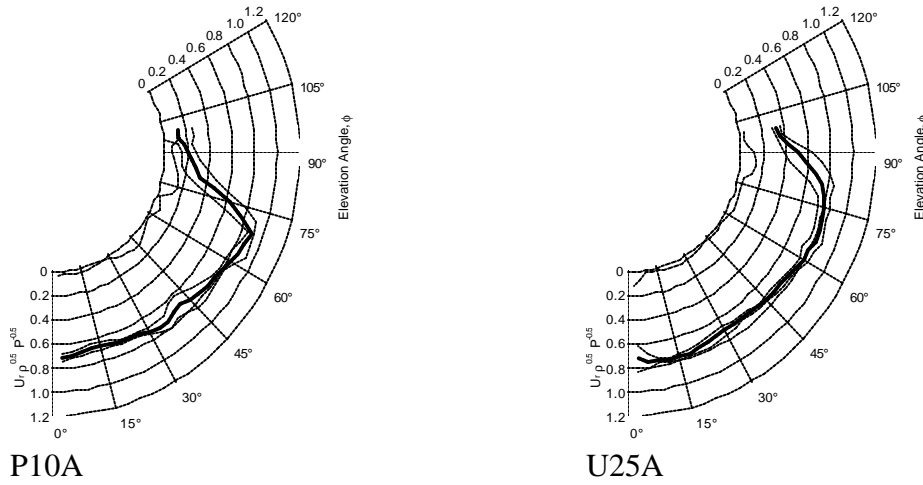
Figure 42. Dimensionless radial velocity for P10A and U25A sprinklers averaged over 3 pressures.

It is interesting to note that the largest errors for both the upright and pendant sprinklers occur for elevation angles $\phi>70°$. This larger error occurs near the edge of the spray where the velocity measurement is not as accurate as in other regions of the spray. The nondimensional velocity for the U25A sprinkler for different pressures collapses better (smaller σ) for $\phi<70°$ at all azimuthal angles as compared to the P10A. It is unclear whether this represents real differences in the sprinkler spray or if it is an artifact of the finer grid used in the PIV calculations for the different sprinklers. There is also substantial variation in the nondimensional velocity for the upright sprinkler directly below the sprinkler, $\phi = 0°$, likely due to the water supply pipe directly below the sprinkler.

The results of this analysis indicate that the non-dimensionalized velocity, $u_r\sqrt{r/P}$ properly accounts for the effect of orifice pressure even at specific sprinkler locations. While it could intuitively be assumed that the average velocity in the flow

field would be proportional to the velocity through the orifice and thus also to $\sqrt{P}$, it is not obvious that this same relationship should hold at specific locations in the flow field. Visual observation of the spray shows that as the pressure changes, the location of the dense portions of the spray change. There are also several physical factors between the orifice and the spray that could effect the relationship, such as the increased water jet momentum striking the deflector, which could tend to reduce the likelihood of the dimensionless spray velocity remaining constant a specific locations. Nevertheless, the non-dimensionalization to account for the effect of the pressure appears to be robust.

5.7   Non-Dimensional Velocities

The nondimensionalization scheme of the previous section appears successful so the velocity results from Figure 33 and Figure 34 were reformatted using the non-dimensionalization as shown in Figure 43 and Figure 44. This has the advantage of allowing comparisons of the radial velocity profile between various sprinklers. While the shapes of the velocity profiles are identical to those in Figure 33 and Figure 34, it is clear that the nondimensional radial velocity is generally between 0.6 and 1.0. This aspect, along with several others related to the nondimensional velocity profiles are discussed in the next sections.
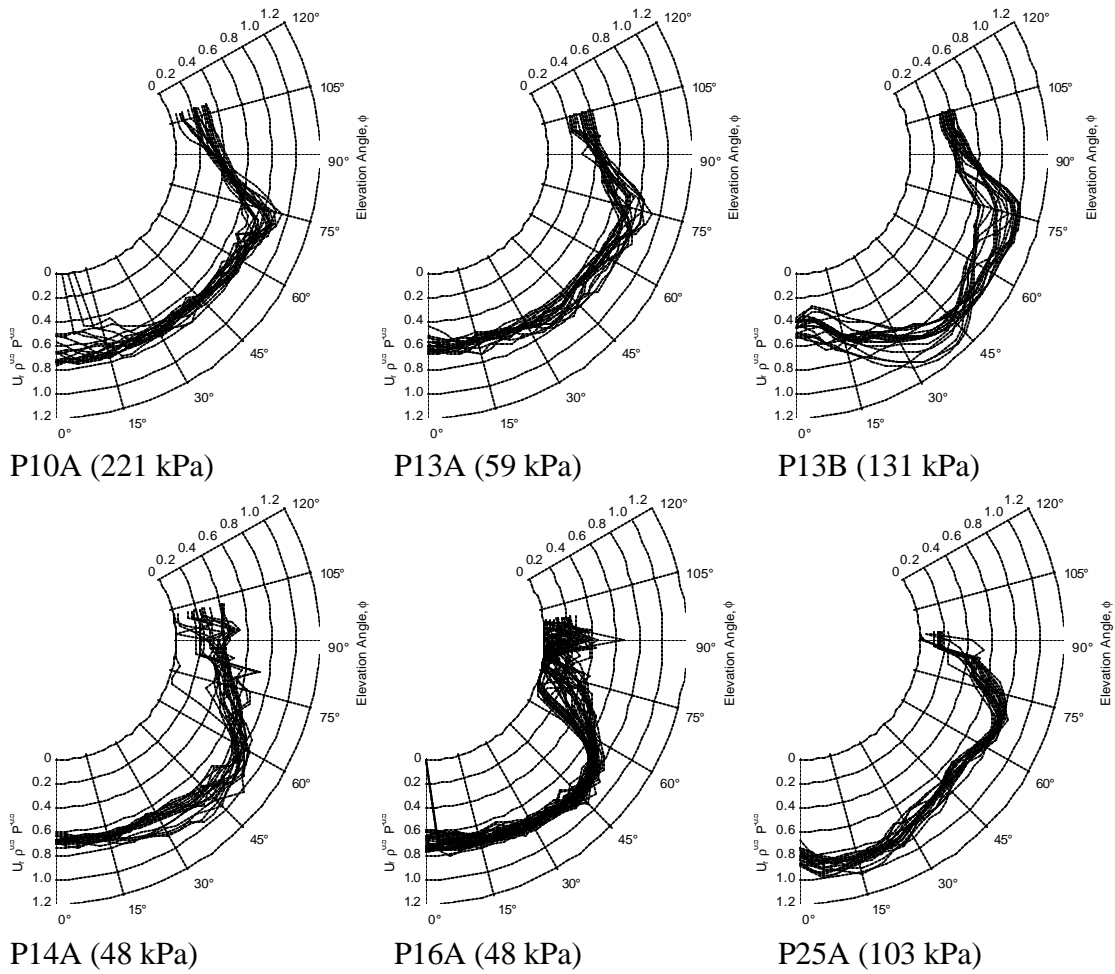
Figure 43. Nondimensionalized Velocities for Pendant Sprinklers
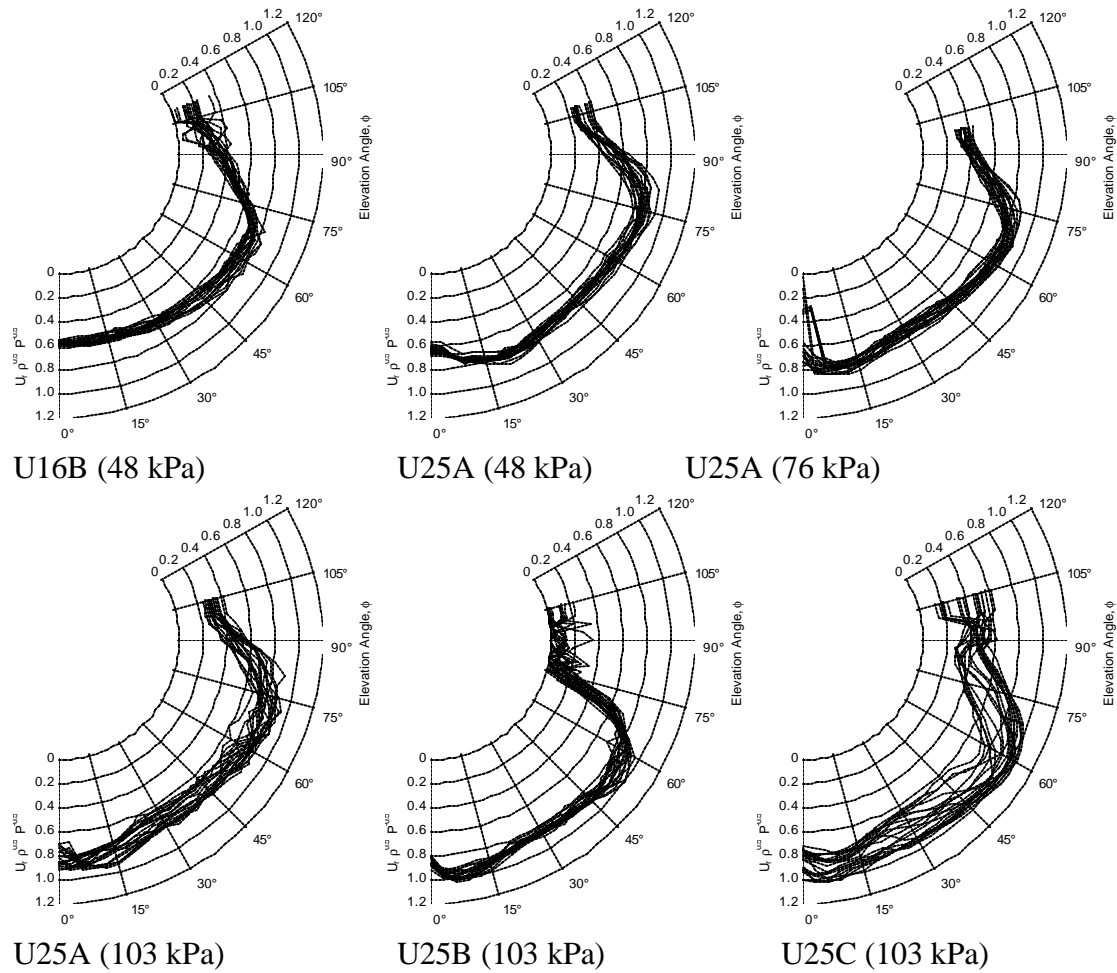
Figure 44. Nondimensionalized Velocities for Upright Sprinklers

U16B (48 kPa)   U25A (48 kPa)   U25A (76 kPa)

U25A (103 kPa)   U25B (103 kPa)   U25C (103 kPa)

5.8   Average Velocity Profiles

It would greatly simplify sprinkler spray analysis if an average velocity could be used globally to describe the spray, or if that were not possible, to at least provide a typical velocity dependant on only a single coordinate. Figure 45 presents the weighted average velocities over all θ and ϕ from Figure 38 after nondimensionalization has been applied. The nondimensional velocities are presented with error bars representing the

standard error $\pm\sigma$ over all θ and ϕ. The standard deviations for individual tests range from $\pm25\%$ to $\pm60\%$ of the weighted mean velocities. An overall weighted velocity from all tests was calculated and is shown as the last column in Figure 45. The global average nondimensional velocity is 0.59 with a standard deviation of 0.24.
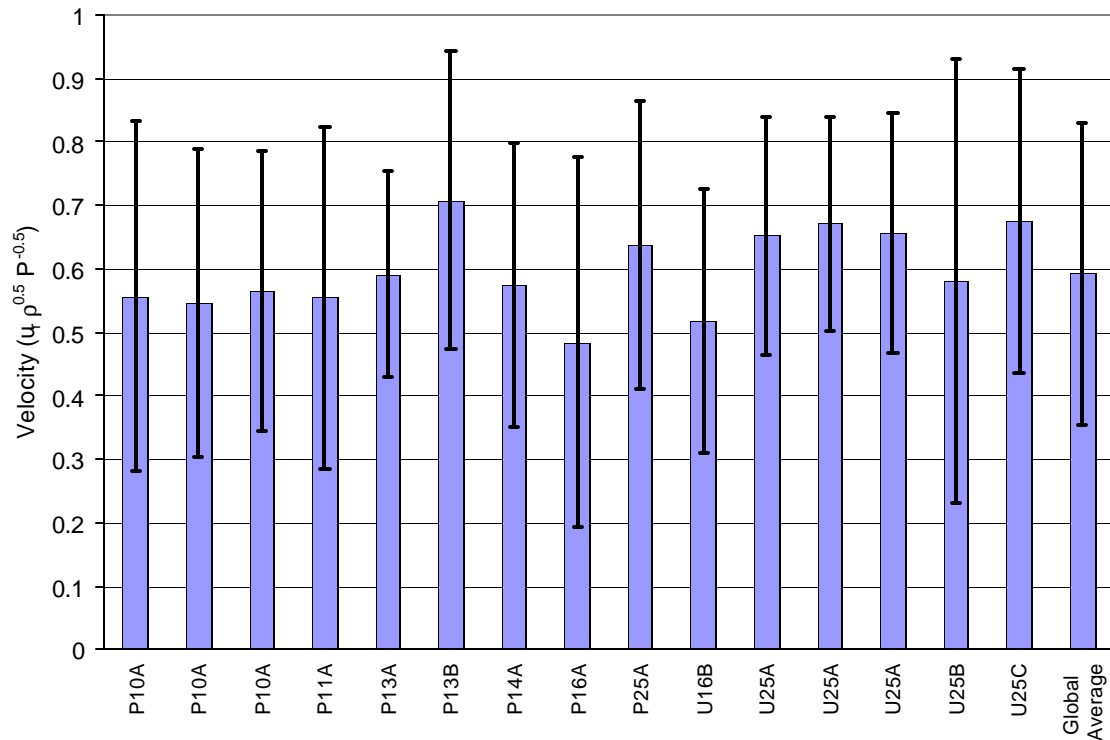
Figure 45. Average Nondimensionalized Velocities

The global average does not provide an acceptable model for defining all sprinkler sprays because of the large variation from position to position. Nevertheless, the relationship in equation (5.4) does provide a ball-park estimate of the radial velocity close to the sprinkler that has not previously been available.

$$u_{avg} \approx 0.6 \sqrt{\frac{P}{r}} \qquad (5.4)$$

The ensemble-averaged radial velocity and standard deviations are plotted as a function of elevation angle the result in Figure 46. The curves in Figure 46 include the standard deviation, σ, average velocity, $\bar{U}_{avg}$, and standard error, $\bar{U}_{avg} \pm \sigma$. Figure 46 presents the data from six tests, three with pendant sprinklers and three with upright sprinklers. The dimensionless velocities for the other sprinklers are shown in Figure 42. The graphs show that the standard deviations for most of the sprinklers were very small, but for two of the sprinklers (P13B and U25C) the standard deviation was somewhat larger.

P13A (59 kPa)   P13B (131 kPa)   P16A (48 kPa)

U16B (48 kPa)   U25A (48 kPa)   U25C (103 kPa)
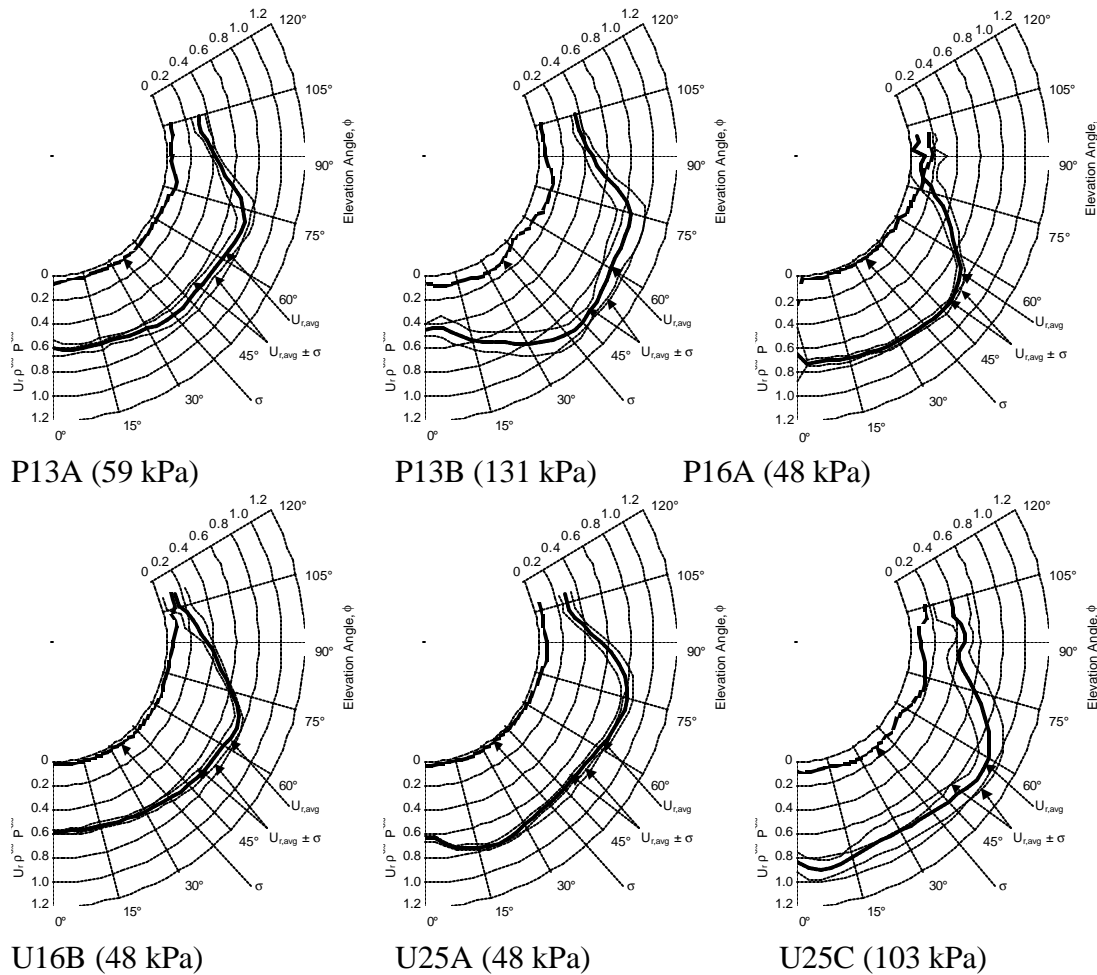
**Figure 46. Nondimensionalized radial velocity averaged over azimuthal angle
plotted as a function of elevation angle**

In fact if the azimuthally averaged standard deviation of the radial velocity is
plotted for each of the tested sprinklers as shown in Figure 47, five of the twelve
sprinklers can reasonable be modeled as axisymmetric because the standard deviations
are less than 5%. Unfortunately, this assumption may not be appropriate for all
conditions with each sprinkler. For example, for the highest pressure test of the U25A
sprinkler the average standard deviation jumped from less than 5% to 8%.
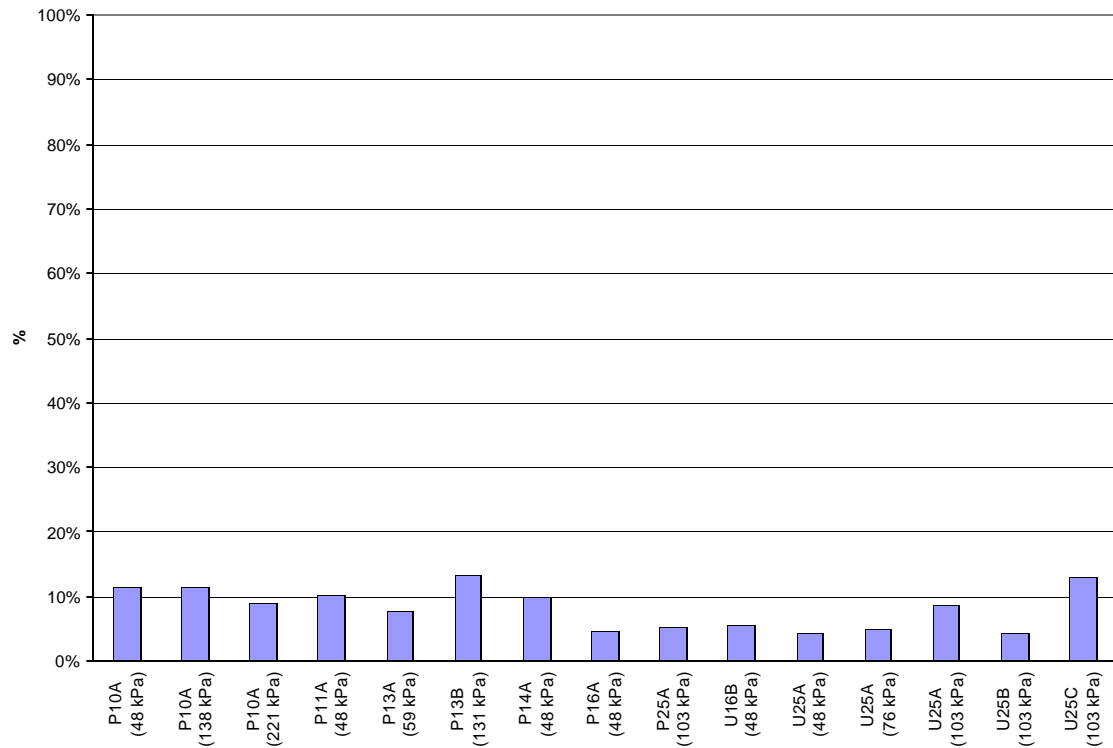
Figure 47. % standard deviation for azimuthally averaged radial velocities

To determine the dependence of the radial velocity on azimuthal angle, θ, the nondimensionalized velocity data was plotted as a function of azimuthal angle for all elevation angles, ϕ. The velocity results are presented in a polar chart format as shown in Figure 48 for the P13B and U25A sprinklers. The small circle in the center of the chart represents the location of the vertical axis. The polar chart extends from parallel to the frame arms, $\theta = 0°$, to perpendicular to the frame arms, $\theta = 90°$. The scale for the magnitude of the nondimensional radial velocity ranges from 0 to 1.2.

This type of azimuthal plot highlights different features of the flow field than were observable in the velocity profiles as a function of elevation angle. The spread of

the data as a function of elevation angle is readily apparent. The velocities for the P13B sprinkler are fairly evenly distributed as a function of elevation angle over the range of 0.4 to 1.0, whereas most of the velocities for the U25A are in a tight grouping between 0.7 and 0.9. Some of the P13B velocity profiles have a slight rise in radial velocity near the sprinkler frame arms in the $\theta=0°$ to $\theta=10°$ region. The U25A shows a saw-tooth pattern with maximums at $\theta=40°$, $60°$ and $75°$ for some of the velocity profiles.

P13B   U25A
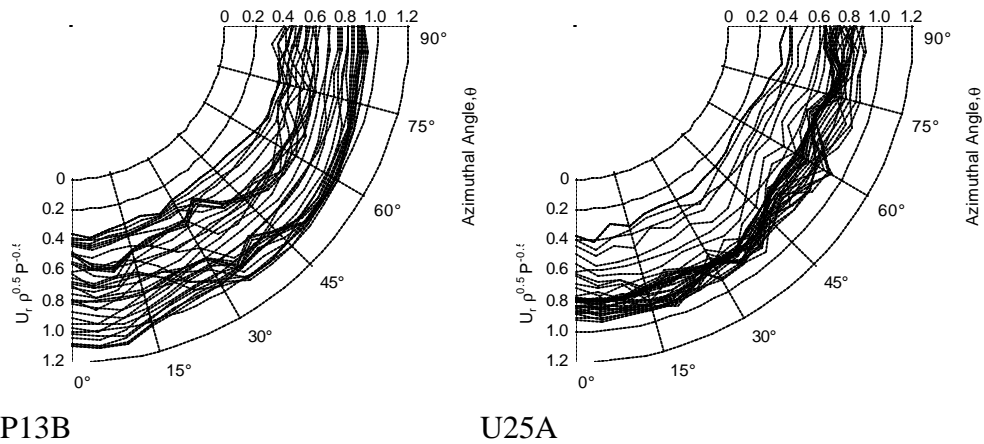
Figure 48. Nondimensionalized velocity plotted as a function of azimuthal angle for all elevation angles

When the weighted averages and standard deviations are calculated as a function of elevation angle and plotted as a function of azimuthal angle the result is shown in Figure 49. The dashed curve closest to the axis represents the standard deviation, σ. The darkest curve represents the weighted average velocity, $\bar{U}_{avg}$, and the two surrounding curves represent the standard error, $\bar{U}_{avg} \pm \sigma$. The standard deviation was typically at least 30% of the weighted average velocity. This result is not unexpected because of the

large variation in the radial velocity with elevation angle observed earlier in Figure 43 and Figure 44.

P13B   U25A
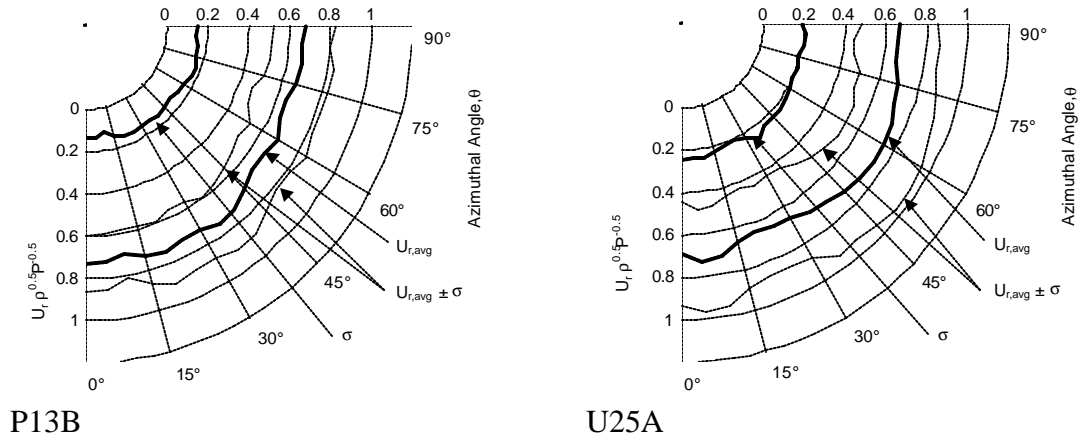
Figure 49. Nondimensional radial velocity averaged over elevation angle plotted as a function of azimuthal angle for the P13B and U25A sprinklers

The nondimensional radial velocities from all the sprinklers were combined to produce a typical axisymmetric sprinkler velocity profile. The calculation was done as an ensemble average over the azimuthal angles of the non-dimensional velocities at each elevation angle. This ensemble average included 19 radial velocities for each of thirteen sprinklers at each elevation angle. Figure 50 shows the average axisymmetric velocities, $\bar{U}_{avg}$, the standard deviation, σ, and the variance, $\bar{U}_{avg} \pm \sigma$. The average velocity remains between 0.6 and 0.8 for elevation angles below $\phi < 75°$. It then decreases to a minimum of 0.2 at an elevation angle of $\phi = 111°$. The average standard deviation was 26% of the radial velocity.
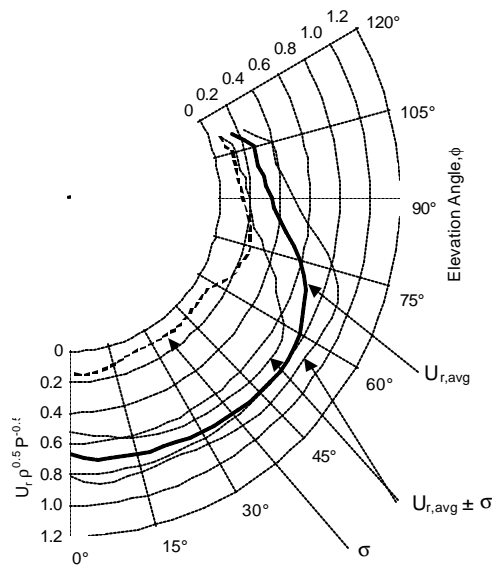
Figure 50. Combined axisymmetric velocity for all sprinklers as a function of elevation angle plotted with the standard deviation.

To provide an indication of the limits of the measured radial velocities, the maximum and minimum radial velocity at each elevation angle for any sprinkler at any azimuthal angle was found. Figure 51 shows the maximum and minimum nondimensional radial velocities as a function of elevation angle. The maximum velocities are relatively constant near a value of 1.0 in the region $0° \leq \phi \leq 80°$. At higher elevation angles, $\phi > 80°$, the maximum velocity decreases to approximately 0.4 at $\phi = 111°$. The minimum radial velocity shown in Figure 51 is zero directly below the sprinkler, $\phi = 0°$, which occurred for upright sprinklers with water supply pipe below the sprinkler. The minimum radial velocity remains fairly uniform near 0.6 for the region $20° \leq \phi \leq 57°$, and drops to zero above $\phi = 60°$ reflecting that some sprinklers spray very little water horizontally.
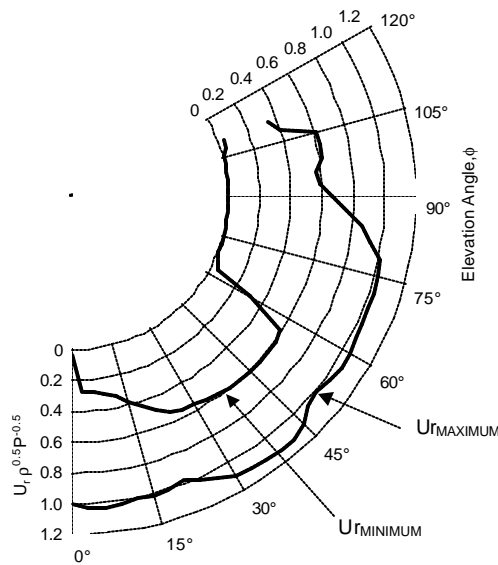
Figure 51. Maximum and minimum nondimensional radial velocity measured for all sprinklers at any azimuthal angle.

Figure 51 provides valuable insight about the limits of the sprinkler spray velocity. The maximum dimensionless spray velocity is typically near 1.0. The minimum spray velocity is approximately 0.6 except where obstructions such as water pipes exist or near horizontal.

5.9   Structure In The Velocity Profile

In Figure 48 peaks were observed in the velocity profile of the U25A sprinkler as a function of azimuthal location. It seems logical that these peaks could be high velocity regions caused by streams of water flowing through the notches in the deflectors. In order to evaluate if this is in fact the case, the nondimensional velocities for two of the sprinklers with large notches were plotted as contour plots in Figure 52 and Figure 53. These figures show the nondimensional velocities for a quadrant of the spray. The

coordinates of the velocities have been mapped to a projection that is similar to a Molweide projection, also known as an equal area projection. This format is typically used by cartographers. Its main advantage is that areas are the nearly the correct size in relation to each other. The disadvantage of this format is that the shapes of the areas are distorted and sometimes appear elongated, especially at the poles. In Figure 52 and Figure 53, the top edge of the figure corresponds to an elevation angle of $\phi = 90°$ corresponding to the equator of a sphere with the sprinkler at its center. Across this top edge, the azimuthal angle varies from $\theta = 0°$ at the left to $\theta = 90°$ at the right. The curves starting at the marked angles at the top of the figure converge at a single point at the bottom of the figure corresponding to the south pole of the sphere surrounding the sprinkler. At any elevation angle, the distance between the $\theta = 0°$ and the $\theta = 90°$ curve corresponds to the arc length around the sphere at this elevation angle.

The U25A plot in Figure 52 has three high velocity regions at an elevation angle of $50° \leq \phi \leq 70°$ and azimuthal angles of $0° \leq \theta \leq 25°$, $35° \leq \theta \leq 40°$, and $50° \leq \theta \leq 60°$. These regions correspond approximately to the location of the deflector notches. The width of the high velocity region near $\theta = 0°$ is much wider than the other regions, probably due to the influence of the frame arms. There is a clearly defined region of lower speed flow that exists in the $65° \leq \theta \leq 70°$ azimuthal angle region for a large range of elevation angles ($20° \leq \phi \leq 80°$). This region roughly corresponds to the location of a ridge on the sprinkler deflector.
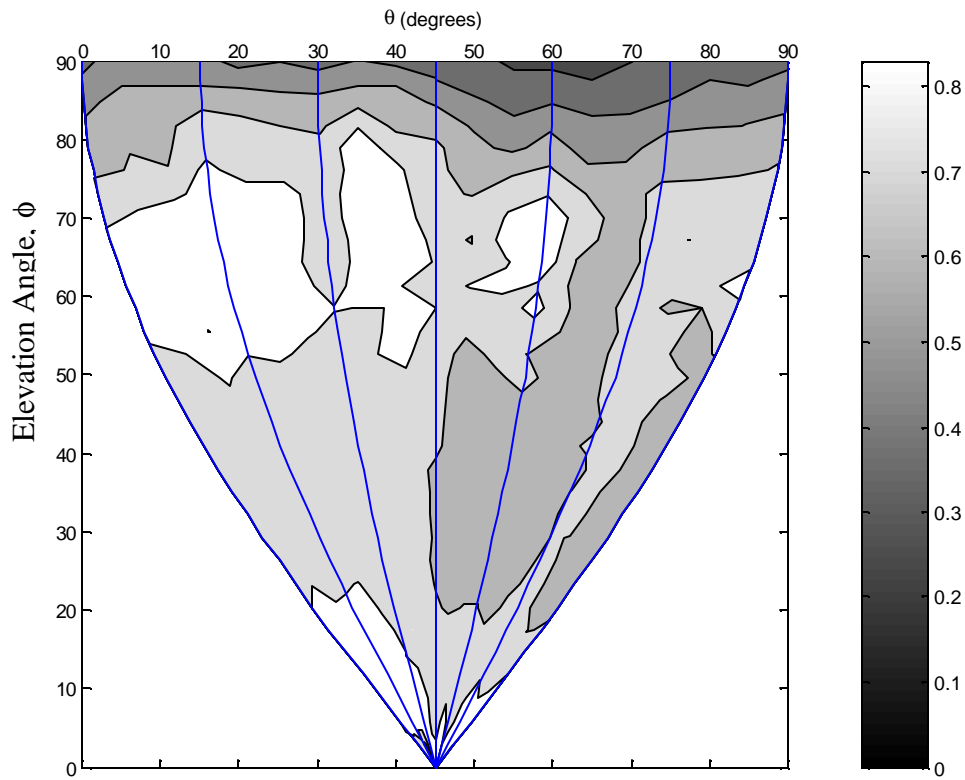
Figure 52. Contour plot of U25A nondimensional radial velocities

The U25B sprinkler in Figure 53 exhibits high velocity regions at an elevation angle of $45° \leq \phi \leq 60°$ and $\theta=20°$, 50° and 70°. The number of high velocity regions is equal to the number of notches in the deflector and the high velocity regions are at approximately the same azimuthal location as the notches.
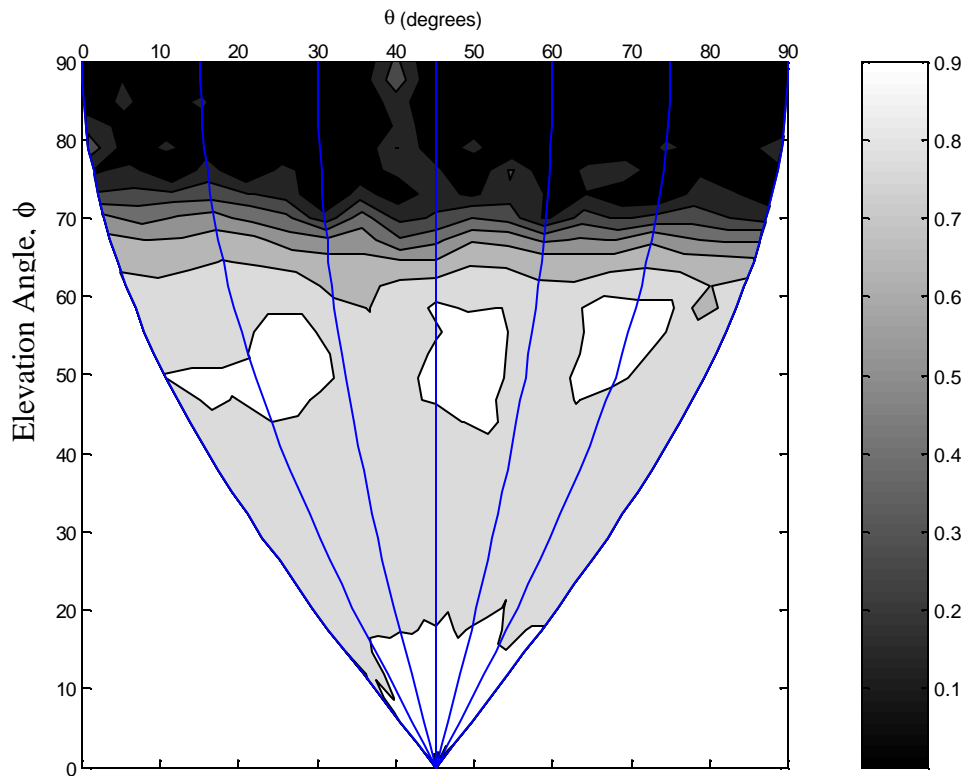
Figure 53. Contour plot of U25B nondimensional radial velocities

High velocity regions in locations corresponding to the deflector notches are probably present for all sprinklers with deflector notches, but they were only observed in the 25mm diameter orifice upright sprinklers. The most likely explanation for not observing the high velocity regions in other sprinklers is that the other sprinklers had much smaller notches or metal between the notches. This resulted in much narrower high velocity regions, or narrower low velocity regions between the high velocity regions, that were not be resolved within the $\theta = 5°$ azimuthal angle between the laser sheet measurements, on the other hand, the average width of the notch and metal between notches for the 25mm orifice upright sprinklers is about $10°$, so there would typically be two laser-sheet measurements within each high velocity region.

5.10 Conclusion

The following conclusions can be made from the results discussed in this chapter.

> ➤ The spray velocity near sprinklers is dependent on the azimuthal angle and the elevation angle. The spray velocity near the sprinkler is radial. The shape of the velocity profile varied widely from sprinkler to sprinkler with no differentiation between upright and pendant sprinklers.

> ➤ The origin of the spray velocity is along the axis of the sprinkler between the orifice and the deflector for pendant sprinklers and between the orifice and 0.05m above the deflector for upright sprinklers.

> ➤ The maximum radial velocities ranged from 5.8 to 14.1 m·s^{-1}. The ratio of the maximum velocity to average orifice velocity was near 100% for many pendant sprinklers. The ratio was always less than 100% for upright sprinklers.

> ➤ The non-dimensionalized velocity, $\bar{U} = u_r\sqrt{r/P}$ properly accounts for the effect of orifice pressure on the radial droplet velocity measured 0.2m from the sprinkler.

> ➤ The relationship, $\bar{U}_{avg} \approx 0.6\sqrt{P/r}$, although not perfect, provides a ball-park estimate of the radial velocity close to the sprinkler that has not previously been available.

> ➤ The velocity profiles for 5 of 12 sprinklers could be reasonably modeled as axisymmetric because the standard deviation at any elevation angle was less than

5%. Further study revealed that variations in the velocity profile could be linked

to sprinkler features such as deflector notches.

➢ A typical axisymmetric sprinkler velocity profile was created from all the velocity

results. The average nondimensional velocity remains between 0.6 and 0.8 for

elevation angles below $\phi < 75°$. It then decreases to a minimum of 0.2 at an

elevation angle of $\phi = 111°$. The average standard deviation was 26% of the

radial velocity.

6   Sprinkler Spray Droplet Sizes

Phase Doppler interferometry (PDI) measurements were made at fixed radial distances close to the sprinkler and along a horizontal plane 1m below the sprinkler as shown in Figure 54. The goal of the measurements close to the sprinkler was to determine the initial droplet size distribution and how it varies with elevation angle and sprinkler pressure. The goal of the measurements 1m below the sprinkler was to determine if the droplet size characteristics changed from that near the sprinkler and to provide a link with past research that was conducted at this distance below the sprinkler. Although it is highly likely that the droplet size distribution changes significantly with azimuthal angle, all experiments close to the sprinkler were conducted at a single azimuthal angle almost perpendicular to the frame arms, $\theta = 82°$, because of time constraints with the equipment.
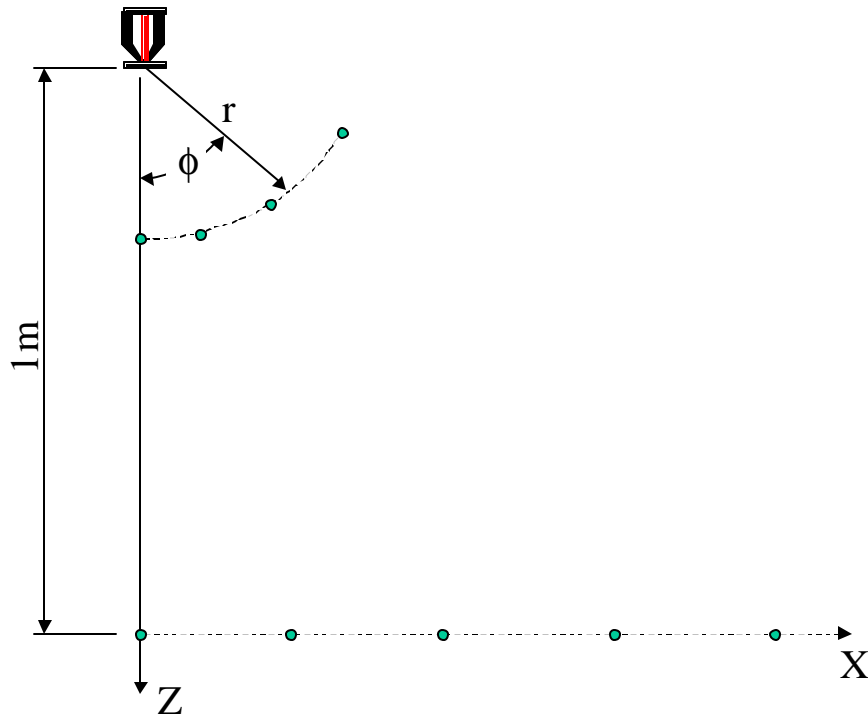
Figure 54. PDI Measurement Locations

6.1 Measurements Close to the Sprinkler

The measurements were conducted as close to the sprinkler as the instrumentation would allow. The locations were determined experimentally by moving the probe volume at increasing radial distances from the sprinkler regions until acceptable droplet diameter data, as defined by the PDI software, was obtained. A radial distance of 0.38m from the sprinkler was found to provide acceptable data for all sprinklers except the 25mm orifice sprinkler. For the 25mm orifice sprinkler a radial distance of 0.61m was required to produce acceptable data.

A total of 54 tests were conducted near the sprinklers with four pendant style and two upright style sprinklers. The droplet sizes at a minimum of three elevation angle

were evaluated for all sprinklers. All sprinklers, except the P19B, were tested at three

pressures. Table 7 provides a list of the test configurations along with the diameter

parameters calculated for each data-set.

Table 7. Equivalent Diameters measured near the sprinklers

Sprinkler	Pressure (kPa)	Elevation (degrees)	d_1 (μm)	DV50 (μm)	d_{32} (μm)
P10B	130	0	187	252	318
P10B	130	10	198	286	389
P10B	130	30	190	337	565
P10B	130	60	162	439	1250
P10B	196	0	189	255	316
P10B	196	10	202	279	358
P10B	196	30	175	262	365
P10B	196	60	162	350	899
P10B	306	0	192	256	319
P10B	306	10	210	279	338
P10B	306	30	181	254	341
P10B	306	60	177	322	635
P13B	37	0	205	791	1608
P13B	37	10	212	895	2017
P13B	37	30	406	1485	2856
P13B	37	60	721	3393	1915
P13B	57	0	196	733	1570
P13B	57	10	206	1142	5693
P13B	57	30	305	1159	2534
P13B	57	60	573	1450	2888
P13B	88	0	194	688	1561
P13B	88	10	187	613	1431
P13B	88	30	264	1003	2576
P13B	88	60	469	1251	2767
P13B	131	0	180	548	1307
P13B	131	10	177	518	1223
P13B	131	30	238	666	1268
P13B	131	60	398	1117	2814
P19A	345	0	291	696	1257
P19A	345	10	261	632	1195
P19A	345	30	157	344	766
P19A	345	60	215	454	1189

Sprinkler	Pressure (kPa)	Elevation (degrees)	d_1 (μm)	DV50 (μm)	d_{32} (μm)
P25A	138	0	323	910	2272
P25A	138	10	254	865	1852
P25A	138	30	257	961	1958
P25A	138	60	361	1197	2276
U16B	163	30	322	850	689
U16B	163	60	400	817	694
U16B	163	90	511	751	698
U16B	198	30	313	814	662
U16B	198	60	370	726	624
U16B	198	90	494	696	647
U16B	232	30	300	744	622
U16B	232	60	358	697	598
U16B	232	90	483	699	654
U25A	89	30	355	1057	853
U25A	89	60	475	1155	938
U25A	89	90	795	1167	1055
U25A	123	30	331	950	767
U25A	123	60	388	1056	822
U25A	123	90	727	1117	1018
U25A	158	30	280	829	659
U25A	158	60	337	975	750
U25A	158	90	652	1000	918

The average number of droplets counted in an individual experiment was 10286 with a maximum of 13028 and a minimum of 6094. The duration of the PDI experiments was defined by the criteria of either 15000 droplets counted or 15 minutes elapsed. Most experiments were terminated by the 15 minute criterion. The reason that the maximum number of droplets counted was 13028 instead of 15000 was that the PDI software always discarded some droplets due to its internal verification algorithms.

The equivalent diameters in Table 7 were evaluated to see if they were related to one another. DV50 and d_{32} were found to follow a general trend with d_1 as shown in Figure 55 and Figure 56. Generally, pendant and upright sprinklers appear to have

different correlations. However, the relation between d_1 and DV50 or d_{32} is fairly weak, based on the correlation coefficient for a linear fit, noted in the figures.
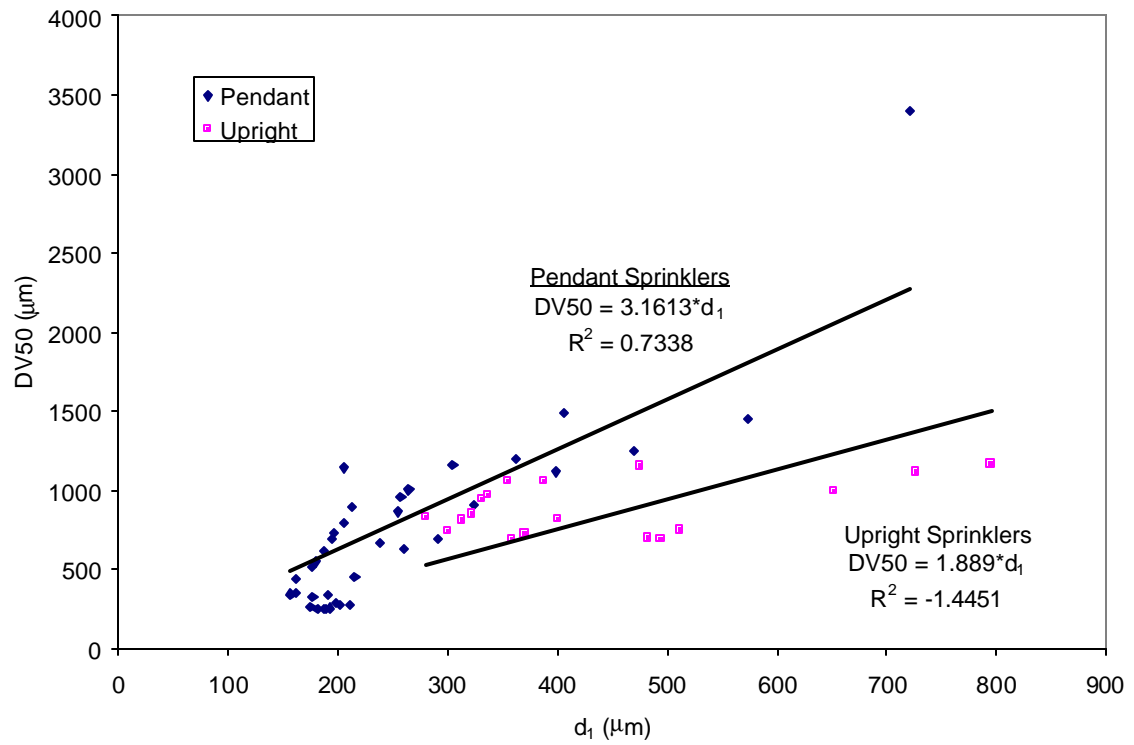
Figure 55. Relation between DV50 and d_1 for measurements close to the sprinkler
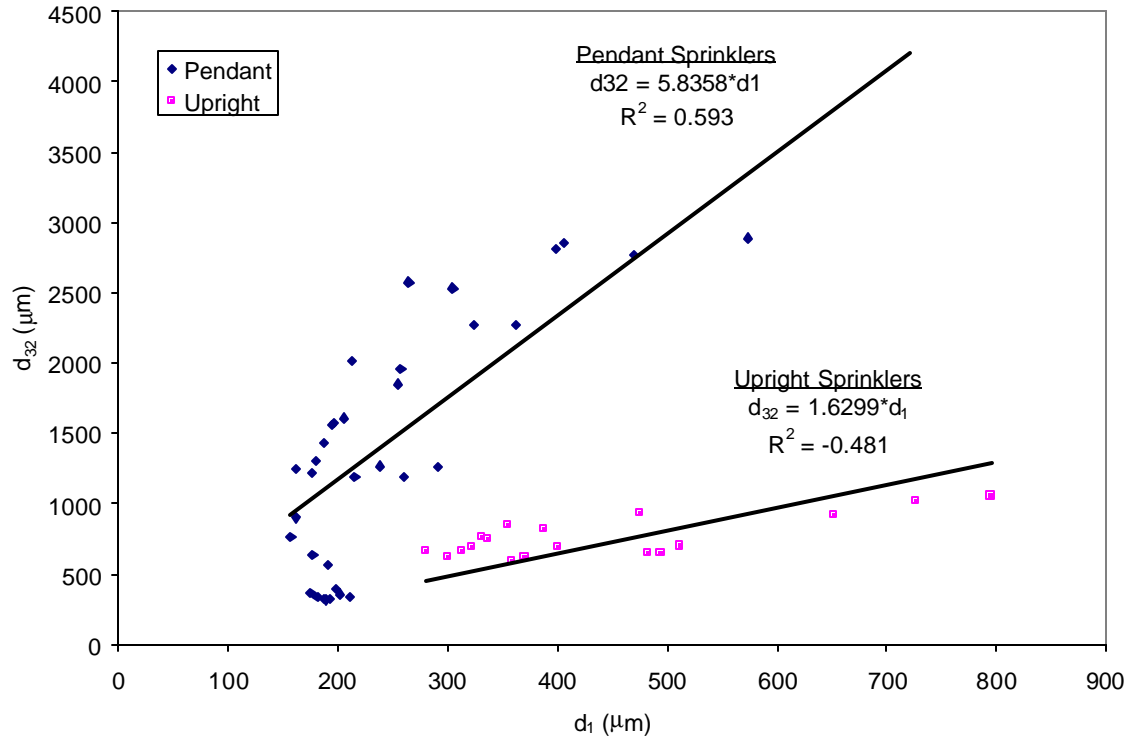
Figure 56. Relation between d_{32} and d_1 for measurements close to the sprinkler

A relationship was found between d_{32} and DV50 for each of the sprinkler type as shown in Figure 57. A linear interpolation found slopes of 2.13 and 0.84 with correlation coefficients of 0.94 and 0.87 for pendant and upright sprinkler, respectively. This relationship, while not anticipated, provides a useful method of converting one measure of droplet diameter to another. It is unclear why upright and pendant sprinklers have different slopes for these relationships. It can only be assumed that there is a difference in the way that the droplets are formed for the different sprinkler orientations.
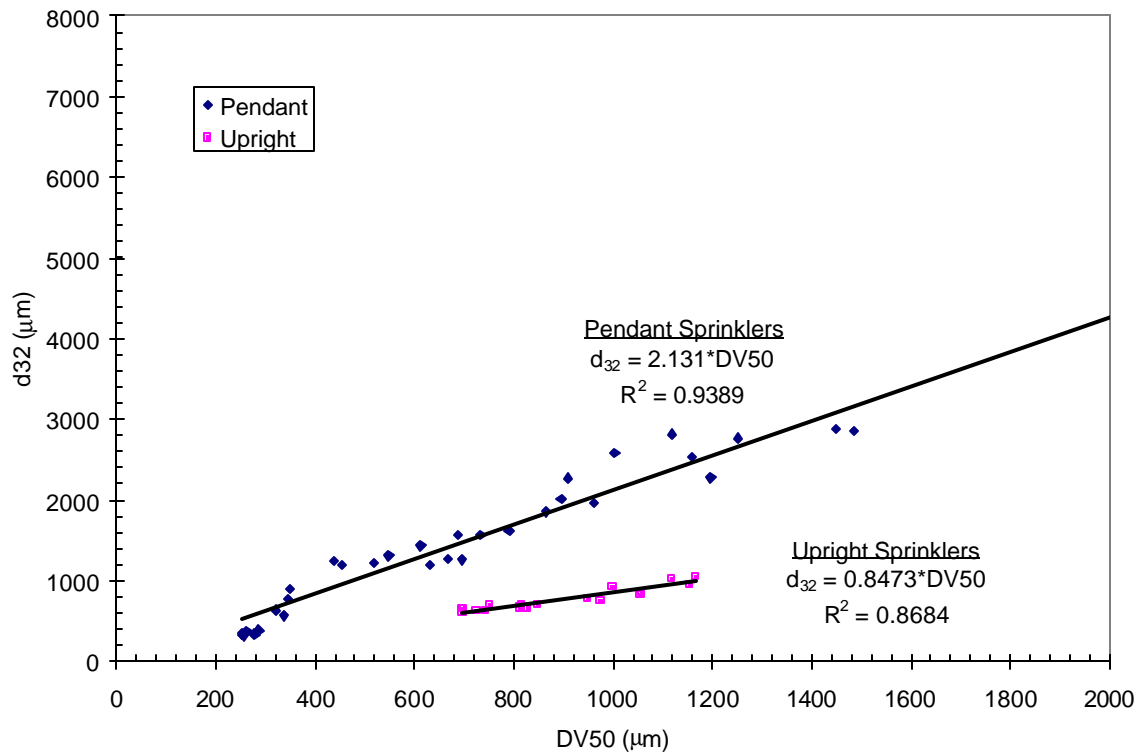
Figure 57. d_{32} as a function of DV50 for measurements close to the sprinkler

6.1.1 Droplet Size Distributions

The initial analysis of the droplet data consists of number count histograms, cumulative counts, and cumulative volume as a function of droplet size as shown in Figure 58 through Figure 61. Histograms were developed using 50μm bin sizes from 0 to 2000μm with a final bin for all droplets larger than 2000μm. The cumulative count (cumulative %) plot provides a clear method to see the fraction of total droplets in a range. The CVF (volume %) provides a method to determine the fraction of the total water that is being carried by droplets of a specific size range.

Figure 58 through Figure 61 shows the droplet size data for the P13B sprinkler at a pressure of 88kPa at elevation angles of ϕ=0°, 10°, 30° and 60°. The droplet diameters are on the horizontal axis, the cumulative percent is on the left vertical axis, and the frequency of droplets for each bin size is shown on the right vertical axis. The histograms in Figure 58 through Figure 61 reveal some interesting characteristics of the spray. At $\phi = 0°$, directly below the sprinkler, the maximum number of droplets were found in the 100µm and 150µm ranges respectively. The number of droplets quickly decreases as diameter increases until by 400µm the number of droplets has been reduced to almost 1/10 of the maximum value. By comparing the four plots and histograms it is clear that as the elevation angle in the spray increases the number of larger droplets increases. In the lower elevation angles, $\phi = 0°$ and $\phi = 10°$, the number of droplets larger than 1000µm drops to nearly zero. For the higher elevation angles, $\phi = 30°$ and $\phi = 60°$, 25% to 30% of the volume is contributed by droplets greater than 2000µm.

Of course the cumulative counts provide results similar to the histograms. The diameter for 50% cumulative count, D10, for the lower elevation angles was 194, 187, and 264µm, which is about the same size as that for the maximum droplet count in the histogram. The highest elevation angle, ϕ=60°, had a D10 of 469µm which is larger than the location for the largest droplet count, but this value is still not surprising considering the larger number of droplets with bigger diameters.

The cumulative volume fractions in Figure 58 through Figure 61 are interesting because they show that a relatively small number of large droplets carry the majority of

the water. As an example, the 150μm bin at the $\phi = 0°$ elevation angle has 3086 droplets

which are 56% of the total number of droplets, but these droplets only carry 2.4% of the

total water. In fact, at the lower elevation angles, $\phi = 0°$ and 10°, more than 50% of the

total water is carried by the droplets greater than 600μm in diameter. At the higher

elevation angles, $\phi = 30°$ and 60°, a large fraction of the water (>20%) is carried by one

or two very large droplets, as evidenced by the discontinuity in the CVF at the high end.
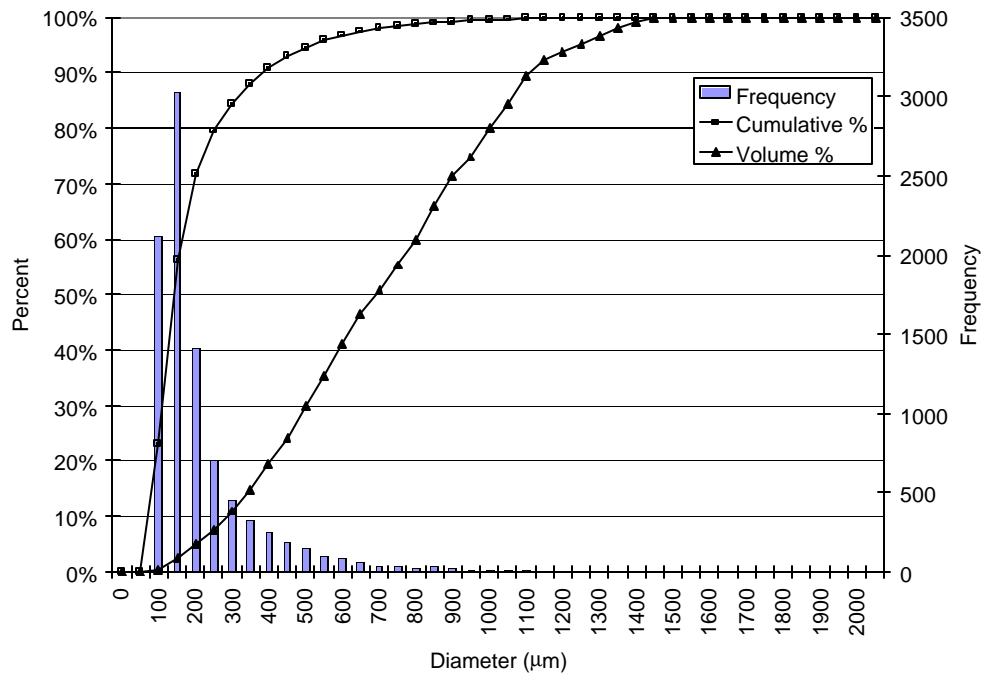
Figure 58. Histograms and CVFs for P13B at 88kPa, $\mathbf{f} = 0°$
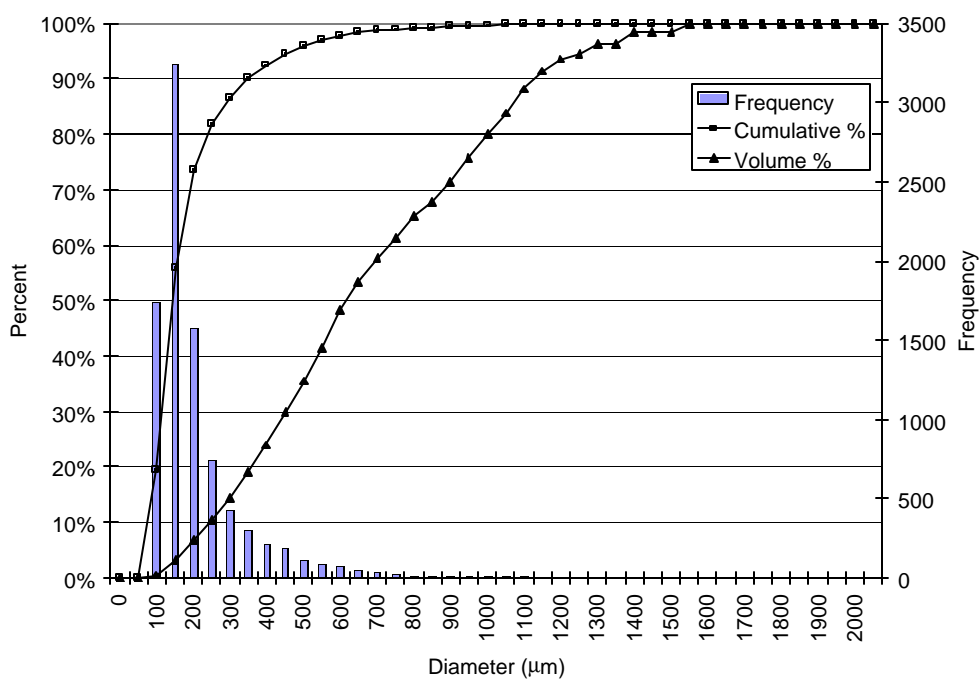
Figure 59. Histograms and CVFs for P13B at 88kPa, f = 10°
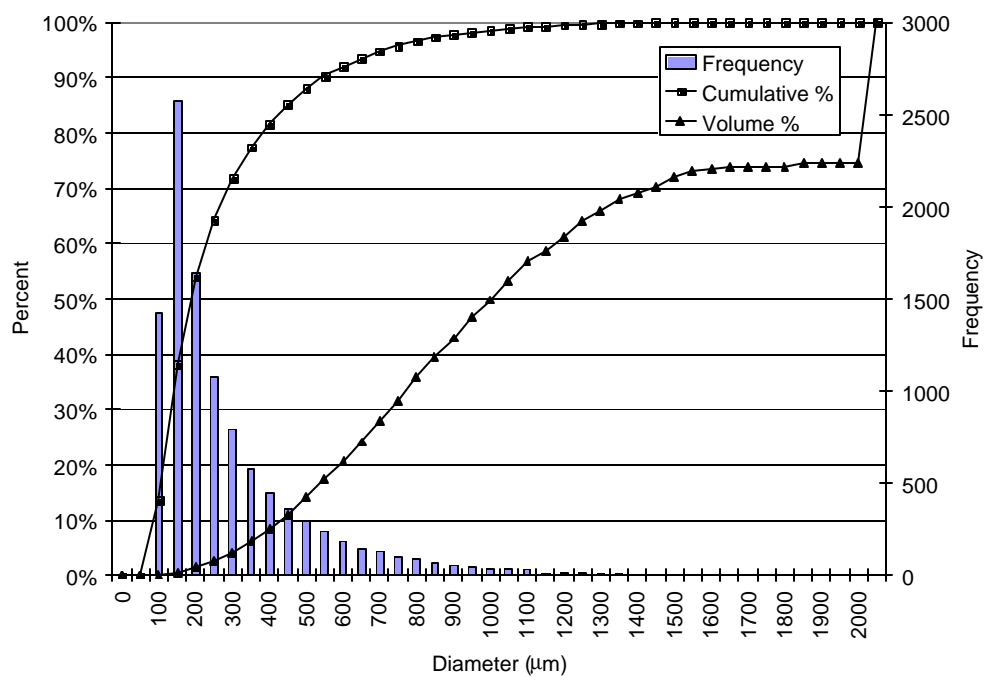
Figure 60. Histograms and CVFs for P13B at 88kPa, f = 30°
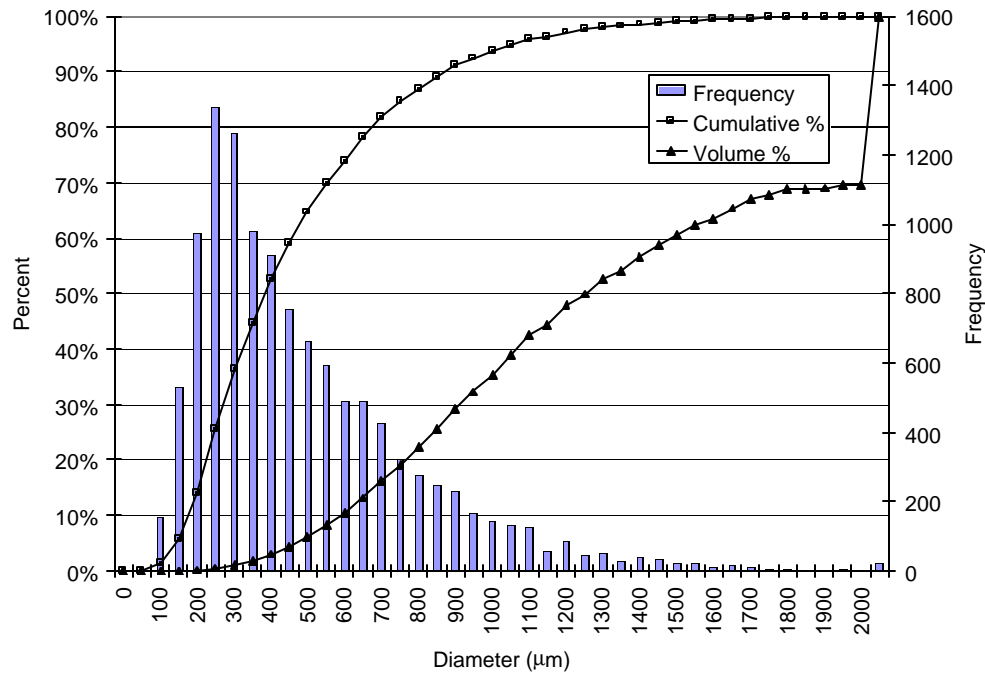
Figure 61. Histograms and CVFs for P13B at 88kPa, $f = 60°$

The behavior of having more large droplets present as the elevation angle increases was common to all sprinklers. For all sprinklers it was found that a few large droplets often dominated (20% to 40%) the water volume at a measurement point.

6.1.2 Droplet Distribution Function

Although there is no fundamental reason for the CVF functions to conform with one of the standard distributions functions, experimental CVF functions are often compared to the standard log-normal and Rosin-Rammler distribution functions in order to develop a qualitative assessment. To do this, the CVF were plotted in the log scale versus normal probability scale as shown in Figure 15. The CVF curves were individually evaluated to determine if they conformed to a standard distribution curve.

First, a least squares curve fit was performed to compare the entire experimental CVF to a log-normal distribution and to a Rosin-Rammler distribution and the data was plotted. If the experimental distribution was observed to conform to different distributions above and below the median volume diameter, DV50, a second least square analysis was conducted on each half of the CVF to calculate the best constants for the log-normal or Rosin-Rammler distribution.

Table 8 shows the test parameters in the first three columns, a description of the distribution to which the data is most similar in the next two columns and the calculated parameters for the distribution in the final four columns. The median volume diameter, DV50, was calculated by sorting the droplet diameters in ascending order, then calculating the droplet volume for each droplet, then calculating a cumulative volume using a numerical integration method. The DV50 was chosen as the droplet diameter in this sorted table where 50% of the cumulative volume was located. Interpolation was typically employed to find the DV50 value. The Rosin-Rammler constants, β and γ, were found using standard least squares analysis to find the best values. The log-normal standard deviation, $s_{\ln}$, was also found using standard least squares techniques although the procedure was more involved because the numerical integration of the log-normal CVF had to be recalculated at each step in the root finding process. When the distribution conformed with one of the standard distributions as shown in the fourth and fifth columns, the original best fit parameters for the other distribution was kept in the Table 8. For example, the P13B sprinkler at 30 kPa and an elevation angle of $\phi = 0°$

matches a Rosin-Rammler distribution above and below DV50 so the β and γ constants reflect the best-fit Rosin-Rammler curve. σ_{ln} in this case was calculated for the best fit log-normal curve for the entire data-set.

The distribution description columns in Table 8 show that the shape of the distribution curve is a function of the sprinkler, the location, and the pressure. For example, the CVF distribution changes with location for the P10B at 130 kPa. It has the same general shape at $\phi = 0°$, 10°, and 30°, but a different shape at $\phi = 60°$. The shape of the distribution also changes with pressure as evidenced by the change that occurs at $\phi=0$ and 60° when the pressure changes from 130 to 196 kPa.

For the majority of experiments (43 out of 54), the CVF distribution conformed to a log-normal distribution below DV50. For 9 experiments the entire CVF above and below the CVF conformed to a log-normal distribution. A log-normal distribution was never found above DV50 unless the distribution was also log-normal below DV50. For 39% of the experiments (21 out of 54) the CVF conformed to a Rosin-Rammler above DV50. In four cases for only the P13B sprinkler, the CVF conformed to a Rosin-Rammler above and below DV50. For fourteen experiments, the distribution was found to conform to the combination log-normal and Rosin-Rammler found by You [34] for ESFR sprinklers.

When evaluating the entire range of droplet sizes, the CVF did not conform exactly to a log-normal, Rosin-Rammler or combination log-normal/Rosin-Rammler distribution for more than half of the experiments. This result demonstrates that until a

fundamental understanding is developed of the droplet creation process from the deflector to the regions of fully developed droplet flow, the only method of determining droplet size distributions will be experiment testing at multiple locations and at a variety of pressures.

Table 8. Comparison of experimental CVF with log-normal and Rosin-Rammler distributions

Sprinkler	Pressure (kPa)	Elevation (degrees)	Distribution below DV50	Distribution above DV50	DV50 (µm)	β (µm)	γ (µm)	σ_{ln} (µm)
P10B	130	0	log-normal	above log-normal	252	0.63	3.20	0.36
P10B	130	10	log-normal	above log-normal	286	0.61	2.72	0.39
P10B	130	30	log-normal	above log-normal	337	0.62	2.06	0.48
P10B	130	60	below log-normal	below log-normal	439	0.68	1.73	0.68
P10B	196	0	log-normal	log-normal	255	0.63	3.31	0.36
P10B	196	10	log-normal	above log-normal	279	0.62	3.08	0.37
P10B	196	30	log-normal	above log-normal	262	0.63	2.57	0.41
P10B	196	60	log-normal	above log-normal	350	0.70	1.29	0.57
P10B	306	0	log-normal	above log-normal	256	0.61	3.04	0.35
P10B	306	10	log-normal	log-normal	279	0.62	3.49	0.35
P10B	306	30	log-normal	above log-normal	254	0.60	2.56	0.37
P10B	306	60	log-normal	above log-normal	322	0.61	1.65	0.48
P13B	37	0	Rosin-Rammler	Rosin-Rammler	791	0.67	2.24	0.73
P13B	37	10	log-normal	Rosin-Rammler	895	0.75	2.57	0.77
P13B	37	30	log-normal	Rosin-Rammler	1485	0.65	2.36	0.62
P13B	37	60	log-normal	log-normal	3393	2.15	2.28	0.79
P13B	57	0	Rosin-Rammler	Rosin-Rammler	733	0.69	2.30	0.74
P13B	57	10	log-normal	above log-normal	1142	0.62	1.19	0.86
P13B	57	30	log-normal	log-normal	1159	0.66	2.03	0.69
P13B	57	60	log-normal	log-normal	1450	0.63	2.18	0.61
P13B	88	0	Rosin-Rammler	Rosin-Rammler	688	0.70	2.30	0.73
P13B	88	10	log-normal	Rosin-Rammler	613	0.64	1.99	0.71
P13B	88	30	log-normal	above log-	1003	0.62	1.58	0.73

| Sprinkler	Pressure (kPa)	Elevation (degrees)	Distribution below DV50	Distribution above DV50	DV50 (μm)	β (μm)	γ (μm)	σ$_{ln}$ (μm)
				normal				
P13B	88	60	log-normal	log-normal	1251	0.62	1.87	0.62
P13B	131	0	log-normal	Rosin-Rammler	548	0.68	1.85	0.70
P13B	131	10	Rosin-Rammler	Rosin-Rammler	518	0.68	2.05	0.69
P13B	131	30	log-normal	Rosin-Rammler	666	0.68	2.30	0.65
P13B	131	60	log-normal	log-normal	1117	0.62	1.62	0.63
P19A	345	0	log-normal	Rosin-Rammler	696	0.65	2.13	0.59
P19A	345	10	log-normal	Rosin-Rammler	632	0.66	2.05	0.60
P19A	345	30	log-normal	log-normal	344	0.67	1.85	0.60
P19A	345	60	log-normal	above log-normal	454	0.63	1.51	0.51
P25A	138	0	log-normal	Rosin-Rammler	910	0.69	1.96	0.60
P25A	138	10	log-normal	Rosin-Rammler	865	0.69	2.19	0.69
P25A	138	30	log-normal	Rosin-Rammler	961	0.71	2.50	0.72
P25A	138	60	log-normal	Rosin-Rammler	1197	0.69	2.44	0.67
U16B	163	30	log-normal	Rosin-Rammler	850	0.70	2.22	0.60
U16B	163	60	log-normal	Rosin-Rammler	817	0.70	2.14	0.53
U16B	163	90	log-normal	above log-normal	751	0.71	2.06	0.37
U16B	198	30	log-normal	Rosin-Rammler	814	0.70	2.20	0.58
U16B	198	60	log-normal	below log-normal	726	0.70	2.12	0.51
U16B	198	90	log-normal	below log-normal	696	0.71	2.06	0.35
U16B	232	30	log-normal	log-normal	744	0.70	2.16	0.58
U16B	232	60	log-normal	below log-normal	697	0.71	2.10	0.50
U16B	232	90	log-normal	above log-normal	699	0.71	2.04	0.37
U25A	89	30	above log-normal	Rosin-Rammler	1057	0.72	2.03	0.64
U25A	89	60	above log-normal	below Rosin-Rammler	1155	0.72	2.07	0.59
U25A	89	90	log-normal	below Rosin-Rammler	1167	0.72	2.05	0.39
U25A	123	30	above log-normal	Rosin-Rammler	950	0.72	2.04	0.62
U25A	123	60	above log-normal	below Rosin-Rammler	1056	0.72	2.07	0.60
U25A	123	90	log-normal	below Rosin-	1117	0.72	2.06	0.41

Sprinkler	Pressure (kPa)	Elevation (degrees)	Distribution below DV50	Distribution above DV50	DV50 (μm)	β (μm)	γ (μm)	σ_{ln} (μm)
U25A	158	30	below log-normal	Rammler Rosin-Rammler	829	0.72	2.06	0.61
U25A	158	60	below log-normal	below Rosin-Rammler	975	0.72	2.06	0.61
U25A	158	90	log-normal	below Rosin-Rammler	1000	0.72	2.04	0.41

For experiments where the CVF conformed to a log-normal distribution, the log-normal standard deviation, $\boldsymbol{s}_{ln}$, ranged from 0.35 to 0.86 with an average of 0.55 and a standard deviation of 0.14. A graphical analysis was conducted to evaluate if σ was directly related to the pressure, the elevation angle, or the orifice diameter. The results indicate that no relationship exists between σ and these parameters.

For experiments where the CVF conformed to a Rosin-Rammler distribution, β ranged from 0.64 to 0.75 with an average of 0.69 and a standard deviation of 0.026 while γ ranged from 1.85 to 2.57 with an average of 2.19 and a standard deviation of 0.186. A graphical analysis was conducted to evaluate if β or γ are directly related to the pressure, the elevation angle, or the orifice diameter. Like the log-normal distribution, the results indicate that no relationship exists between β or γ and the other parameters. Analysis was conducted to determine if the Rosin-Rammler constants, β and γ, are related to one another as shown in Figure 62. Figure 62 shows a scatter plot between γ and β. No clear trend is visible, indicating no relationship between γ and β.
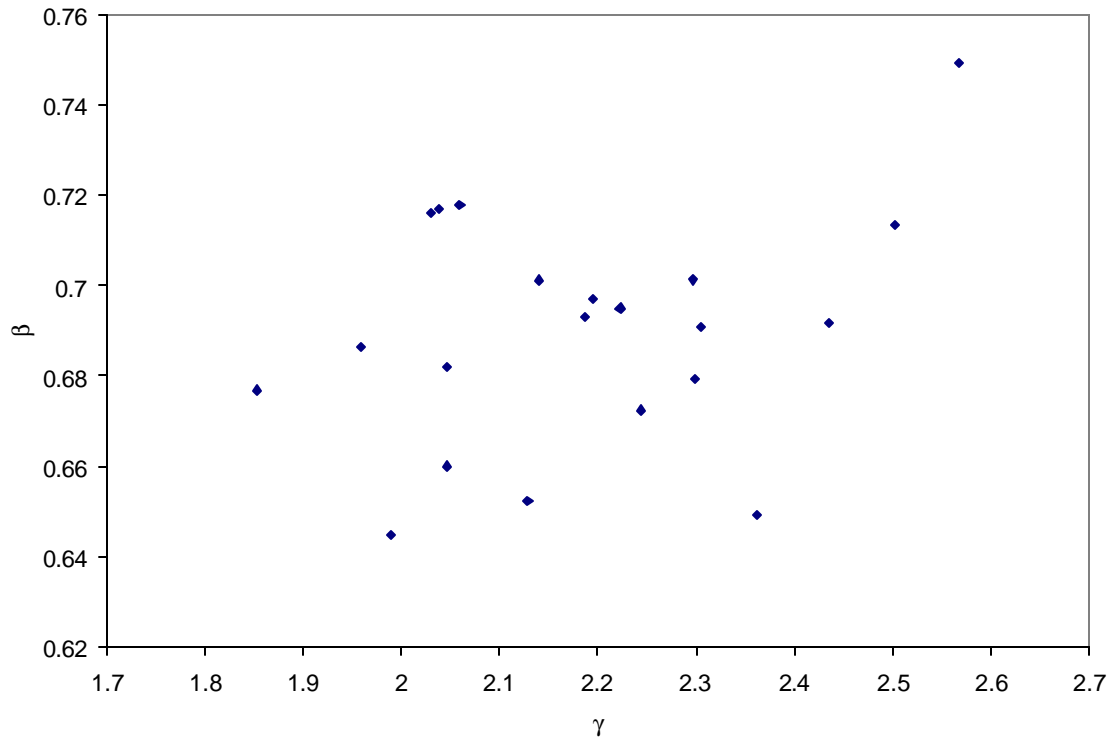
Figure 62. Relationship between Rosin-Rammler constants

6.1.3 Effect of Pressure on Median Diameter

Scaling analysis by Dundas [45] for water sprays has predicted that the median

droplet size should be proportional to the inverse cube root of the Weber number,

$We = \boldsymbol{r}_w u^2 d_1 / \boldsymbol{s}$, as follows

$$\frac{DV50}{D} = C\,\mathrm{We}^{-1/3} \tag{6.1}$$

where *DV50* is the volume median diameter, *D* is the orifice diameter, *C* is the constant

of proportionality, *u* is the velocity of the water jet, σ is the surface tension of water, and

$\boldsymbol{r}_w$ is water density. Experiments and a literature review by Lawson [46] showed that a

proportionality constant C = 2.7 provided the best fit to the available sprinkler data.

Figure 63 shows the droplet size normalized by the orifice diameter as a function of the Weber number. The correlation from Lawson's paper is the straight line. It should be noted that in Lawson's paper the data was well behaved with little variance from the correlation line.
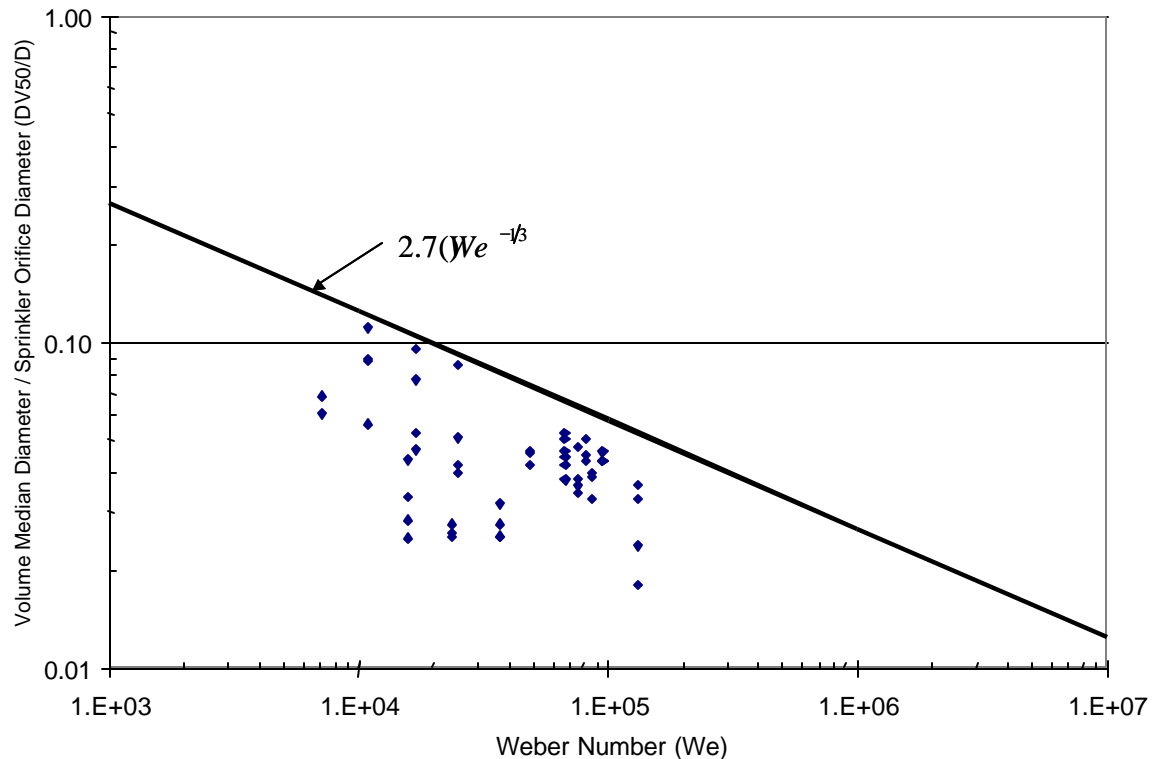
Figure 63. Comparison of Droplet Size Data to Dundas Correlation

Clearly, the current data-set does not match the correlation although it does appear that the correlation may provide an upper bound. There could be several reasons for this. The new data was: (1) obtained using newer and more sophisticated techniques which are able to measure a larger number of droplets at a higher diameter resolution, (2) taken closer to the sprinkler which provides measurements of the initial spray before droplet size dependence on the trajectory has an effect, (3) taken at different elevation

angles at fixed radial distances whereas Lawson's data was taken at various distances from the sprinkler.

Unlike previous research, the new data plotted in Figure 63 does not follow a clear trend. This is not unexpected when the large differences in median droplet diameter at different elevation angles is taken into account. The data was analyzed to see if elevation angle dependency of the droplet diameter could be identified as the culprit. In Figure 64 the volume median droplet diameter divided by the orifice diameter is plotted as a function of the Weber number. Fourteen data-sets are shown in Figure 64 each data-set represents one measurement location and one sprinkler at three water pressures. A best fit trend line is shown for each data series. The trend lines were calculated using least squares techniques assuming a linear approximation and assuming a y intercept of 0. The impact of this form of the trend line is that as the pressure (and consequently the velocity) increases towards infinity the median droplet diameter will approach 0. The trend lines in Figure 64 closely match the data for each elevation angle for a sprinkler. The slopes of the trend lines ranged from 0.72 to 2.48 with an average of 1.53.
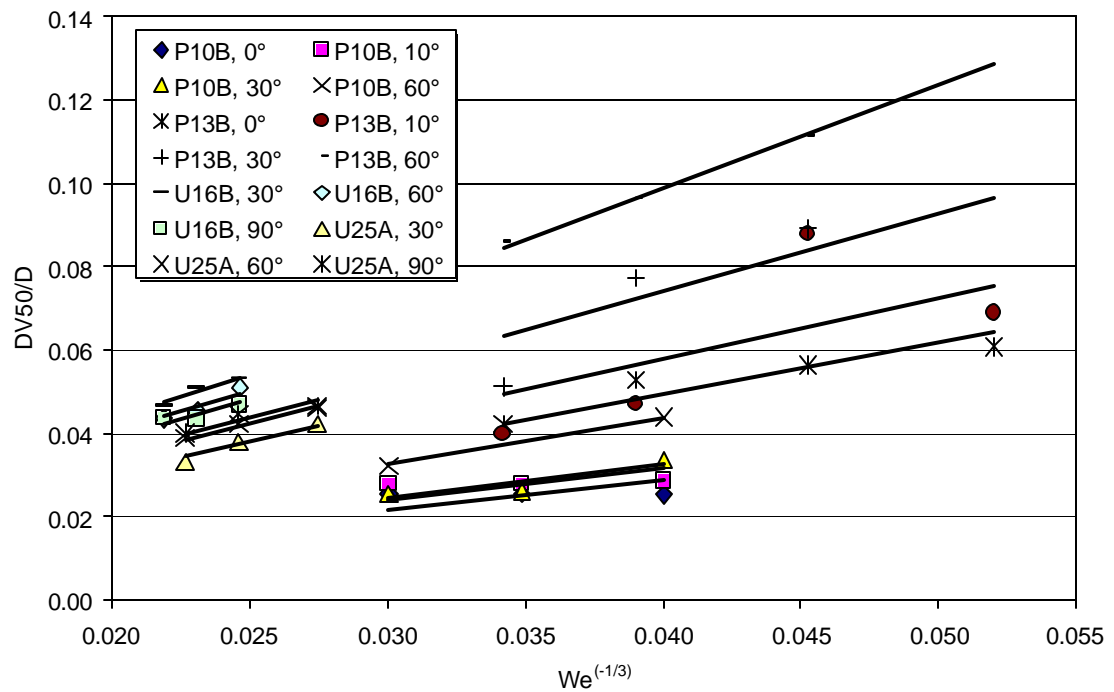
Figure 64. Droplet Diameter Relationship To Weber Number

The slopes of the trend lines from Figure 64 were plotted in Figure 65 ordered by sprinkler and then by elevation angle. It is clear that the slope of the trend lines is a function of elevation angle. For three of the four sprinklers, the slope increases with elevation angle, but for the U16B the slope decreases with increasing elevation angle.
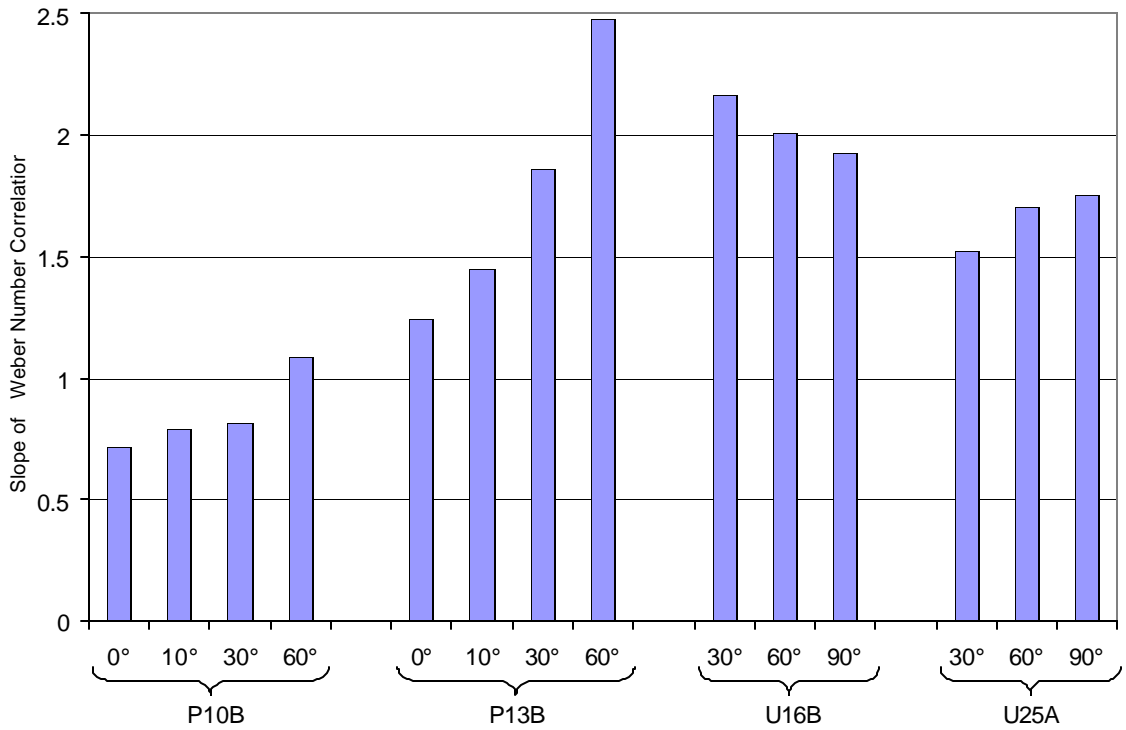
Figure 65. Slopes of Weber Number Trend Lines

The results of this analysis indicate that the volume median diameter is indeed proportional to the inverse cube root of the Weber number as postulated by Dundas [45] and indicated in equation (1.16). However, the 2.7 proportionality constant that was put forth by Lawson is not universal for all sprinklers or for all measurement locations and elevation angles near a specific sprinkler. The proportionality constant depends on both the sprinkler design and the location that the droplet size is measured in the spray.

6.1.4 Mass of Water Visible in Laser Sheet Experiments

The PDI results show that a large fraction of droplets are to small to be captured within the 300 μm/pixel resolution of the CCD camera used in the laser sheet experiments. In order for the laser sheet experiments to provide a meaningful measure of

the sprinkler spray, the droplets visible in the laser sheet images would have to comprise a large enough fraction of the water transported by the spray for the measurements to be considered representative.

Using the CVF analysis it is possible to determine the fraction of the total volume flow rate that is visible in the laser sheet experiments if an assumption is made about the minimum size of the droplets that are visible in the images. One could assume that any droplets that fill an entire pixel would definitely be detected in the CCD images of the laser sheet experiments. It is also plausible that a droplet that fills a substantial portion of an individual pixel would also be detected in the image. To evaluate what fraction of the water is visible in the laser sheet CCD images, the fraction of the total volume of water was calculated for droplets that were greater than or equal to 150, 200, or 300μm representing droplets that have diameters at least one-half, two-thirds or the entire dimension of one pixel in a laser sheet image.

Figure 66 shows the results of this analysis for six different sprinklers with different orifice sizes. The results show that the water volume detected in the CCD images approaches 100%. The sprinkler results are ordered by style (pendant or upright), and then by increasing orifice size. For the P13B, P25A and all of the upright sprinklers the total water fractions were above 90% regardless of elevation angle or the droplet sizes criterion. However, the P10B at 0° elevation angle only had 30% of the water carried by the droplets with diameters greater than 300μm, but that fraction increased to 76% and 94% when droplets as small as 200μm and 150μm were included, respectively. For the

P19A the total water fractions were lower than the P13B and the P25A, but not as small

as the P10A. Since the P19A data was obtained at a much higher pressure than for the

other sprinklers it is clear that the inverse relationship between the droplet size and the

pressure had an effect.
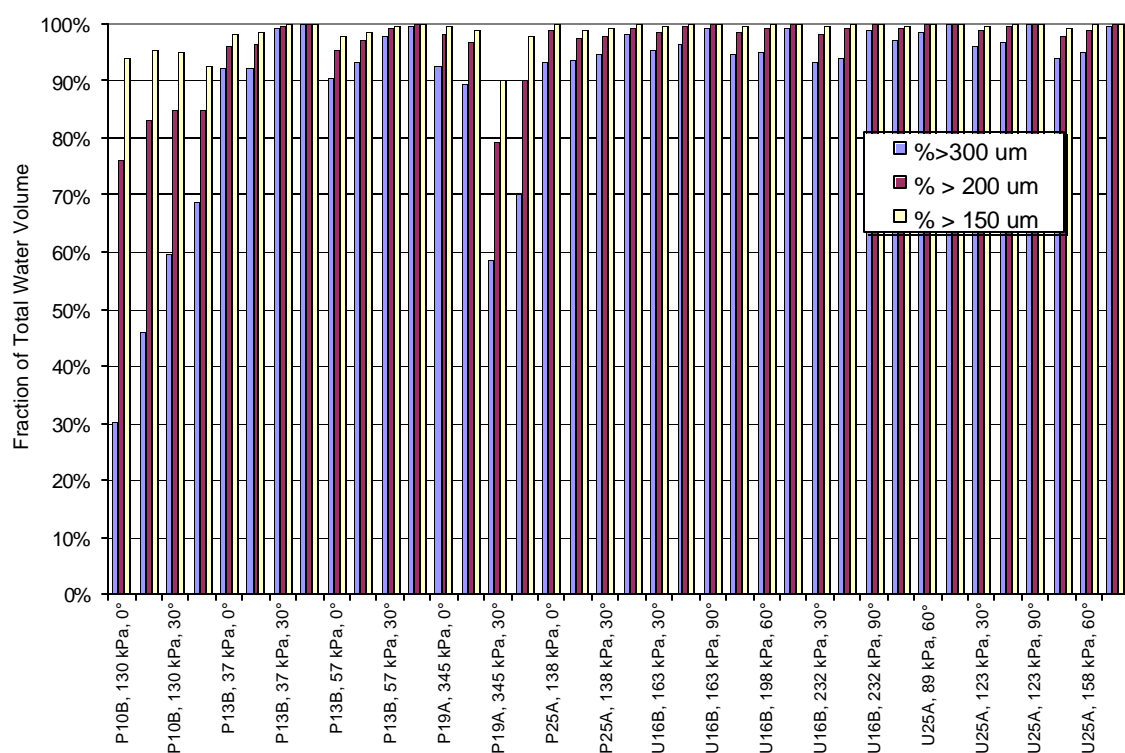
Figure 66. Fraction of Water Visible in Laser Sheet Images

The results in Figure 66 indicate that the fraction of the water visible in the CCD

images was close to 100% for most laser sheet experiments. The consequence of this

finding is that the use of PIV at the resolution used in the experiments described in

Chapter 5 provides velocity results that characterize the portion of droplets in a sprinkler

spray that deliver near all of the water to a fire.

6.2   Measurements on Horizontal Plane Below Sprinkler

Droplet size measurements were also conducted along a horizontal plane 1 meter below the P19B, U16B, and U25C sprinklers as shown in Figure 54. Measurements were made at six azimuthal angles and at a variety of radial distances from the axis of the sprinkler out to a maximum distance of 2.6m. These measurements were much more difficult to make than the measurements near the sprinkler because of the extremely low data rates. As the distance from the sprinkler increased the data rate decreased until at distances greater than one meter from the data rates of 1 Hz or less were often observed. Eighty-five (85) tests were conducted below the sprinkler of which 40% would have been discarded because of low data counts if they were used individually. Instead, the data from all azimuthal angles were combined for each radial distance, X.   This approach provided enough data for a statistically significant sample, but the tradeoff was that any information about the azimuthal dependence was lost. The minimum number of droplets used in the analysis was 2261 for the P19B at 2.64m. The average number of droplets for each horizontal distance was 35800. A summary of the results of the combined tests is presented in Table 9.

Table 9. PDI Experiments 1m below Sprinkler

Sprinkler	Pressure (kPa)	Z (m)	X (m)	Droplet Count	d_1 (μm)	d_2 (μm)	DV50 (μm)
P19B	345	1	0	6163	269	605	917
P19B	345	1	0.29	51263	208	366	568
P19B	345	1	0.58	58041	195	288	497
P19B	345	1	1.18	53492	281	401	454
P19B	345	1	2.04	14990	681	857	898
P19B	345	1	2.64	2268	142	951	1050
U16B	345	1	0	22879	128	166	207
U16B	345	1	0.29	60511	134	172	216
U16B	345	1	0.58	101972	230	474	719
U16B	345	1	1.18	100051	285	527	732
U16B	345	1	2.04	5692	298	1082	1156
U25C	138	1	1.30	18918	505	616	754
U25C	138	1	2.26	2800	1162	1293	1373

For all sprinklers, the equivalent droplet diameters, d_1, d_2, and DV50 increased with increasing radial distance. It seems logical that this relationship would be caused by the dependence of trajectory on droplet size. The ballistic model in Section 1.7 suggests that the maximum horizontal distance that a droplet can travel is a function of the droplet size and the initial velocity of the droplet. In the velocity analysis it was found that the maximum velocity was typically on the same order as the velocity of the water through the sprinkler orifice. If this initial velocity is used as an input into a ballistic calculation, the minimum droplet size that can travel to any horizontal position can be calculated.

The orifice velocities for the P19B, U16B and U25C were 22, 25, and 14 m·s^{-1}, respectively. A trajectory calculation was conducted to determine the maximum distance

that various sized droplets with these initial velocities could travel radially during 1m of vertical fall. The droplets in the calculation were ejected horizontally from the sprinkler to maximize the radial distance. Figure 67 shows DV50 as a function of radial distance for trajectory calculations and the experimental results. The trajectory curves represent the maximum radial distance that a droplet of a given diameter could travel according to the trajectory analysis. All of the experimental results in Figure 67 indicate a radial distance traveled that is less than that predicted from the trajectory analysis. Nevertheless, the trend in the experimental data matches that in the trajectory analysis, except for small radial distances where other factors may play a role.
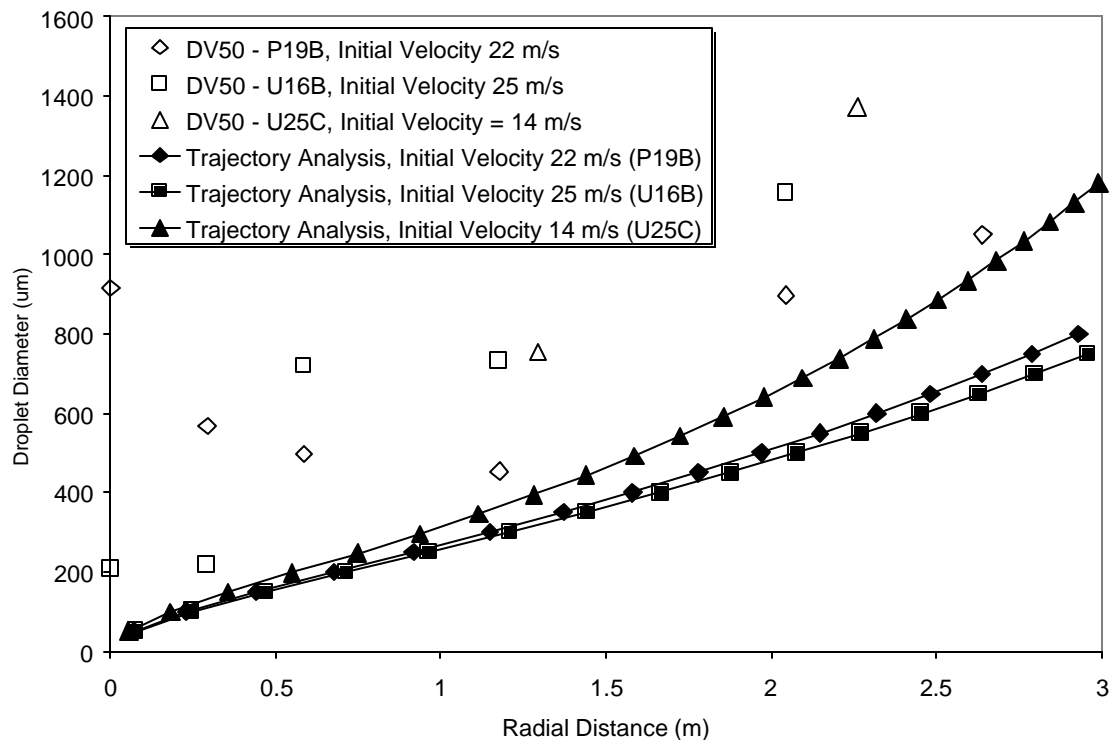
Figure 67. Volume median diameter as a function of horizontal distance.

6.2.1 Droplet Size Distributions

Figure 68 through Figure 71 show histograms, cumulative count, and cumulative volume flux for the P19B sprinkler for distances from the sprinkler of 0.29, 1.18, 2.04 and 2.64m respectively. At distances less than 1.18m from the sprinkler the shape of the histograms remained similar to the example in Figure 68. At the 1176mm distance shown in Figure 69 the histogram's shape begins to change by broadening in the $200 \leq d \leq 700 \mu m$ region.
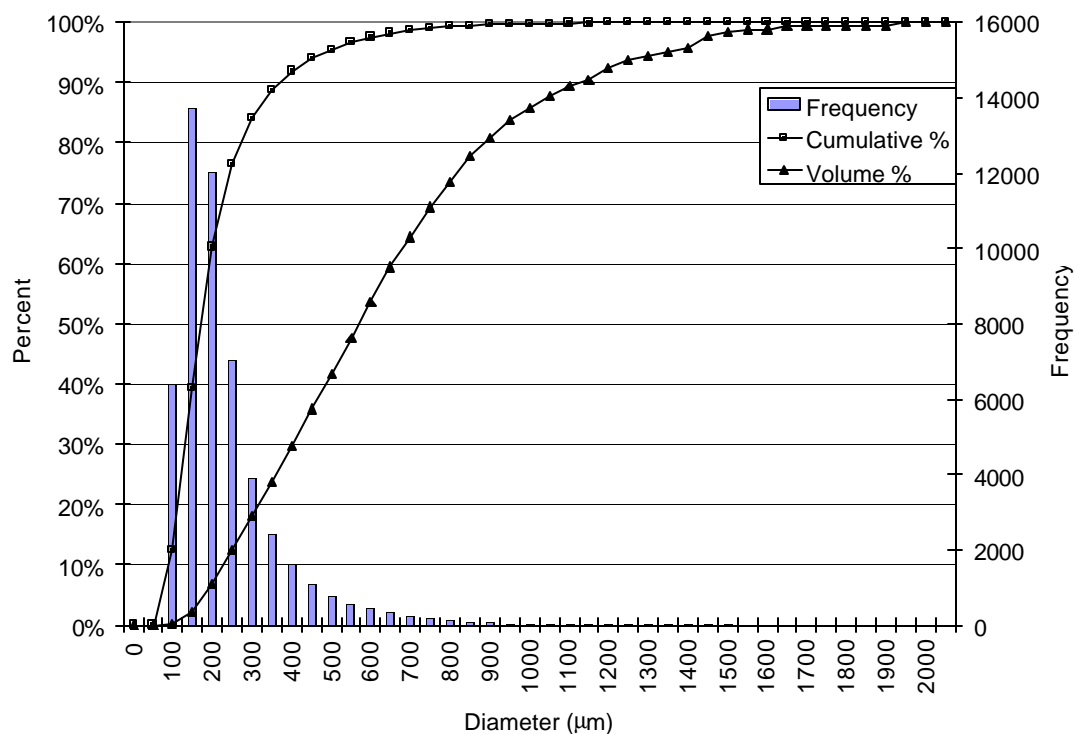
Figure 68. Droplet sizes 1m below and 0.29m horizontal distance from P19B
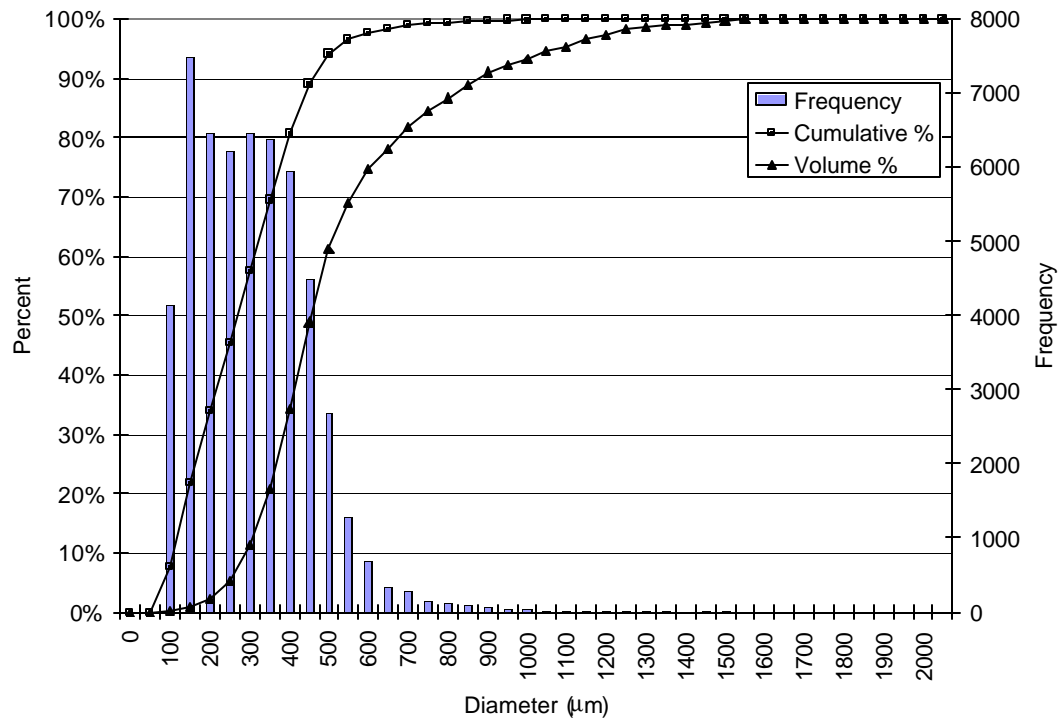
Figure 69. Droplet sizes 1m below and 1.18m horizontal distance from P19B

At the 2.04m distance shown in Figure 70 the histogram displays a bimodal hump and the 2.64m shown in Figure 71 there also appears to be a bimodal hump although the second shape in the distribution is quite low. This bimodal histogram could be anticipated by the trajectory analysis that suggested that the distance that a droplet could traverse from the spray origin is a function of the droplet size. This means that as the distance from the sprinkler increases more of the small droplets will fall out of the spray. The smallest droplets (d< 200 μm) are so small that they are carried by the air flow entrained with the spray. Therefore, a possible reason for the bimodal distribution is that as the distance from the sprinkler increases, the largest droplets can traverse the distance, but in addition, the very smallest droplets are also carried along by the air flow to any distance.

Figure 70. Droplet Sizes 1m below and 2.04m horizontal distance from P19B
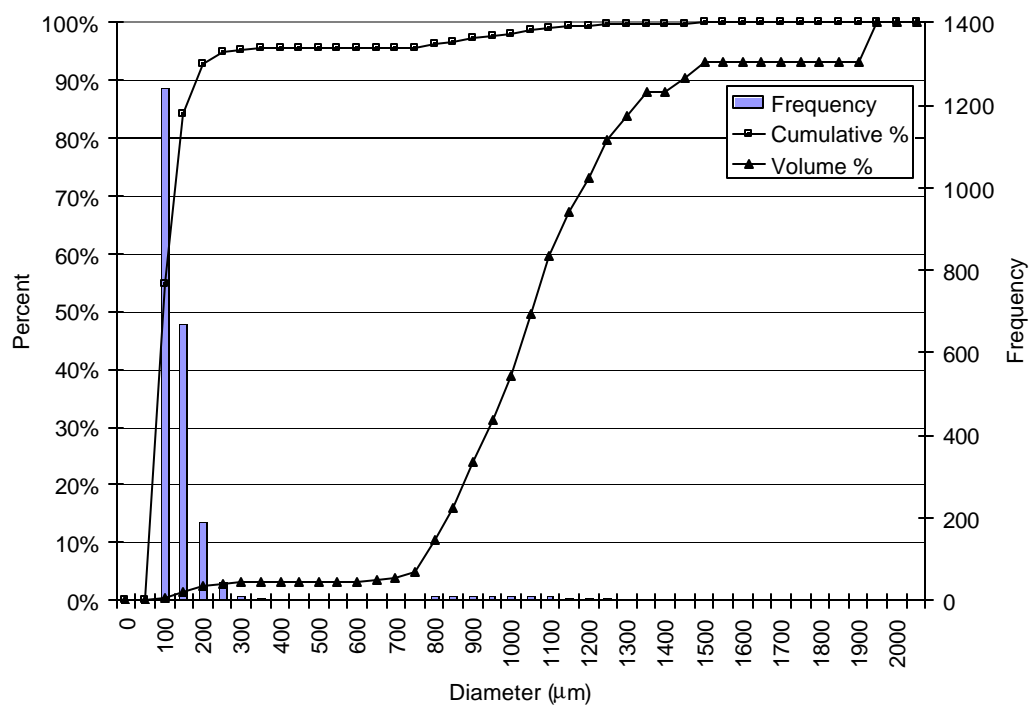
Figure 71. Droplet Sizes 1m below and 2.64m horizontal distance from P19B

Figure 72 through Figure 74 show histograms, cumulative count, and cumulative volume flux for the U16B sprinkler for distances from the sprinkler of 0.29, 1.18, and 2.04m respectively. Results from the tests at 2.64m from the sprinkler were discarded due to low droplet counts. The maximum number of droplets is always found in the $100 \leq d \leq 200\mu m$ region, but as the distance from the sprinkler increases the proportion of droplets in the $d>200\mu m$ region increases. Again a bimodal distribution is observed at the 2.04m distance shown in Figure 74.
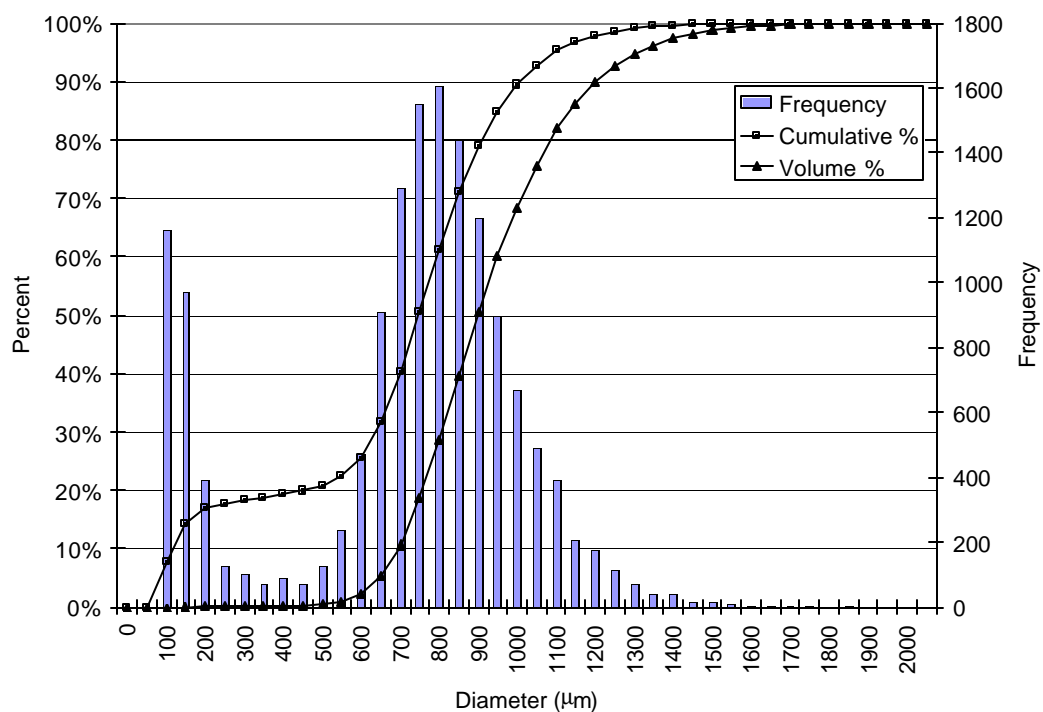

Figure 72. Droplet Sizes 1m below and 0.29m horizontal distance from U16B
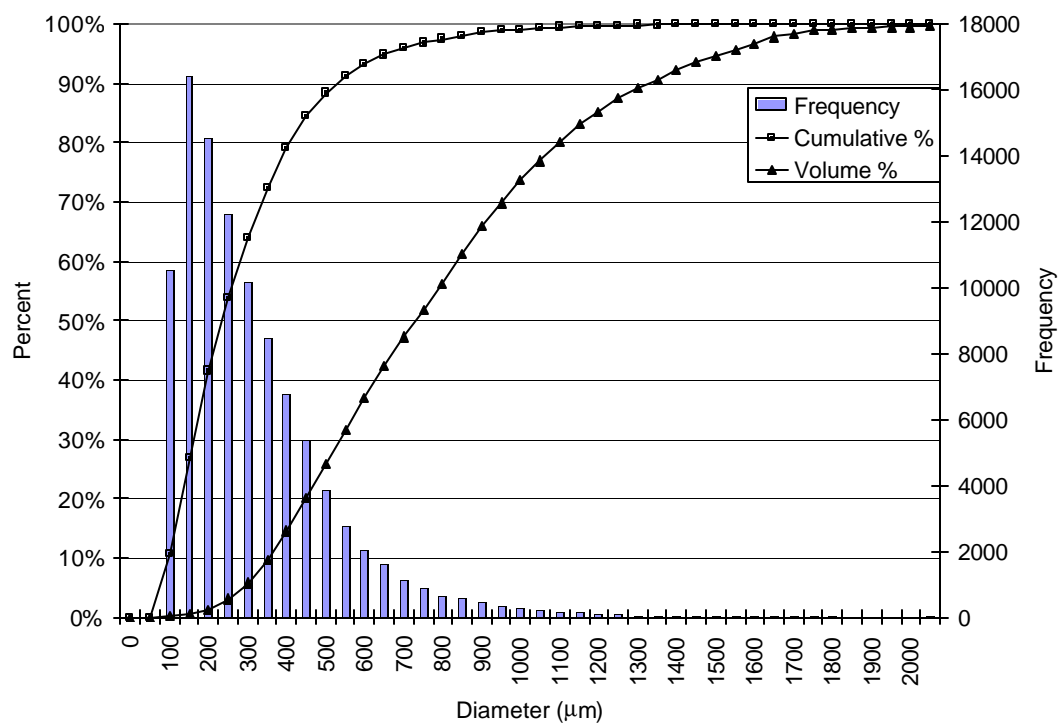
Figure 73. Droplet Sizes 1m below and 1.18m horizontal distance from U16B

Figure 74. Droplet Sizes 1m below and 2.04m horizontal distance from U16B

Histograms of the droplet sizes for X=1.30m and X=26m for the U25C sprinkler are shown in Figure 75 and Figure 76 respectively. At X=1.30m the maximum number of droplets are located in the $400 \leq d \leq 600\mu$m region and at X=2.26m in the $1000 \leq d \leq 1300\mu$m region. However it is clear that mostly larger droplets are present at the larger radius, consistent with the particle tracking analysis in Chapter 1.
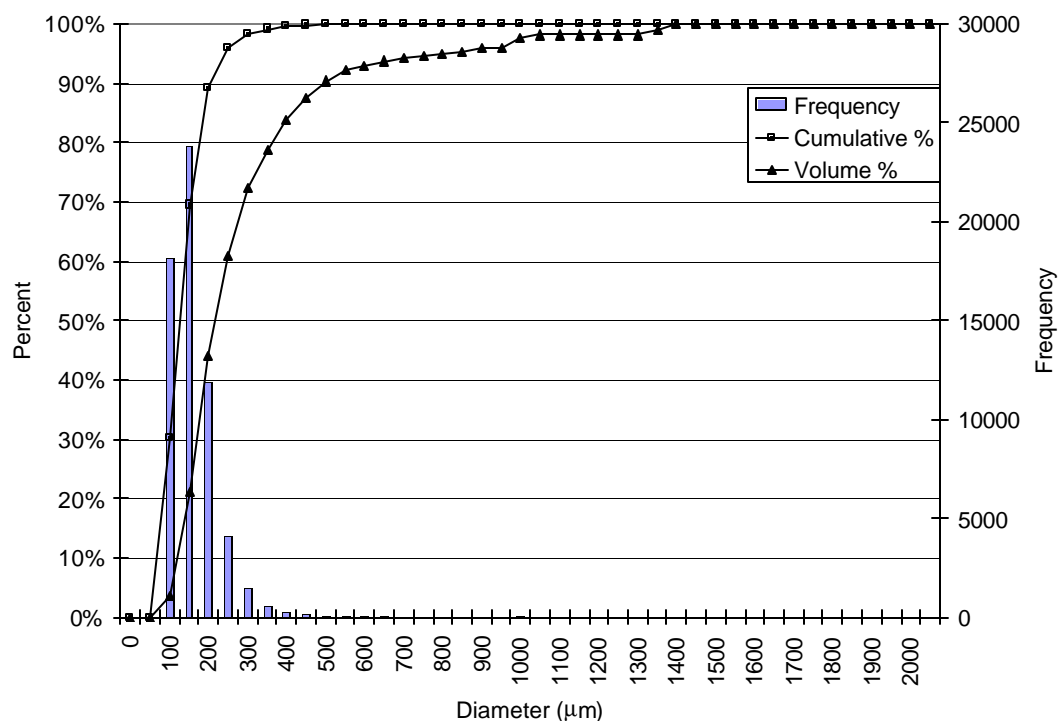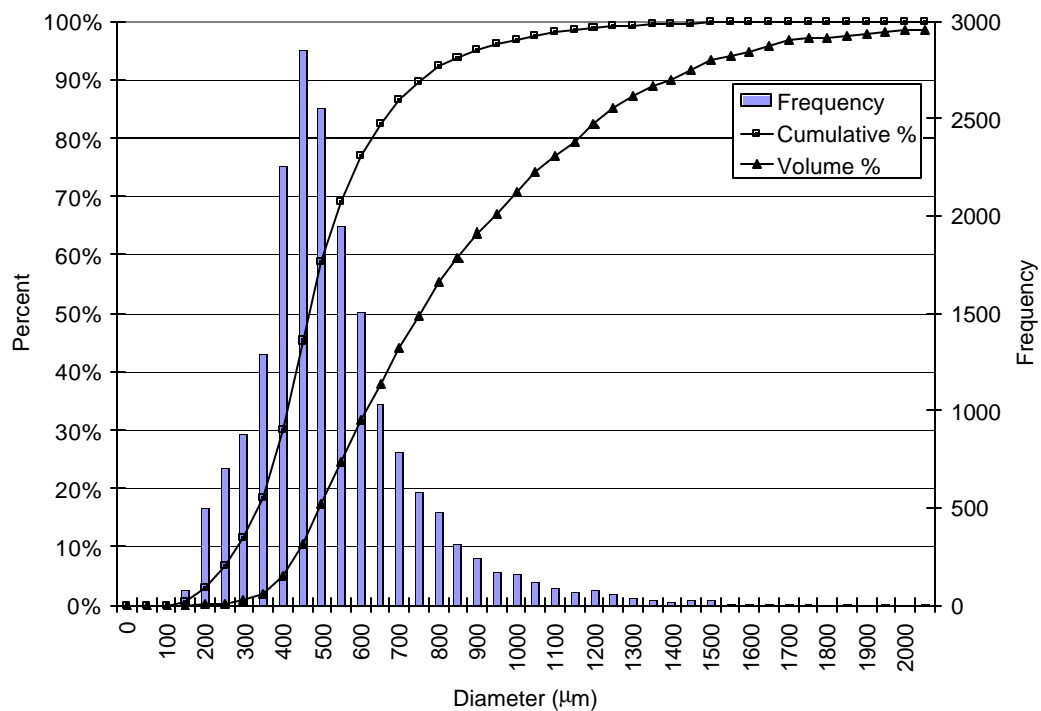

Figure 75. Droplet Sizes 1m below and 1.30m horizontal distance from U25C

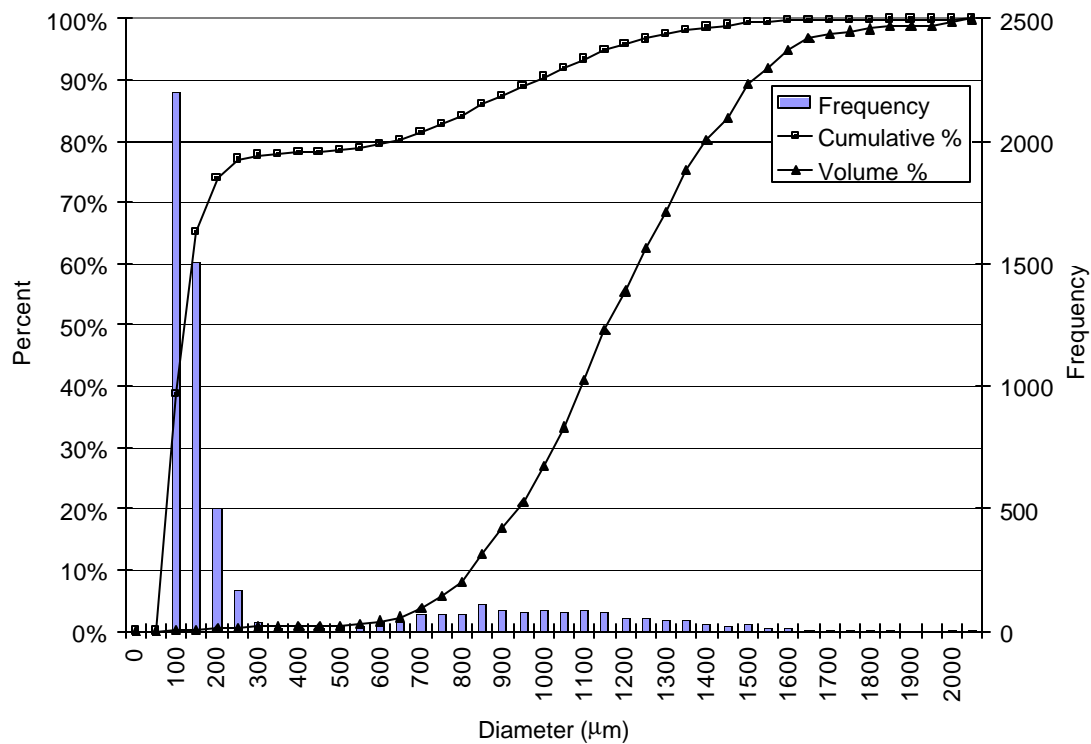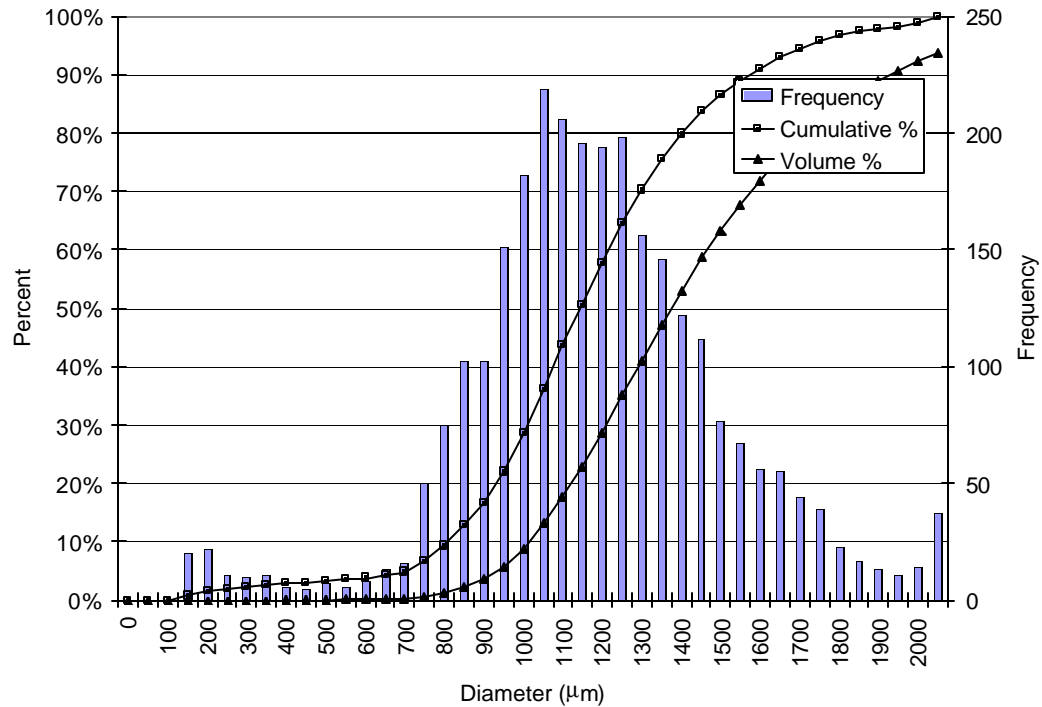**Figure 76. Droplet Sizes 1m below and 2.26m horizontal distance from U25C**

6.2.2   Droplet Distribution Function

The droplet distribution functions were also evaluated for the measurements in a plane below the sprinklers. Three regions were found in the P19B spray where the droplet distribution curves had similar shapes. These similar regions were 1) 0, 0.292, and 0.584m 2) 1.176m and 3) 2.044 and 2.641m. Region 1 was found to conform with a Rosin-Rammler above the volume median diameter and a log-normal below the volume median diameter. Region 2 was found to conform to a Rosin-Rammler above the volume median diameter. Region 3 conformed to a log-normal distribution for all except the smallest droplets that were much smaller than droplets in a log-normal distribution. These smallest droplets, which comprised of less than 1% of the water volume, were in

the bimodal region observed in the histograms. Typical charts from the three regions

representing the CVF measured at 0.292, 1.176 and 2.044m are shown in Figure 77

through Figure 79 respectively.
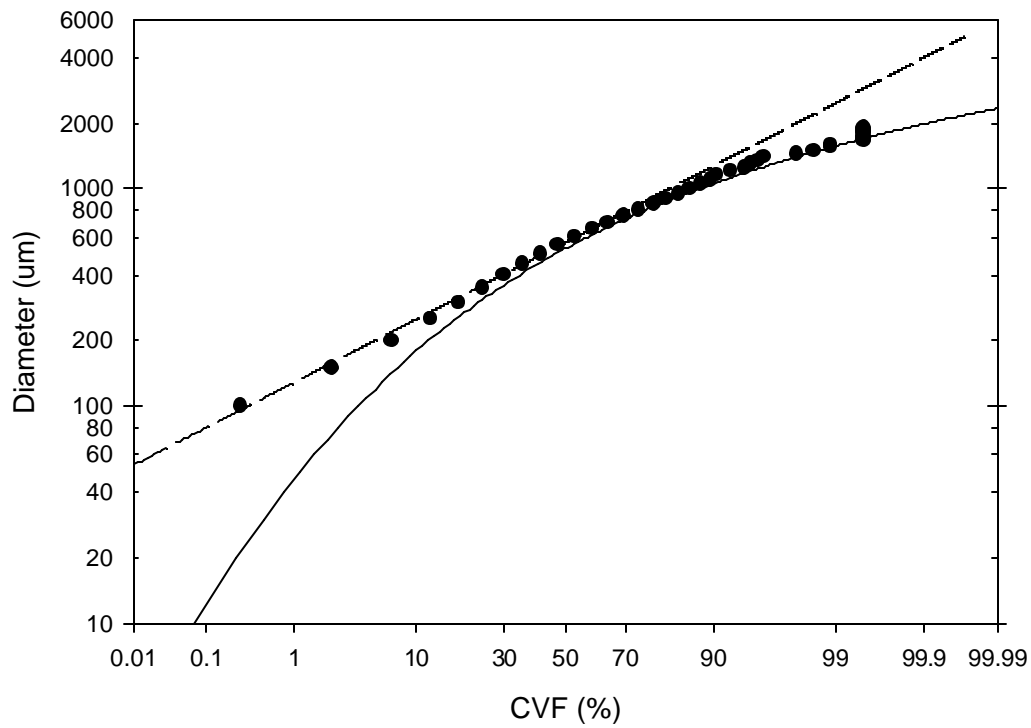
Figure 77. CVF of P19B sprinkler at X = 0.292m
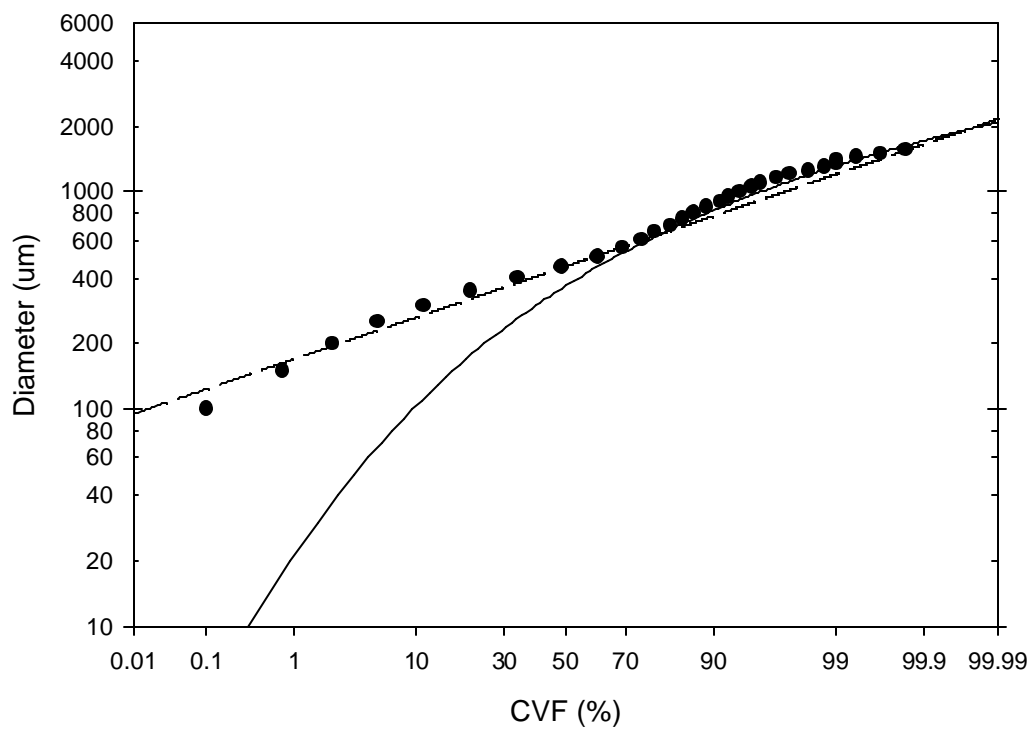
Figure 78. CVF of P19B sprinkler at X = 1.176m
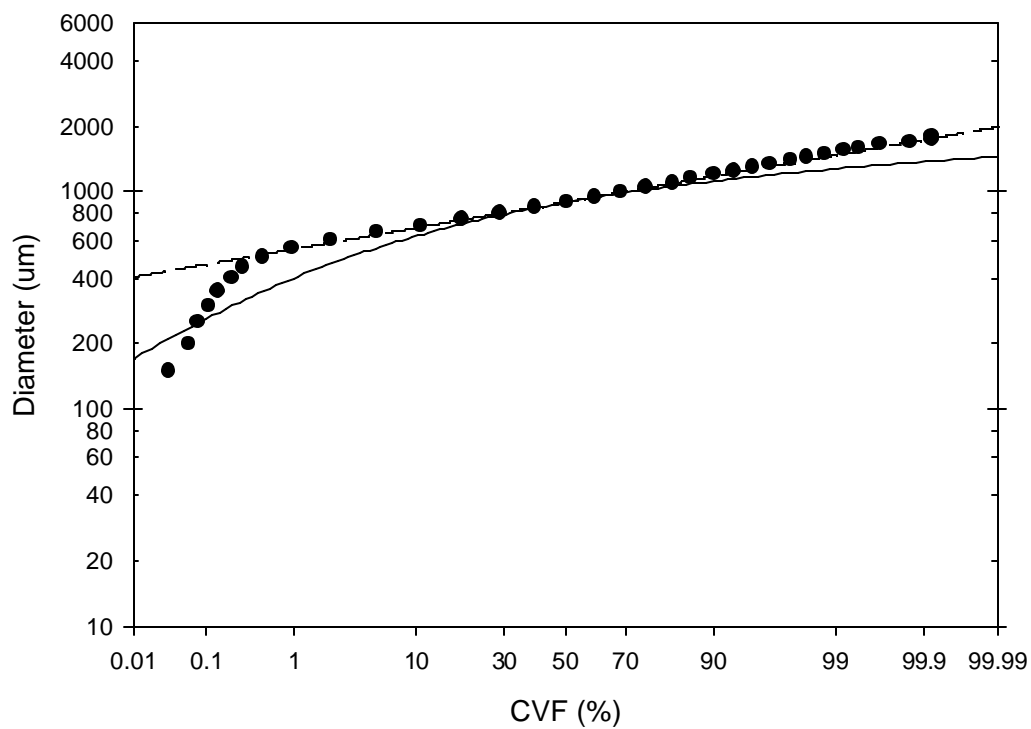
Figure 79. CVF of P19B sprinkler at X = 2.044m

Typical charts from the three regions representing the ddf measured at 0.292, 1.176 and 2.044m for the U16B sprinkler are shown in Figure 80 through Figure 82 respectively. Three regions with similarly shaped CVF curves were found. These similar regions were 1) 0, and 0.292m, 2) 0.584 and 1.176m and 3) 2.044 m. Droplets in region 1 were found above log-normal line when the droplets were larger than the volume median diameter and were log-normal below the volume median diameter which is different from the P19B sprinkler   Region 2 was similar to region 1 in the P19B sprinkler and was found to conform with a Rosin-Rammler above the volume median diameter and a log-normal below the volume median diameter. Region 3 was similar to region 3 in the P19B sprinkler and conformed to a log-normal distribution for all except the smallest droplets that were much smaller than droplets in a log-normal distribution. These smallest droplets, which again comprised of less than 1% of the water volume, were in the bimodal region observed in the histograms.
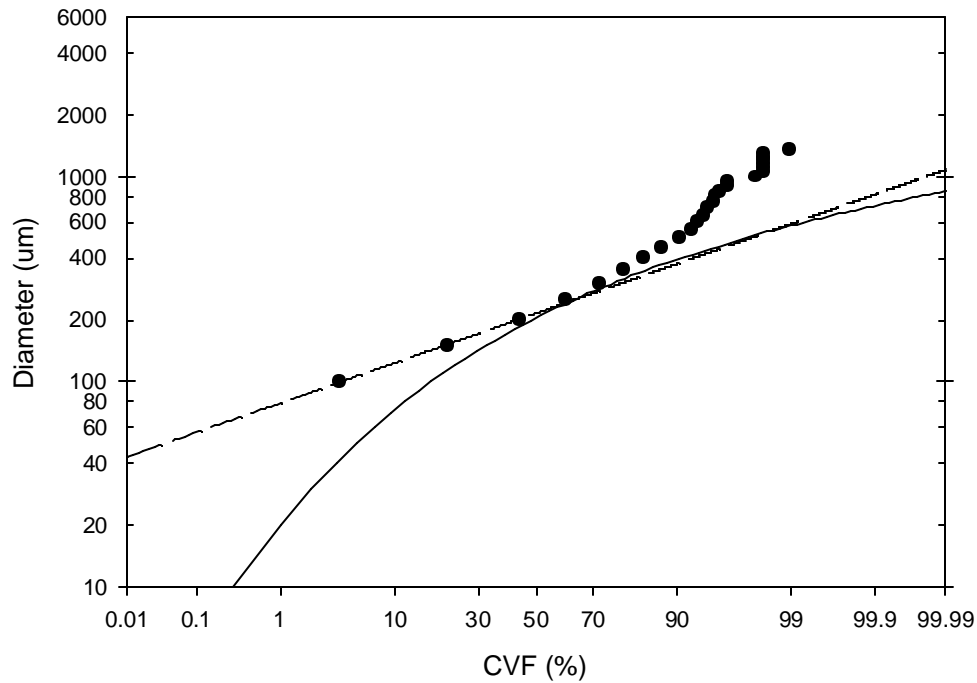
Figure 80. CVF of U16B sprinkler at X = 0.292m

It is reasonable to assume that the differences between the shape of the CVF close to the upright sprinkler and further away are due to the influence of the branch line interfering with the spray. The branch line for upright sprinklers was located directly below the sprinkler may have caused more collisions between droplets thus causing more larger droplets to be formed.
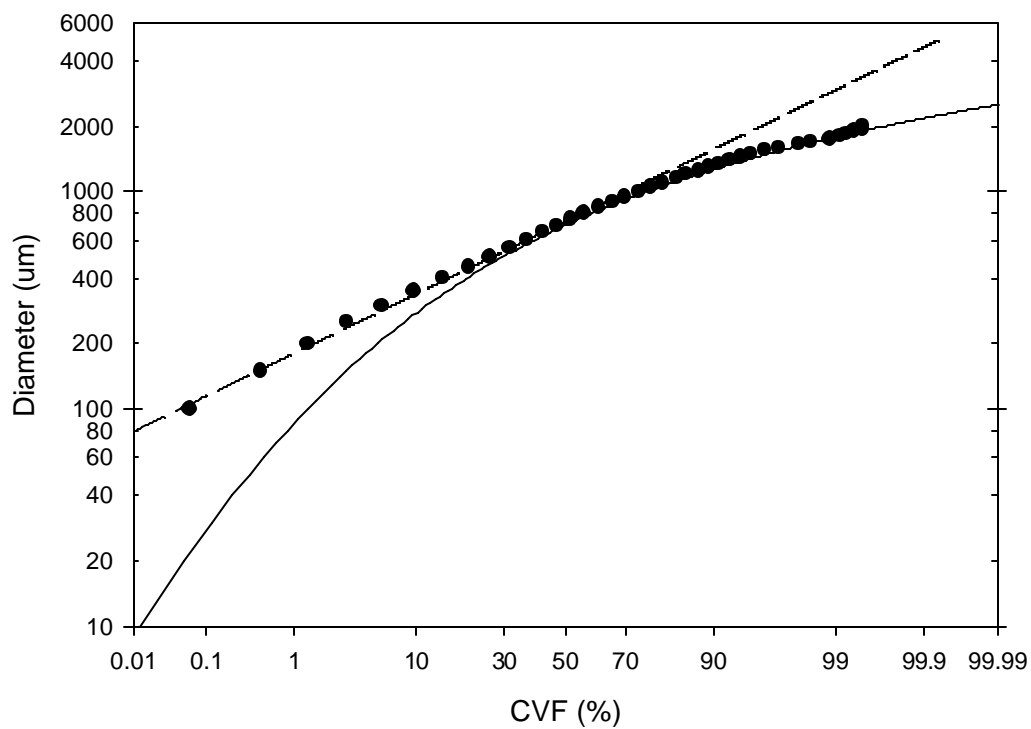
Figure 81. CVF of U16B sprinkler at X = 1.176m
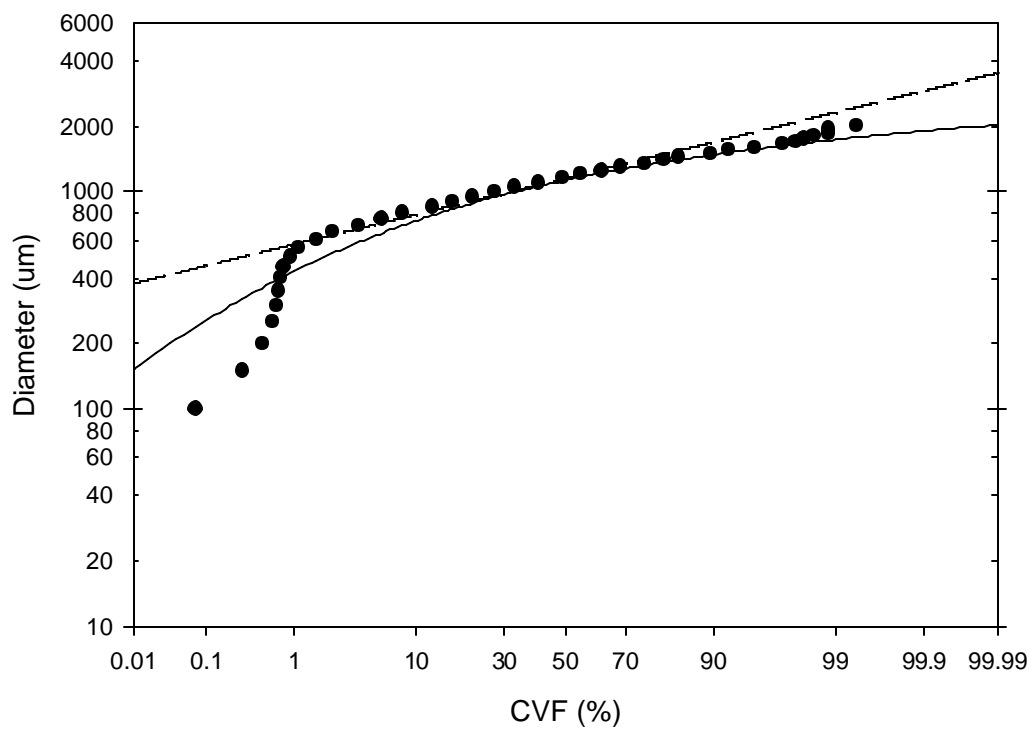
Figure 82. CVF of U16B sprinkler at X = 2.044m

The CVF for the 1.295 and 2.260m measurement locations for the U25C sprinkler are shown in Figure 83 and Figure 84 respectively. The droplet sizes measured at 1.295 and 2.260m both exhibited a log-normal distribution. The measurement at 2.260m exhibited the smaller than log-normal behavior observed in the P19B and the U16C sprinkler. Surprisingly the measurement at 1.295m did not have these smaller droplets.
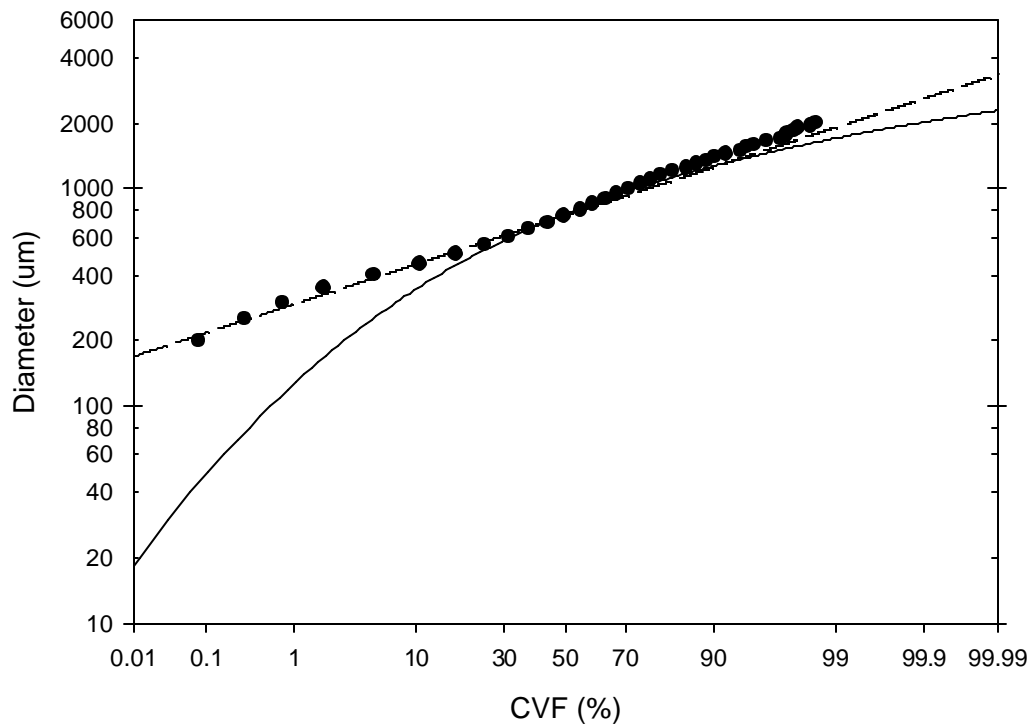
Figure 83. CVF of U25Csprinkler sprinkler at X = 1.295m
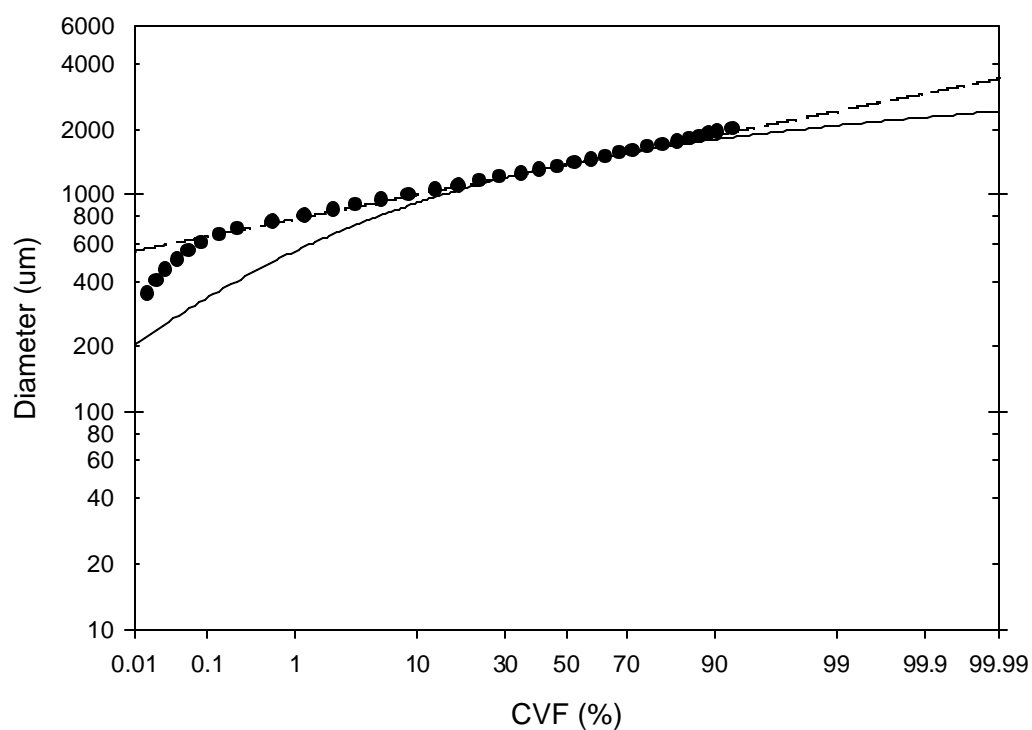
Figure 84. CVF of U25Csprinkler sprinkler at X = 2.260m

The results of the CVF analysis are summarized in Table 10. A description of the shapes of the CVF function is provided in the third column. The calculated constants for the log-normal and Rosin-Rammler distributions are tabulated in the last four columns.

Table 10. Standard Distribution Constants

Sprinkler	X (m)	Distribution below DV50	Distribution above DV50	DV50 (µm)	β (µm)	γ (µm)	σ_ln (µm)
P19B	0	Log-normal	Rosin-Rammler	917	0.661	2.065	0.691
P19B	0.292	Log-normal	Rosin-Rammler	568	0.721	1.739	0.635
P19B	0.584	Log-normal	Rosin-Rammler	497	0.653	1.735	0.612
P19B	1.176	Near log-normal [1]	Rosin-Rammler	454	0.869	1.490	0.420
P19B	2.044	Log-normal [2]	Log-normal	898	0.611	5.311	0.214
P19B	2.641	Log-normal [2]	Log-normal [3]	1050	0.630	5.090	0.234
U16B	0	Log-normal	Above log-normal [1]	207	0.620	2.114	0.442
U16B	0.292	Log-normal	Above log-normal [1]	216	0.611	1.819	0.434
U16B	0.584	Log-normal	Rosin-Rammler	719	0.720	1.878	0.685
U16B	1.176	Log-normal	Rosin-Rammler	732	0.701	2.028	0.599
U16B	2.044	Log-normal [2]	Rosin-Rammler	1156	0.693	4.408	0.300
U25C	1.295	Log-normal	Log-normal	754	0.612	2.366	0.402
U25C	2.260	Log-normal [2]	Log-normal	1373	0.615	4.622	0.245

Notes:
The CVF did not conform to a standard distribution function
The smallest droplet sizes were below the log-normal curve due to the bimodal shape of the number distribution curve.
The largest droplets were above the log-normal curve probably due to the low number count used in the test's analysis.

It was evident that as the distance from the sprinkler increased, the standard deviation, σ_{ln}, for the log-normal CVF tended to decrease as shown in Figure 85. The σ_{ln} is a measure of the range of droplet sizes that make up the delivered water volume. As σ_{ln} decreases the range of droplet sizes delivering the bulk of the water decreases. Figure 85 shows that close to the sprinkler there is significant variability in σ_{ln}. At large distances from the sprinkler, $X > 2$ m, σ_{ln} is much smaller and has less variability. This is probably a consequence of only larger droplets being present at the larger horizontal

distances, as indicated from the trajectory analysis. As a consequence of only larger

droplets being present at greater radii, the overall range of droplets sizes is less, reducing

σ_{ln}.
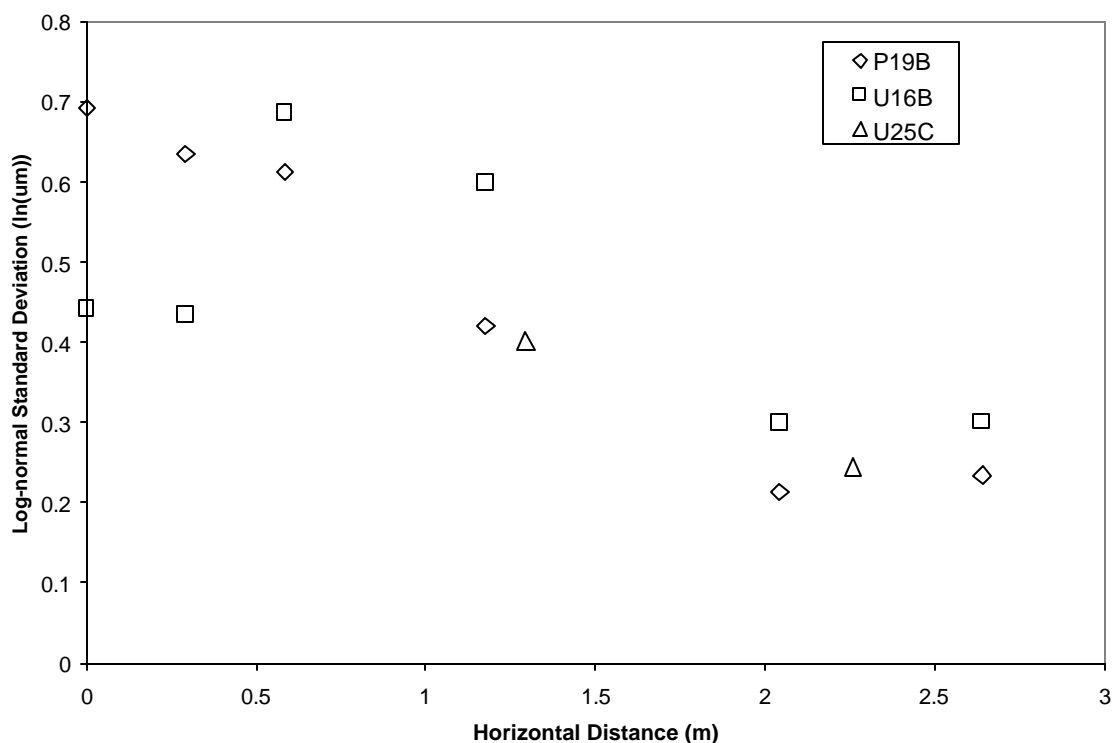
Figure 85. Log-normal standard deviation

The constant β for the curves conforming to a Rosin-Rammler distribution

remained relatively constant regardless of sprinkler or location. The β values ranged

from 0.6 to 1.0 with an average of 0.69 and a standard deviation of 0.12. In order to

determine if the constants were similar to historical results, a t-test was conducted

comparing the β from this study to the values published by You[34]. The t-test showed

that there is only a 72% chance that the mean of this data-set match You's results. This

means that it is unlikely that this data is similar to You's. Not matching You's data is not

unexpected since the constants were found to depend on the sprinkler and You's sprinklers were not tested in this study.

The constant γ for the curves conforming to a Rosin-Rammler distribution was independent of sprinkler type. There was a general trend of increasing γ with distance, but the relationship was somewhat. A very weak correlation coefficient, r^2, of 74% was the best that could be obtained from a linear correlation.

6.3   Conclusion

The following conclusions can be made from the results discussed in this chapter.

➤ Sprinkler sprays are composed of a large number of droplets with diameters that span 2 orders of magnitude. The largest number of droplets are typically less than 250μm in diameter, but the majority of the water volume is typically carried by droplets with diameters greater than 300μm.

➤ Near the sprinklers more large droplets were present as the elevation angle increased. It was observed that a few large droplets often dominated (20% to 40%) the water volume at a measurement point. The importance of a seldom occurring large droplet having significant impact on the results indicates that long sample times are required for droplet size analysis. The experiments in this project were conducted for at least 15 minutes, which might be considered the minimum time required for an adequate sample.

➢ The shape of the CVF near the sprinklers was found to depend on the sprinkler type, the elevation angle, and the water pressure. The shape of the CVF was unique for each sprinkler and location. In a limited number of cases (less than 50%) the CVF was found to conform to a log-normal, Rosin-Rammler or combination log-normal/Rosin-Rammler distribution. When the CVF curves conformed to a standard distribution, the constants for the distributions were unique for each sprinkler/elevation angle/water pressure combination and no relationship could be found between the constants and location or water pressure. This result demonstrates that until a fundamental understanding is developed of the droplet creation process from the deflector to the regions of fully developed droplet flow, the only method of determining droplet size distributions will be experimental testing at multiple locations and at a variety of pressures.

➢ The results of this analysis indicate that the volume median diameter is proportional to the inverse cube root of the Weber number as postulated by Dundas [45]. However, the 2.7 proportionality constant that was put forth in the past [46] is not universal for all sprinklers. The proportionality constants measured in this study ranged from 0.72 to 2.48 with an average of 1.53. The proportionality constant is a function of the sprinkler design and the location in the spray.

➢ The trajectory analysis from Chapter 1 suggests that the maximum horizontal distance that a droplet can travel is a function of the droplet size and the initial velocity of the droplet. Larger droplets are able to travel further than smaller ones. These

experiments corroborate the results of the trajectory analysis and suggests that the minimum median volume diameter below sprinklers could be estimated at any location using trajectory analysis.

7   Water Flux

Information about water flux is used in a different manner than information about velocity and droplet size distribution. Knowledge of the initial droplet velocity and droplet size determines where an individual droplet will travel based on the trajectory of the droplet. The water flux, on the other hand, defines how much water is transported to each location below the sprinkler. From the standpoint of fire suppression, water flux is often considered the most important of the three types of sprinkler spray information.

Visual observations demonstrate that the water flux is not constant throughout the spray. The water flux changes as both a function of elevation angle and azimuthal location. An example of this is shown in the two laser sheet images in Figure 86. The two images represent results from the P10A sprinkler at 48 kPa at azimuthal angles parallel to the frame arms, $\theta = 0°$, and perpendicular to the frame arms, $\theta = 90°$. For each image it is clear that the water concentration is a function of elevation angle with both images exhibiting low droplet count directly below the sprinklers, higher droplet counts as the elevation angle increases, and few or no droplets observed as the elevation angle increases above the horizontal. The images in Figure 86 also demonstrate the variability of water concentration with azimuthal angle. Parallel to the frame arms there appears to be high water concentrations at elevation angles up to $\phi \leq 105°$. Perpendicular to the frame arms the high water concentrations end at a much lower elevation angle of approximately $\phi < 70°$. For this reason, a single global value for the water flux of a sprinkler could not fully describe the water flux, and measurements at many locations in the spray are required.   149

q = 0°   **q = 90°**
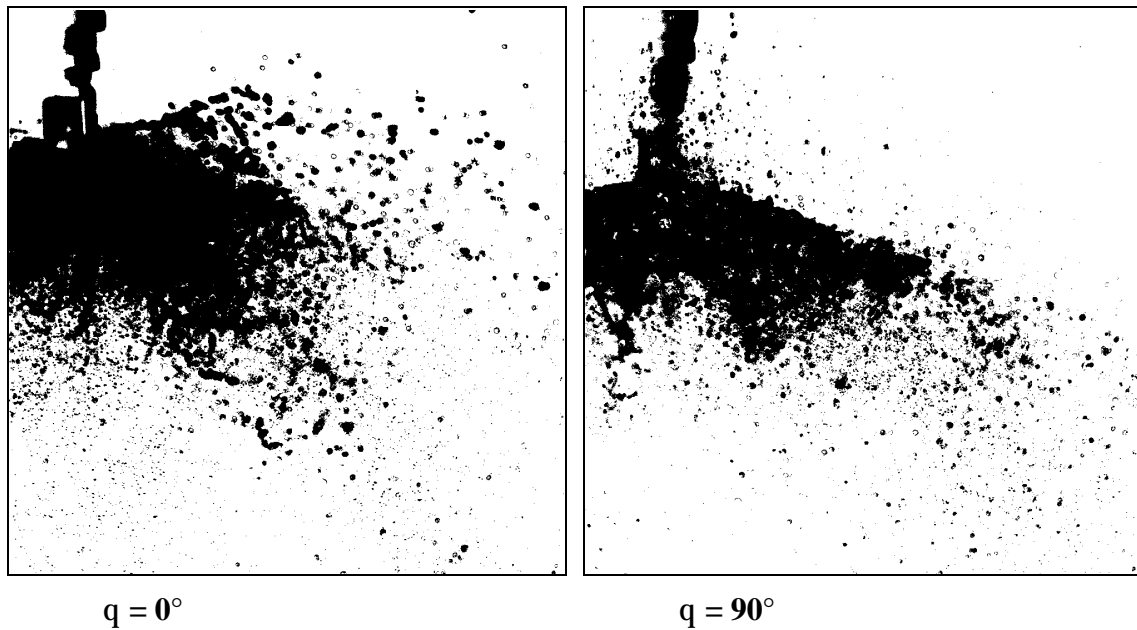
Figure 86. Image of Spray from P10A at q = 0° and q = 90°

Many techniques are available for measuring the water flux. The simplest method is to collect water at the areas of interest using pans. This method has been used for many years using 0.3m square pans placed on a horizontal plane either 1m or 3m below the sprinkler [47]. A second approach would be to use PDI to measure flux. In a PDI flux measurement, the exact size and number of droplets through a small probe volume recorded over time could be used to find the flux at that location. Unfortunately, the probe volume of the PDI technique is extremely small and the number of measurements required to completely map the region around a sprinkler makes this approach prohibitively expensive. A third method developed for use in this in this study is based on counting droplets in the laser sheet images to estimate the water flux.

7.1   Calculating Water Flux

The mass water flux is simply the mass flow rate of the water through a surface. In simplest terms the mass water flux, $\dot{m}''$, can be quantified as

$$\dot{m}'' = \dot{m}/A \qquad\qquad 7.1$$

where $\dot{m}$ is the mass flow rate in kg·sec^{-1}, A is the area through which the water is flowing in m², and the mass water flux is in units of kg·sec^{-1}·m^{-2}.

For sprinkler applications, the volumetric water flux is a better parameter to report than the mass water flux because the quantity of interest is amount of water coverage. The volumetric water flux is simply the volume flow rate of the water through a surface. The volumetric water flux, $\dot{q}''$, can be quantified as

$$\dot{q}'' = \dot{q}/A \qquad\qquad 7.2$$

where $\dot{q}$ is the volumetric flow rate of the water in the control volume in m^3·sec^{-1} and the volumetric water flux is in units of m·sec^{-1}. The conversion factor from mass flow rate, $\dot{m}$, to the volumetric flow rate, $\dot{q}$, is the water density, ρ, in kg/m^3.

Since a spherical coordinate system is most appropriate for the analysis of fire sprinklers, the differential areas of interest, dA, are located on the surface of a sphere as shown in Figure 87. The impact of this choice of coordinate systems is that the areas are of different size depending on the elevation angle, ϕ. For a spherical differential area

element, $dA = r^2 \sin\phi \, d\theta \, d\phi$, where r is the radius of the sphere and θ and ϕ are the azimuthal angle and elevation angle as shown in Figure 87.
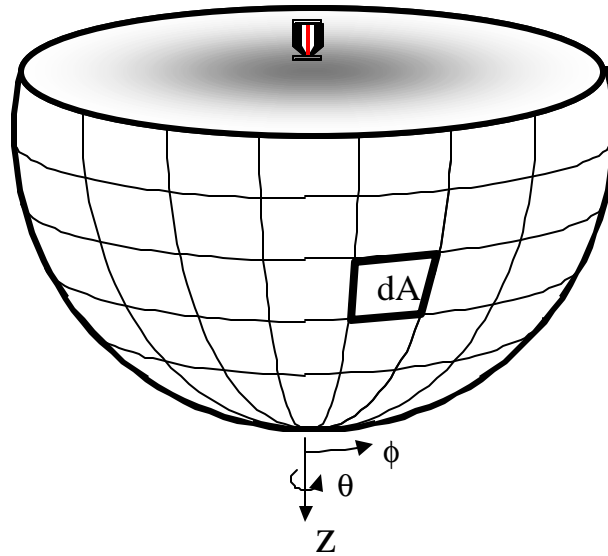
Figure 87. Coordinate system for water flux

Two techniques were considered for calculating the water volume fraction in the spray from the laser sheet images: 1) calculating the area of the visible droplets in an image and assuming that the sum of volumes is proportional to the water volume fraction, 2) counting the number of droplets in a region and assuming the count of droplets is proportional to the volume fraction of water.

Calculating the water volume fraction based on the area of the droplets in the image requires that the area of the droplets be clearly visible and measurable in the images. The resolution of the image has to be fine enough to resolve the droplet size to provide an estimate of the droplet volume. The advantage of this technique is that the calculation is a direct measurement with very few assumptions required. However,

Atreya and Everest[48] have demonstrated that the type of laser sheet illumination that was used in this study to illuminate the droplets by scattered light may produce errors in droplet size estimates. These errors are apparently due to the fact that droplets that are not bisected by the laser sheet are not uniformly illuminated for their entire diameter. As a result, the droplet image may be smaller than the actual droplet size. Thus, the diameter of the droplet estimated from the area in a laser sheet image is highly dependent on its location relative to the laser sheet. An alternative to avoid this situation is to use a fluorescing dye in the sprinkler water. When illuminated by a laser sheet, the dye causes the entire droplet to be visible regardless of where the laser sheet intersects it. However, this was not possible here, so droplet sizes could not be estimated accurately.

Calculating the water volume fraction by estimating the droplet count requires the assumption that the number of visible droplets in the image be proportional to the total water volume in the image. The nominal resolution of the images in the tests was 300 μm/pixel. If the assumption is made that all droplets with diameters greater than or equal to the image resolution in the experiments are visible in the image, then the droplet size analysis in Chapter 6 shows that the droplets with diameters on the order of 300μm and greater typically make up at least 90% of the volume of the water in a region. Since the unresolved small end of the size distribution is responsible for less than 10% of the water volume, it is reasonable to assume that nearly all of the water volume can be accounted for by counting drops. Therefore, the count method of estimating water density was used for this study.

Based on this method, the differential volume of water, dq, in a differential measurement volume, dV is

$$dq = \frac{\boldsymbol{p} D^3}{6} N \, dV \qquad 7.3$$

where D is the average droplet diameter and N is the number density of droplets in a unit volume, V. The differential volume, $dV = r d\boldsymbol{f} \, dr \, dL$, is approximately $6.3\text{E-}5\text{m}^3$ where r is the radius of the sphere, the differential elevation angle $d\phi$ has been defined as $\pi/60$ (3°) increments, the differential radius, dr, has been defined as the 50mm wide region of bounded by $175\text{mm} \leq r \leq 225\text{mm}$, and dL is the thickness of the laser sheet which is approximately 1mm. It is important to note that the volume, dV, in this equation is the thin region dL wide where the laser sheet bisects the sphere and is not the much larger volume between the two measurement planes that are $\theta = 5°$ apart.

If the average diameter of the visible droplets is assumed to be a constant throughout the spray at a given radial distance then the water volume fraction as a function of elevation angle and azimuthal angle is

$$q'''(\boldsymbol{f}, \boldsymbol{q}) = \frac{q}{V} = \frac{\boldsymbol{p} D^3}{6} N(\boldsymbol{f}, \boldsymbol{q}) \qquad 7.4$$

Because the average diameter in equation 7.4 is assumed to be a constant, the water volume fraction, $q'''(\boldsymbol{f}, \boldsymbol{q})$, in any region is proportional to the experimental droplet number count, $N(\boldsymbol{f}, \boldsymbol{q})$, in that region.

The differential volumetric flow rate through area *dA* is

$$d\dot{q}(\boldsymbol{f},\boldsymbol{q}) = q'''(\boldsymbol{f},\boldsymbol{q})\, u_r(\boldsymbol{f},\boldsymbol{q})\, dA \qquad 7.5$$

where the differential area, $dA = r^2 \sin \boldsymbol{f}\, d\boldsymbol{q}\, d\boldsymbol{f}$, the droplet number count, $N(\boldsymbol{f},\boldsymbol{q})$, in droplets·m^{-3} has been measured in this chapter. The radial velocity, $u_r(\boldsymbol{f},\boldsymbol{q})$, was measured in Chapter 5. The only unknown in equation 7.5 is the average droplet diameter, *D*, which can be related to the total flow through the sprinkler by

$$\dot{Q}_{total} = 4\left(\boldsymbol{p} D^3 / 6\right) \int_{\boldsymbol{f}=0}^{\boldsymbol{p}} \int_{\boldsymbol{q}=0}^{\boldsymbol{p}/2} N(\boldsymbol{f},\boldsymbol{q}) u_r(\boldsymbol{f},\boldsymbol{q}) r^2 \sin \boldsymbol{f}\ d\boldsymbol{q}\, d\boldsymbol{f} \qquad 7.6$$

where $\dot{Q}_{total}$ is the total volumetric flow rate through the sprinkler orifice in m^3·sec^{-1} and the factor of 4 reflects that measurements were made in only one quadrant of the spray.

7.1.1 Droplet Count

Commercial image processing software (Scion Image) was used to locate the droplets in the laser sheet images. The software identifies contiguous regions of uniform gray-scale levels in the image through a perimeter search algorithm. Using this algorithm, the software was used to identify all the individual droplets in the image as well as other noise-type items such as the sprinkler and the water ligaments close to the sprinkler. The algorithm requires that the 256 bit gray-scale images acquired by the PIV camera to be dithered to a black and white (2 bit) image. This was accomplished by choosing a "Threshold" value above which all values were white and below which all

were black. The threshold level was chosen manually for each data-set with the goal of maximizing the visible droplets while minimizing the noise in the image. When the threshold is set too high, the software identifies many noise items as droplets. A threshold value too low results in no droplets identified except in the highest water density region. There is typically a range of about 60 gray-scale levels out of 256 where the number of drops identified is invariant. The threshold was set within this invariant region.

Figure 88 shows an example of a laser sheet image before and after dithering. The Image on the left shows the 256 gray-scale image of a U25B sprinkler at 103 kPa parallel to the frame arms. The image on the right shows the same image after it has been dithered to a black and white image. It is clear that the same droplets are visible in both images.
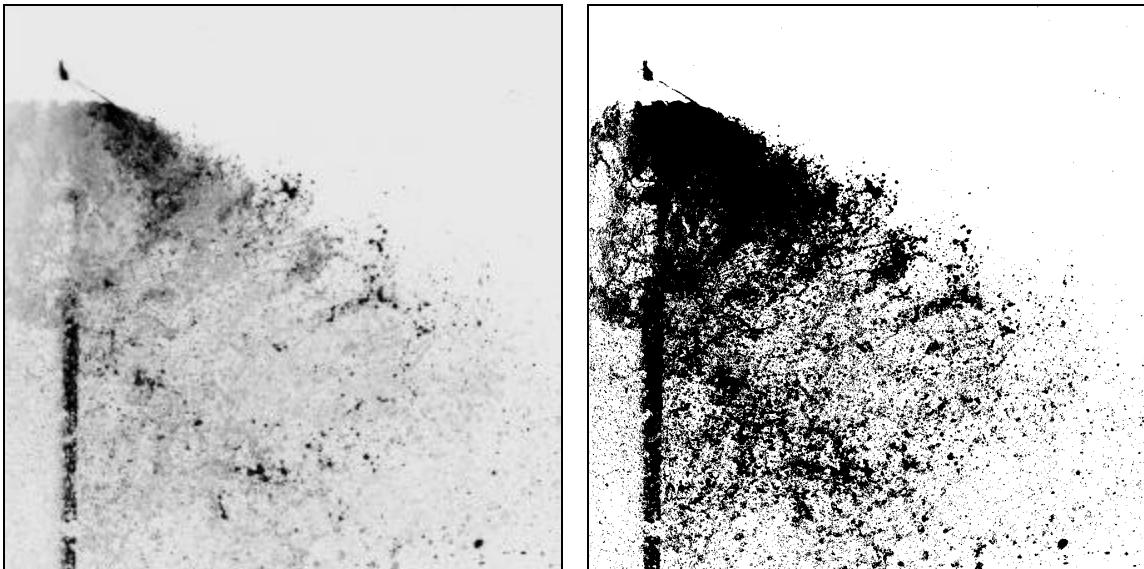
Figure 88. Example of laser sheet image before and after dithering

The position of the water droplets identified using this technique were located using Scion Software for 30 of the laser sheet images at each azimuthal angle. The second image only of the PIV image pairs were used to avoid double counting droplets. The droplets at radial distances between 175mm to 225 mm from the virtual spray origin were extracted from the data and were used for analysis. The droplets found in the analysis region for the P10A and U25A sprinklers are shown in Figure 89. The droplet locations in $\phi=3°$ wide regions have been shaded differently to aid visual analysis. An advantage of this format is that the locations where the water was found is apparent as is the relative density of the water in different regions simply based on the density of dots in the region.

The differences between the P10A and U25A are easily distinguishable. The relative density of the droplets in all regions was much higher for the U25A than for the P10A. The U25A also has large concentrations of droplets to a higher elevation angle than the P10A. The water supply pipe interfering with the spray causes the relatively sparse region of droplets directly below the U25A sprinkler. The P10A sprinkler has a fairly low distribution of droplets in the lower elevation angles $0° \leq \phi \leq 30°$ and a higher concentration of droplets in the $30° \leq \phi \leq 70°$ elevation angles.

P10A   U25A
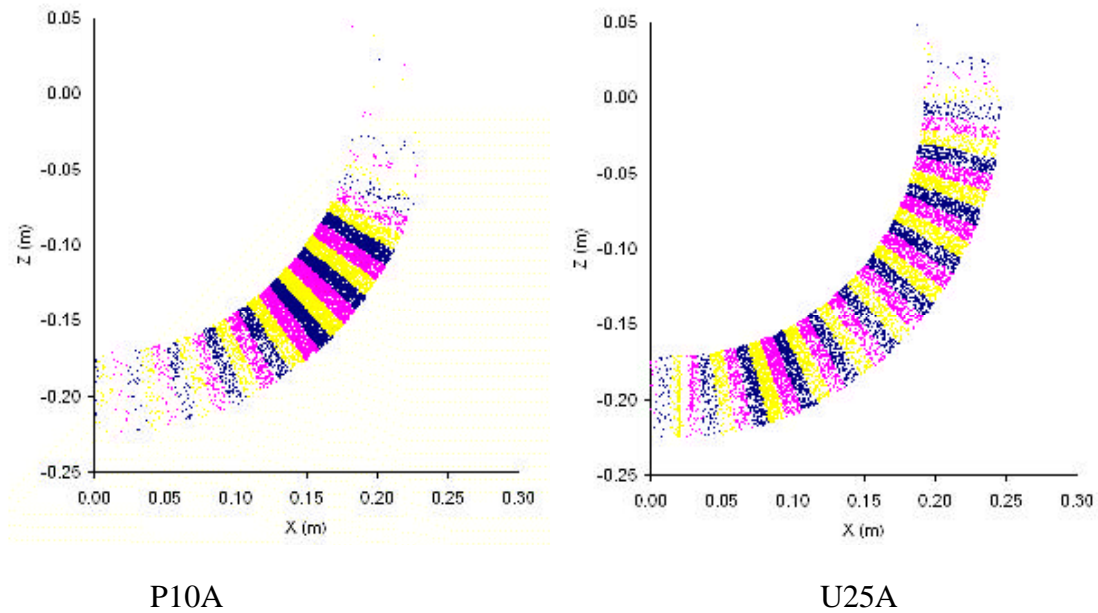
Figure 89. Droplet locations for P10A and U25A sprinklers calculated by image processing software from the laser sheet images. Both figures represent an azimuthal angle $\theta = 90°$ and a water pressure of 48 kPa

The number of droplets found in each data set of 19 azimuthal angles was significant. The maximum number of droplets measured for a sprinkler was 1,139,000 and the minimum was 121,000 with an average of 556,000 droplets measured per sprinkler data set. The maximum number of droplets counted for any sprinkler in a 3° wide region was 8036 droplets in the $13.5° = \phi = 16.5°$ region for the U25A sprinkler at 103 kPa. The average number of droplets counted in a 3° elevation angle region was 845. A summary of the droplet count results is given in Table 11.

Table 11. Droplet count results

Sprinkler	Pressure (kPa)	Total Count	Maximum Count in 3° Region
P10A	48	256876	1640
P10A	138	467769	3385
P10A	221	276130	2604
P13A	59	252261	2525
P13B	131	899134	4244
P14A	48	349333	1805
P16A	48	121365	1368
P25A	103	773085	3483
U16B	48	229625	2115
U25A	48	214990	975
U25A	76	1139122	4257
U25A	103	782294	8036
U25B	103	844303	6466
U25C	103	1071263	5015

The count of droplets was plotted using a polar format similar to the format used for droplet velocity. The virtual spray origin is located at the center of the plot. The polar angles indicate the elevation angle, and the scale of the chart represents the count of droplets measured in a 3° wide region for 175mm ≤ r ≤ 225mm. Figure 90 shows the droplet count as a function of elevation angle for the 19 azimuthal angles for P10A and U25A sprinklers. The highest concentration of droplets was located in the region $60° = \phi = 70°$ for the P10A sprinkler and in the region $10° = \phi = 20°$ for the U25A sprinkler. The shapes of the count curves are different for the two sprinklers. The P10A count has a smooth character and the U25A has a sharp edged and jagged character. This difference in the shape of the number count curves is most likely due to the differences in the design of the sprinklers. The U25 has large square notches (6mm wide) in the deflector whereas the P10A has much smaller (1.5 mm wide) rounded notches.
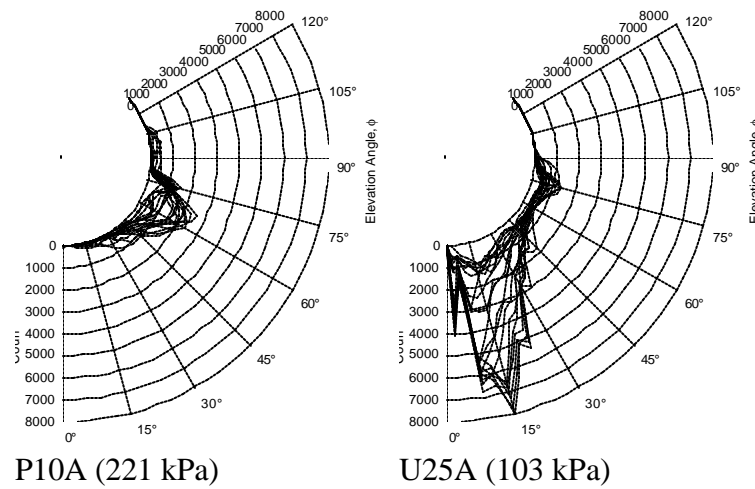
Figure 90. Droplet Count for P10A and U25A

7.1.2 Volume Fraction

When equation 7.7 was solved for the average diameter, *D*, the diameters ranged from 338μm to 990μm with an average of 631μm as shown in Table 12. The *D* values were in the same general range as the diameters measured in the PDI experiments, which lend credibility to this calculation approach. The diameter values calculated using this method were not expected to be equal to those measured using PDI because these diameters are a global average over the entire spray whereas the PDI values are only valid in the measurement location. Once the diameter, D, was known, equation 7.4 was used to calculate the water volume fraction, q''', at each location in the spray at a distance 0.2m from the sprinkler. The maximum q''' measured for each sprinkler spray was calculated along with the average and standard deviation for the locations where q''' was non-zero as shown in Table 12. The maximum q''' measured in a spray ranged from a

low of 0.12% for the sprinkler with the lowest flow rate (P10A at 48 kPa) to a maximum

of 2.81% for the sprinkler with the highest flow rate (U25A at 103 kPa).

Table 12. Average droplet diameter, *D*, and water volume fraction calculated from the visible droplets in the laser sheet image using equation 7.4 and 7.7.

| Sprinkler	Pressure (kPa)	D (μm)	q''' Maximum	q''' Average	q''' Standard Deviation
P10A	48	444	0.12%	0.03%	0.03%
P10A	138	362	0.13%	0.03%	0.03%
P10A	221	413	0.15%	0.02%	0.03%
P13A	59	584	0.42%	0.06%	0.08%
P13B	131	338	0.14%	0.04%	0.04%
P14A	48	620	0.36%	0.10%	0.08%
P16A	48	990	1.11%	0.10%	0.09%
P25A	103	724	1.11%	0.43%	0.30%
U16B	48	749	0.75%	0.12%	0.14%
U25A	48	972	0.75%	0.24%	0.17%
U25A	76	587	0.72%	0.33%	0.20%
U25A	103	747	2.81%	0.40%	0.51%
U25B	103	710	1.94%	0.47%	0.45%
U25C	103	591	0.87%	0.31%	0.23%

Figure 91 and Figure 92 show the q''' for the P10A and U25A sprinklers,

respectively, in the form of polar plots and contour plots. The two plot formats

complement each other because the polar plot provides a representation of the magnitude

while the contour plot presents the elevation angle and azimuthal angle location in an

intuitive format. The lighter contours indicate regions of high water volume fraction.

The polar plot in Figure 91 indicates that the maximum q''' occurs at $\phi = 65°$ at a value of

0.0015. The contour plot shows that there is a high q''' near the frame arms, $\theta < 20°$,

then a sparse region $20° \leq \theta \leq 30°$, followed by another high q''' region $30° \leq \theta \leq 90°$.

For the U25A sprinkler the polar plot shows that the highest q''' are located at low elevation angles, $\phi < 30°$ with a magnitude near 0.02. The polar plot also shows a bimodal shape for q''' with a second smaller peak of about 0.005 at $\phi = 60°$. The contour plot shows that there is significant variation in q'''. There are no sparse regions in the flow as were observed in the P10A sprinkler. The maximum q''' is away from the frame arms, $\theta > 45°$ at the lower elevation $\phi < 30°$. There are also three high q''' regions at $\phi = 80°$ which approximately coincide with sprinkler deflector notches.
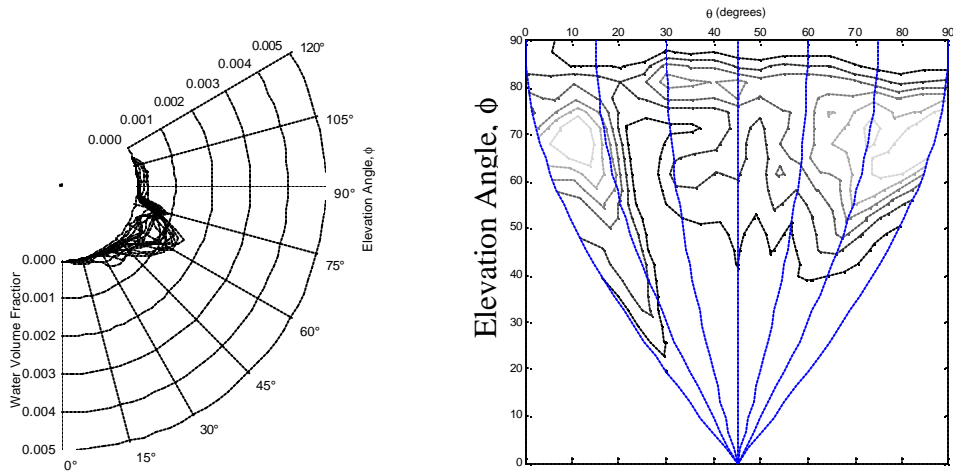
Figure 91. Polar and contour plots of water volume fraction for P10A sprinkler at 221 kPa
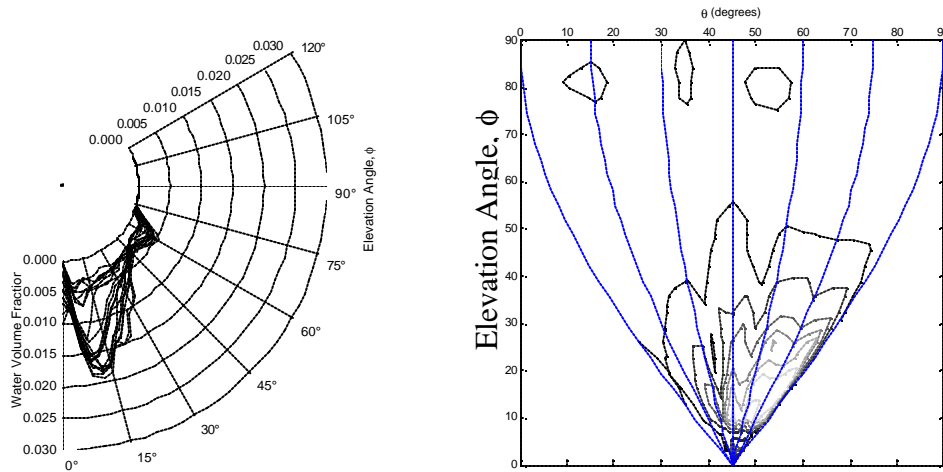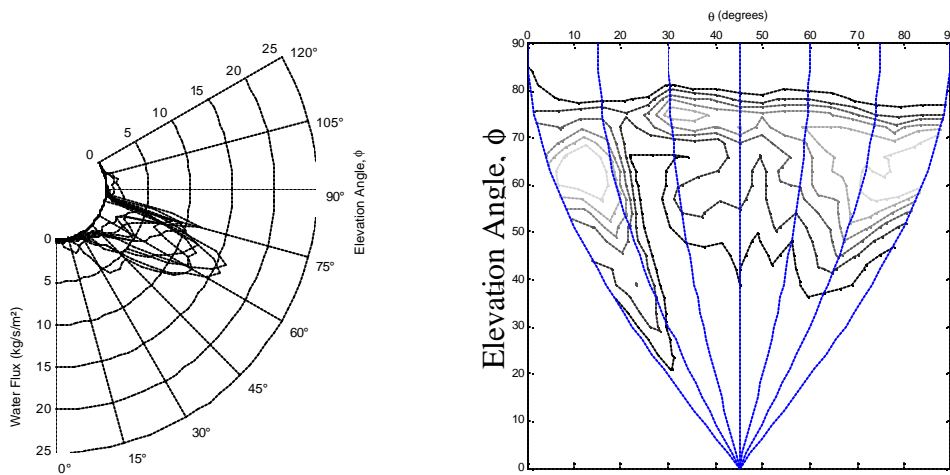
Figure 92. Polar and contour plots of water volume fraction for U25A sprinkler at 103 kPa
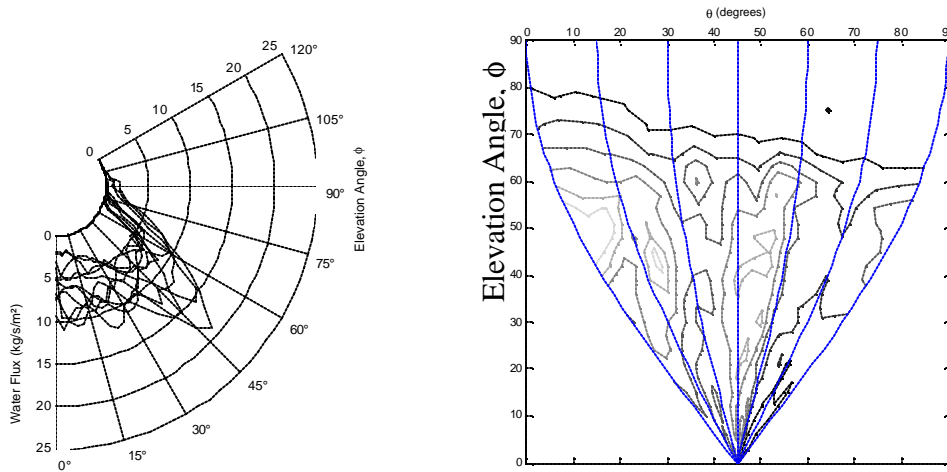
7.2   Water Flux

The mass water flux 0.2m from the sprinkler was calculated using equation 7.1. The flow rate was calculated for each area, *dA*, using equation 7.5. The water flux varied substantially between tests reflecting the wide range of water flow rates and orifice sizes studied. The maximum local flux measured was 215 kg·s^{-1}m^2 for the U25 at 103 kPa and the minimum local flux was 6.7 kg·s^{-1}m^2 for the P10A at 48 kPa. The maximum flux ranged from 2.7 to 9.7 times the average flux for individual sprinklers with a mean maximum flux that was 5.8 times the average flux.

Figure 93 through Figure 95 show the water flux for three pendant sprinklers in meridional planes measured 200mm from the sprinkler. Each sprinkler distributes its water in a dramatically different manner. The P10A sprinkler has a high water flux near the frame arms $\theta < 15°$, $45° < \phi < 75°$ as shown in Figure 93. Next to this high flux region is a relatively sparse region, $15° < \theta < 30°$ followed by another high flux region, $30° < \theta < 90°$

that is narrower in elevation angle, $50°<\phi<75°$. The P14A sprinkler also has a high flux region near the frame arms, $\theta < 20°$, $10°<\phi<65°$ as shown in Figure 94. The upper contour decreases from its maximum, $\phi = 80°$, near the frame arms to a minimum of $\phi = 65°$ perpendicular to the frame arms. This suggests that the frame arms influence the spray by directing it somewhat upward. Nevertheless, the P14A sprinkler distributes the majority of its water flux in the $\phi < 60°$ region. The P25A sprinkler sends its water flux downward at $0°<\phi<35°$ as shown in Figure 95. There is azimuthal variation in the P25A water flux, but it does not follow a trend as with the P10A and P14A sprinklers. The dramatically different water flux profiles for different sprinklers suggests that a universal flux profile for all sprinklers is not possible.

Figure 93. Polar and contour plots of water flux for P10A sprinkler at 221 kPa

Figure 94. Polar and contour plot of water flux for P14A sprinkler at 48 kPa
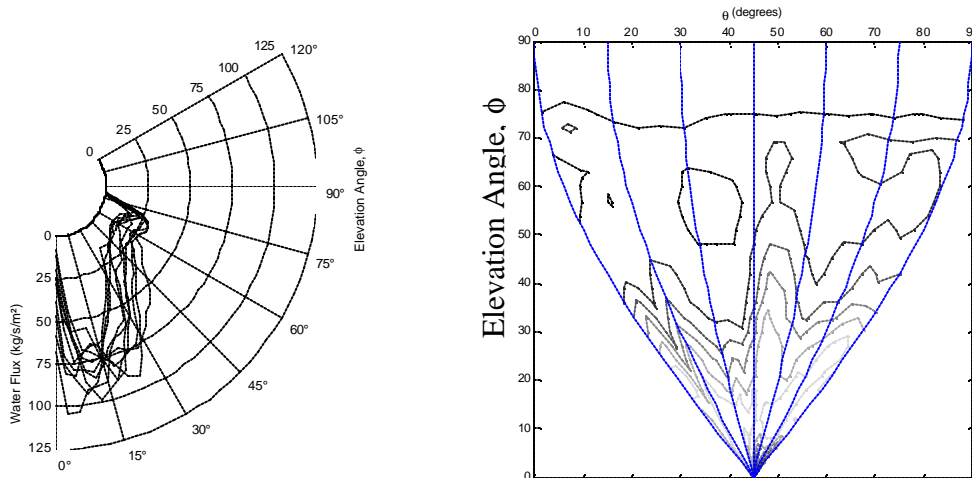
Figure 95. Polar and contour plot of water flux for P25A sprinkler at 103 kPa

Figure 96 through Figure 98 present the water fluxes for three upright sprinklers (scales for individual charts are different). Like the pendant sprinklers each upright sprinkler distributes its water differently from the others. The U16B distributed its water almost horizontally in the 45°<φ<70° region as indicated in Figure 96. The highest water flux is concentrated in two azimuthal regions, 0°< θ <30° and 45°< θ <80°. The U25A distributes its water in the 5°<φ<70° region as shown in Figure 97. There is azimuthal

variation in the water flux including four regions most evident near $\phi = 60°$ that roughly

coincide with deflector notch locations. The U25B sends its water downward in the

$5°<\phi<20°$ regions as shown in Figure 98. The highest water flux is in the $30° < \theta < 90°$

region. There are high flux regions that roughly coincide with deflector notches evident

at $45° < \phi < 65°$. One functional difference between the upright and pendant sprinkler

that is reflected in the water flux results, is that the upright sprinklers cannot propel water

directly below themselves due to the water supply pipe. Thus, the water flux at $\phi = 0°$ is

quite small for upright sprinklers.

The water flux distributions reflect the design intent of the sprinkler designers.

The P10A sprinkler is designed for residential installations where there is typically a low

ceiling and the majority of the fuel is against the walls. For this reason, the P10A

sprinkler delivers most of its water at a high elevation angle with little water directed

downward. The sprinklers with orifices diameters of 14mm and and larger were designed

for high ceilinged areas, such as warehouses and factories. For this reason, these

sprinklers deliver most of their water downward

Figure 96. Polar and contour plot of water flux for U16B sprinkler at 48 kPa

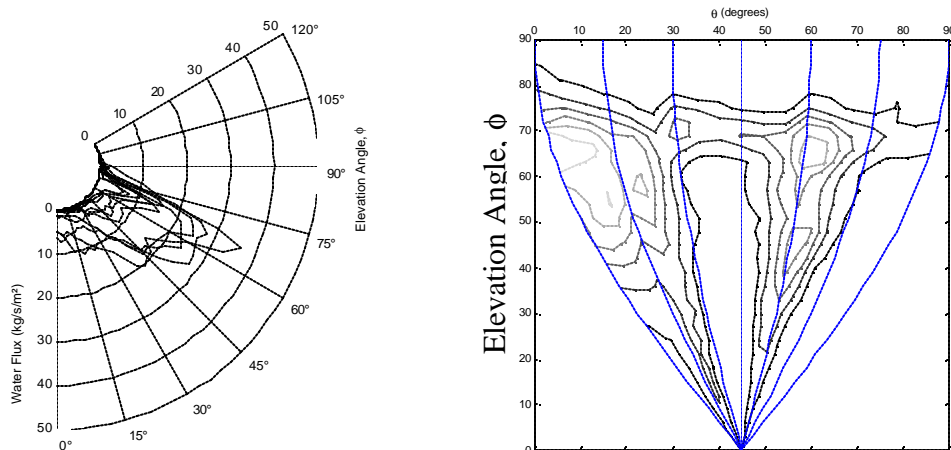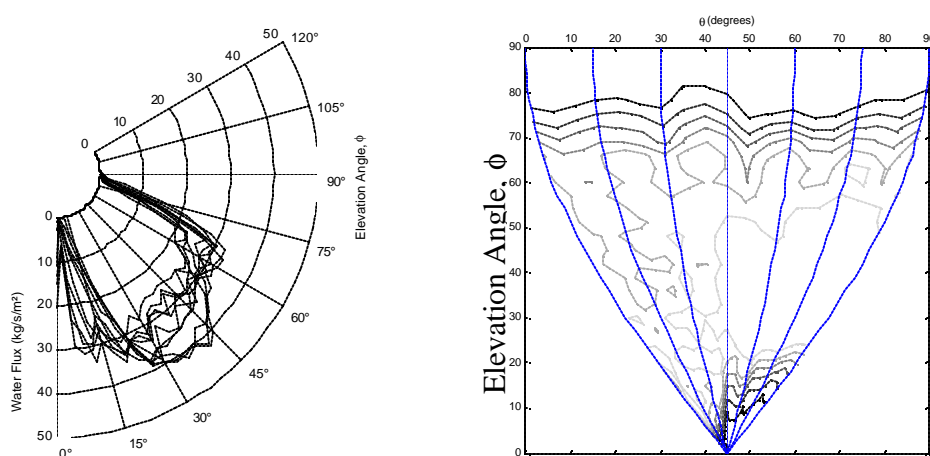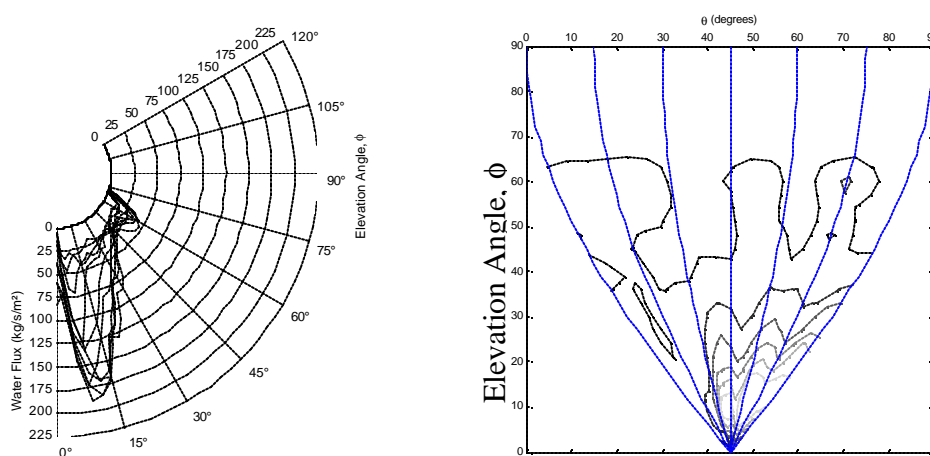**Figure 97. Polar and contour plot of water flux for U25A sprinkler at 76 kPa**

Figure 98. Polar and contour plot of water flux for U25B sprinkler at 103 kPa

7.3   Non-Dimensional Flux

The flux data was nondimensionalized using the total mass flow rate of water through the sprinkler, $\dot{m}_{sprinkler}$, and the surface area of the sphere, A, through which all the flux calculations were based as shown in equation 7.7.
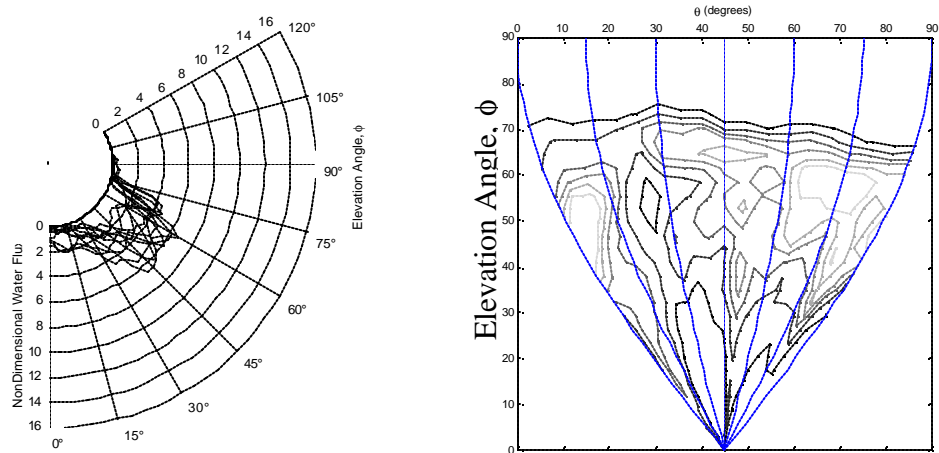
$$\bar{\dot{m}}'' = \dot{m}'' \frac{A}{\dot{m}_{sprinkler}}$$

7.7

where $\bar{\dot{m}}''$ is the nondimensional mass flux, $\dot{m}''$ is local mass flux in kg·sec^{-1}m^2 at a distance 0.2m from the sprinkler, A is in m², and $\dot{m}_{sprinkler}$ is in kg·sec^{-1}. The quantity $\dot{m}_{sprinkler}/A$ is the mass flux if the spray was uniformly distributed over the entire sphere surrounding the sprinkler.

7.4   Flux as a Function of Pressure

For velocity profiles and droplet size distributions there were quantifiable relationships for the effect of pressure. To evaluate if the same would be possible for non-dimensional mass flux the three tests for the P10A and the U25A in which the pressure was varied are plotted as shown in Figure 99 through Figure 101 and Figure 102 through Figure 104, respectively.   The shapes of the flux curves are different at different pressures. For the P10A sprinkler, there are several similarities in the nondimensional flux even as the pressure is varied. First, the maximum non-dimensional flux is 6 to 8 at all pressures. Second, the maximum flux occurs in the region $45° < \phi < 75°$ at all

pressures. Third, one of the regions of high flux is near the frame arms ($0°<\theta<20°$) at an elevation of $40°<\phi<65°$ regardless of the pressure. Finally, other patches of high flux are evident for $60°<\phi<75°$, probably related to flow through the sprinkler deflector notches. On the other hand, there is a measurable flux for $\theta<30°$ at the lower two pressures, but for the 221 kPa test the flux in this range is reduced. For the U25A the dependence of the non-dimensional flux on pressure is more evident. For the lower two pressures, the magnitudes in the polar plots are similar and the flux curves have similar shapes. The magnitude and shape of the 103 kPa flux curve is much different from the tests at the lower pressures. This indicates that as the water pressure is varied, the water distribution leaving the sprinkler deflector changes directing more water downward. Nevertheless, there are significant similarities between the flux distributions. At all three pressures, the effect of the deflector notches is evident for $60°<\phi<80°$. Thus, from Figure 99 through Figure 104, it appears that the pressure can significantly alter the distribution of the mass flux, although many features of the mass flux seem somewhat independent of pressure.

Figure 99. Polar and contour plot of nondimensional flux for P10A sprinkler at 48 kPa
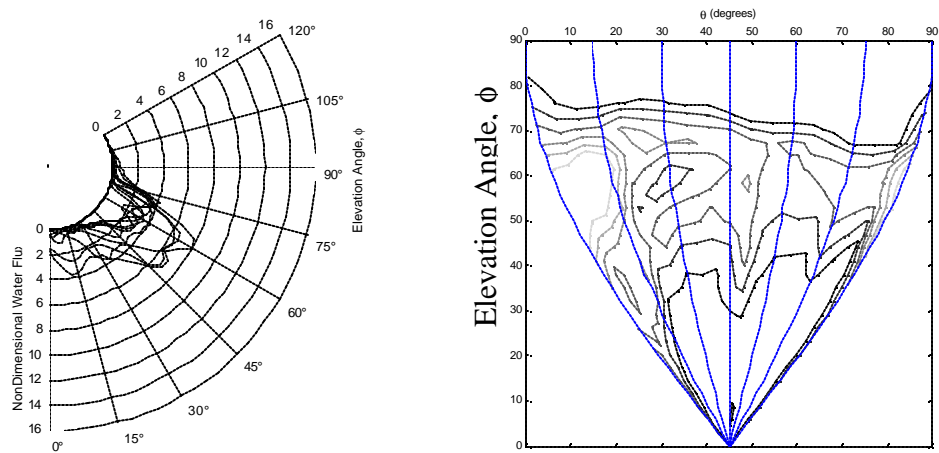
Figure 100. Polar and contour plot of nondimensional flux for P10A sprinkler at 138 kPa
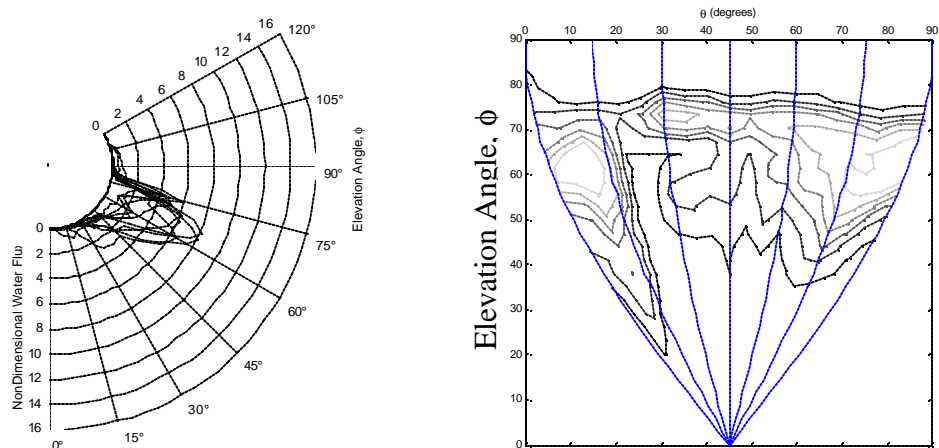
Figure 101. Polar and contour plot of nondimensional flux for P10A sprinkler at 221 kPa

Figure 102. Polar and contour plot of nondimensional flux for U25A sprinkler at 48 kPa
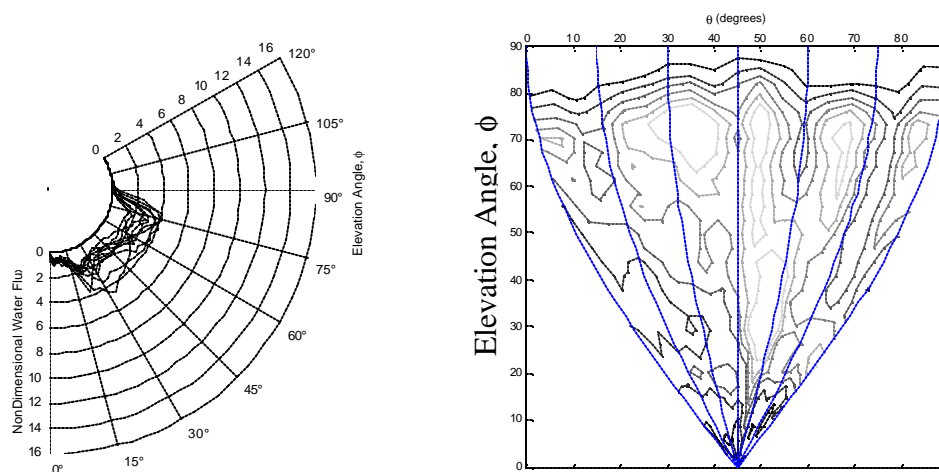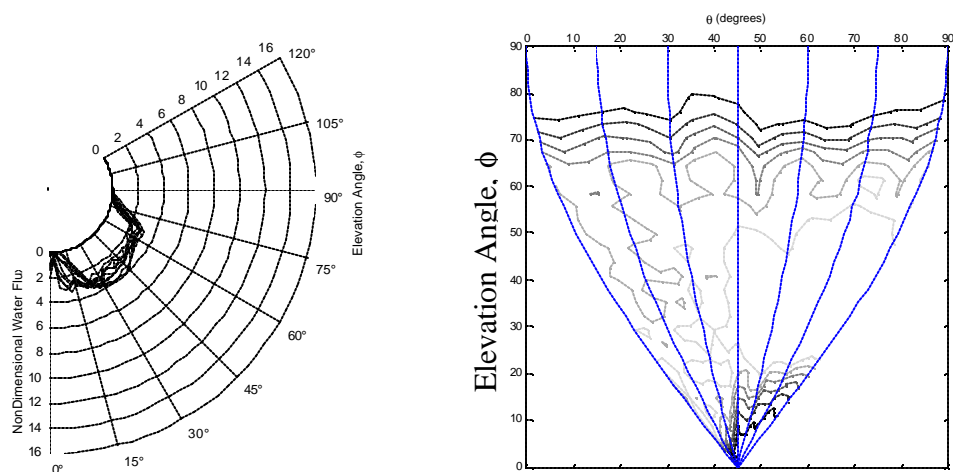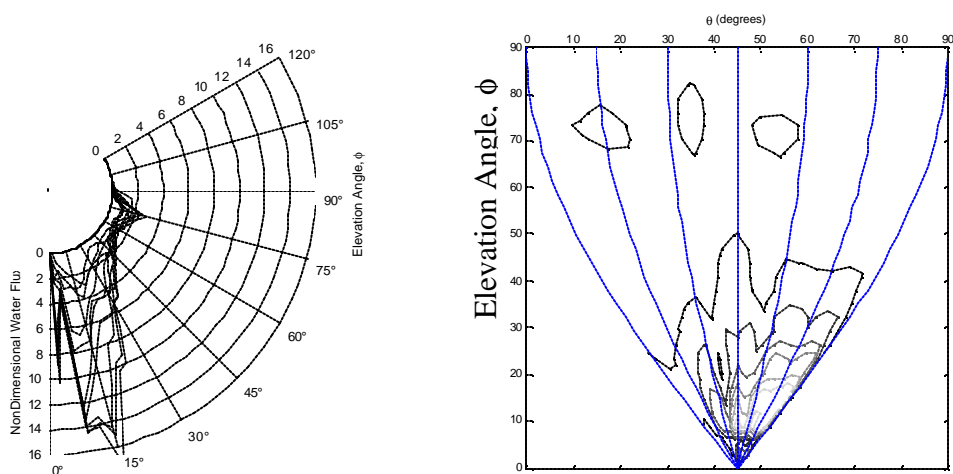
Figure 103. Polar and contour plot of nondimensional flux for U25A sprinkler at 76 kPa

Figure 104. Polar and contour plot of nondimensional flux for U25A sprinkler at 103 kPa

7.5   Average Sprinklers

7.5.1   Axisymmetry of Water Flux

Although it is clear from the preceding sections that the water flux is not axisymmetric, it is still worthwhile to determine the degree of deviation from axisymmetry. The flux was calculated for each sprinkler as an ensemble average of the fluxes measured at different azimuthal angles. The standard deviation of the ensemble averages at each elevation angle was calculated to evaluate the variance in the flux data with azimuthal angle. It was found that the standard deviation in the axisymmetrically averaged flux was typically about 50% of the axisymmetric flux at each elevation angle. An example of this is shown in Figure 105 for three sprinklers. Each chart shows the average nondimensional flux and the standard deviation, σ, of that flux. If the axisymmetric assumption were valid, the average flux would be of much greater magnitude than the standard deviation which is not the case. Therefore it is clear that the flux can not be approximated as axisymmetric.
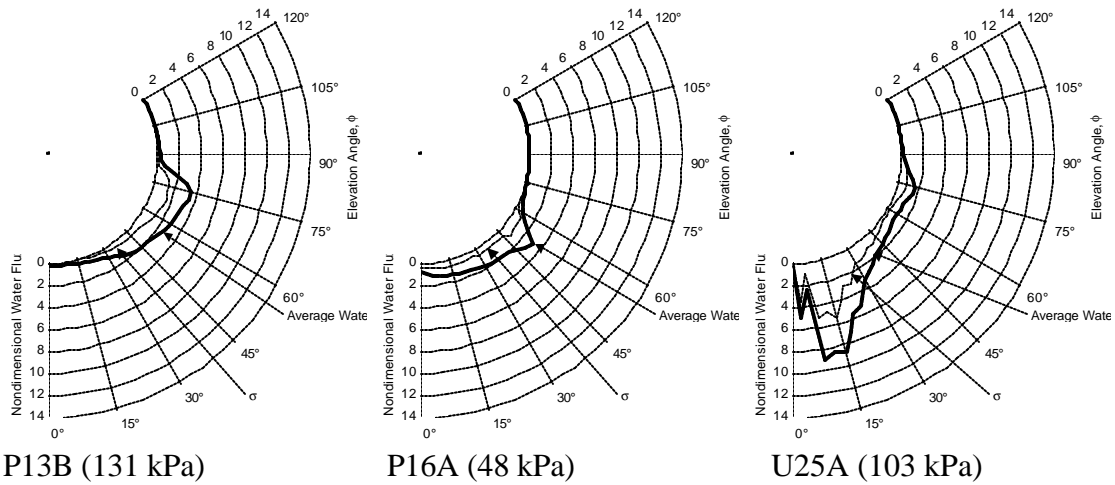
Figure 105. Azimuthally Averaged Flux for P13B, P16A and U25A Sprinklers

7.5.2 Average Over Elevation angle

From the results in preceding sections it is evident that the mass water flux depends on the elevation angle, but it is helpful to determine the degree of variability. Figure 106 shows the flux as a function of azimuthal angle for three test configurations.
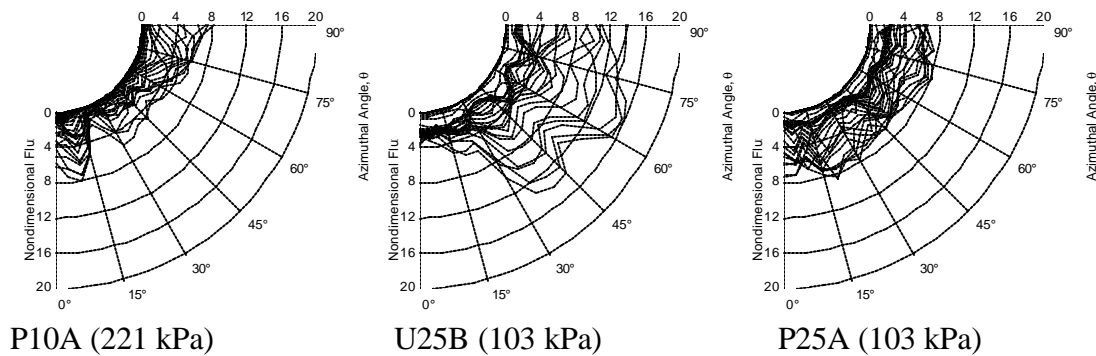
Figure 106. Flux as a function of azimuthal angle for P10A, U25B and P25A

Although it is clear from Figure 106 that the variance in the flux as a function of elevation angle will be high, for completeness the weighted average flux and its standard deviation was calculated for all sprinklers. Figure 107 shows the average (thick line) and

standard deviation for the same data that is presented in Figure 106. It can be clearly

seen that the standard deviation is often larger than the average value. Therefore, the flux

is strongly dependent on elevation angle.

P10A (48 kPa)   P25A (103 kPa)   U25B (103 kPa)

Figure 107. Average Flux as a Function of Azimuthal Angle for P10A, U25B and P25A

7.5.3   Average Flux for All Sprinklers

Average axisymmetric flux profiles were calculated for all tested sprinklers.

Because of the wide variation in the water flux values depending on sprinkler it was

decided to create two average profiles. One profile is for sprinklers with 25mm orifices

and one profile is for all other sprinklers. Figure 108 and Figure 109 show the calculated
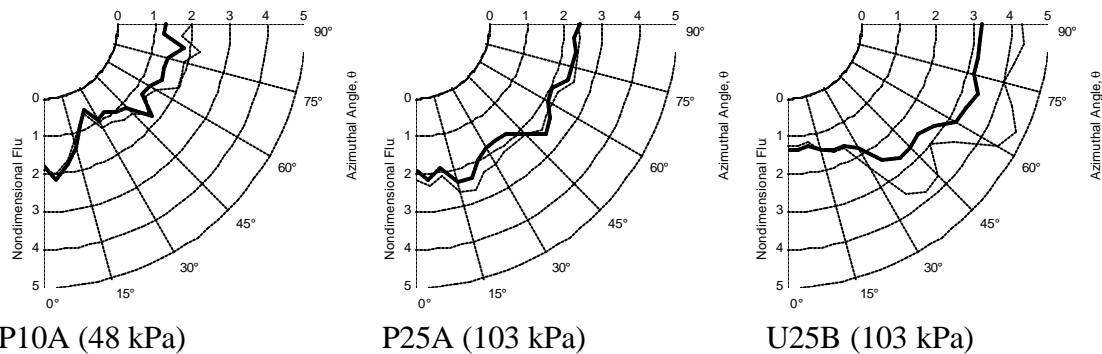
average axisymmetric flux, the standard deviation, σ, and the expected variance from the

average $\pm \sigma$ as a function of elevation angle. The standard deviation was typically 74% of

the average for the 25mm sprinklers and 110% of the average for the smaller orifice

sprinklers. Although there is large variance from the average, these average flux profiles

provide a starting point for researchers that do not have detailed flux data about

individual sprinklers. A point of clarification is in order here. From Figure 108 and

Figure 109 that the flux averaged overall measurements is two to three times the average flux, $\dot{m}A$, (see equation 7.7). But recall A is the area of the entire sphere surrounding the sprinkler. Since nearly all of the spray is in the lower hemisphere, a dimensionless flux of about two is quite reasonable.
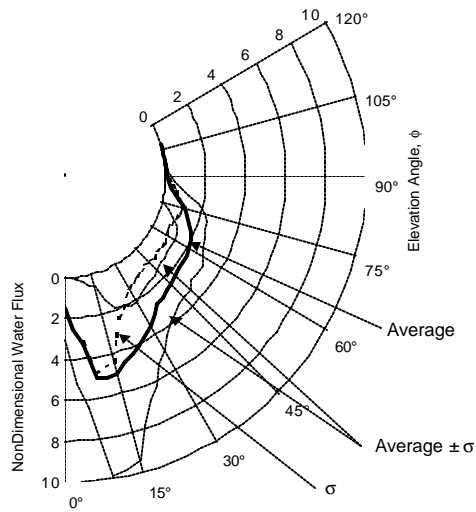
Figure 108. Average nondimensional water fluxes as a function of elevation angle for all tested sprinklers with 25mm orifices.
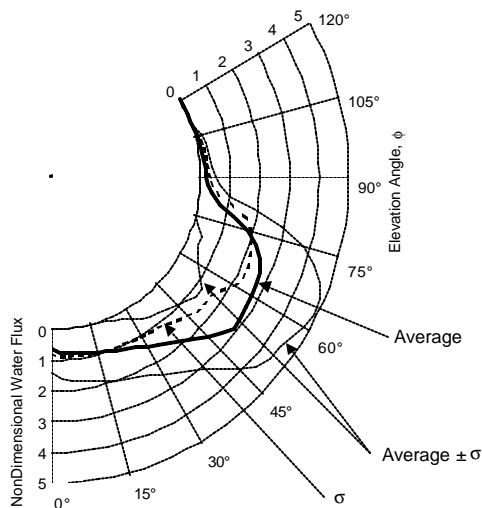
Figure 109. Average nondimensional water fluxes as a function of elevation angle for all tested sprinklers with orifices less than 25mm.

Figure 110 and Figure 111 show the maximum and minimum fluxes measured at each elevation angle for 25mm orifice sprinkler and smaller orifice sprinklers, respectively. The maximum fluxes were 18 and 11 for the 255mm orifice and smaller sprinkler respectively. The minimum fluxes were close to zero for both families of sprinklers reflecting that there were locations where no droplets were found in each family of sprinklers.

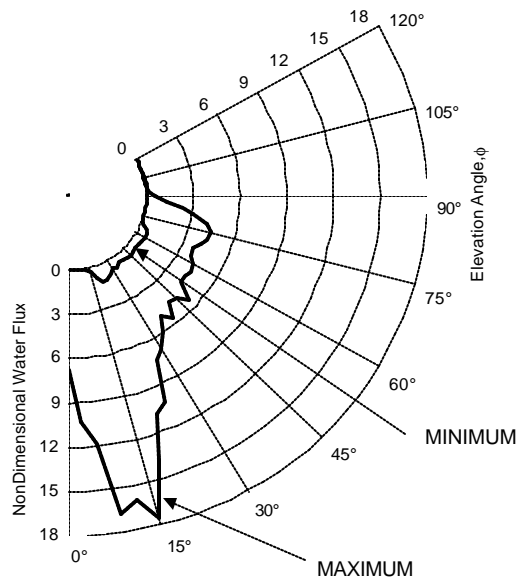**Figure 110. Maximum and minimum water fluxes as a function of elevation angle for all tested sprinklers with 25mm orifices.**
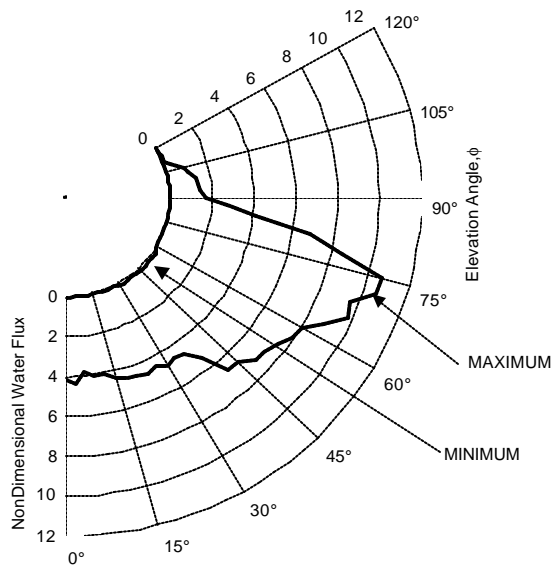
Figure 111. Maximum and minimum water fluxes as a function of elevation angle for all tested sprinklers with orifices less than 25mm.

7.6   Conclusions

The following conclusions can be made from the results discussed in this chapter.

➢ Sprinkler water flux can be calculated using PIV techniques by combining PIV velocities with an estimate of the water volume fraction derived from the PIV images. The water volume fraction can be estimated by a count of the visible water droplets in PIV images with a resolution of 300 μm/pixel or finer because the PDI results in Chapter 6 showed that more than 90% of the water volume is visible in the PIV images.

➢ There is substantial variation in the water flux from sprinkler to sprinkler. The maximum local flux measured was 215 $kg \cdot s^{-1} m^2$ for the U25 at 103 kPa and the minimum local flux was 6.7 $kg \cdot s^{-1} m^2$ for the P10A at 48 kPa.

- ➢ For a given sprinkler, the water flux depends on the location (ϕ, θ). Often regions of flux related to the notches in the deflector are evident.

- ➢ Pressure has a varying effect on the water flux. In some cases, changing the pressure only changes the details of the water flux distribution. In other cases, the changes are more dramatic.

- ➢ The deviations in the water flux distribution are so great that it is impossible to determine a universal water flux profile or to assume axisymmetry in the water flux.

8 Summary

An experimental study was conducted to measure the water spray characteristics near fire sprinklers using state-of-the-art laser diagnostic equipment. The sprays near sprinklers are complex with the spray characteristics of velocity, droplet size distribution, and water flux varying with elevation angle and azimuthal angle with respect to the sprinkler.

The spray velocity near the sprinkler is radial. The shape of the velocity profile varies widely from sprinkler to sprinkler with no differentiation between upright and pendant sprinklers. The maximum radial velocities range from 5.8 to 14.1 $m \cdot s^{-1}$. The ratio of the maximum droplet velocity to average orifice velocity is near 100% for many pendant sprinklers, and the ratio is always less than 100% for upright sprinklers. The non-dimensionalized velocity, $\bar{U} = u_r \sqrt{r/P}$ accounts for the effect of orifice pressure. An overall weighted average nondimensional velocity from all tests was 0.59 with a standard deviation of 0.24. The relationship, $\bar{U}_{avg} \approx 0.6\sqrt{P/r}$, although not perfect, provides a ball-park estimate of the radial velocity close to the sprinkler that has not previously been available. The velocity profiles for 5 of 12 sprinklers could be reasonably modeled as axisymmetric. Many variations in the velocity profile could be linked to sprinkler features (e.g. deflector notches). A typical axisymmetric sprinkler velocity profile was created from all the velocity results with the average nondimensional velocity between 0.6 and 0.8 for elevation angles below $\phi < 75°$. The velocity profile then decreased to a minimum of 0.2 at an elevation angle of $\phi = 111°$. The maximum

nondimensional velocities at each elevation angle for any sprinkler are relatively constant near a value of 1.0 in the region $0° \leq \phi \leq 80°$. At higher elevation angles, $\phi > 80°$, the maximum nondimensional velocity decreases to approximately 0.4 at $\phi = 111°$. The minimum nondimensional radial at each elevation angle for any sprinkler velocity is zero directly below the sprinkler, then it remains fairly uniform near 0.6 for the region $20° \leq \phi \leq 57°$, and drops to zero above $\phi = 60°$ reflecting that some sprinklers spray very little water horizontally.

Sprinkler sprays are composed of a large number of droplets with diameters that span 2 orders of magnitude. The largest number of droplets are typically less than 250μm in diameter, but the majority of the water volume is typically carried by droplets with diameters greater than 300μm. Near the sprinklers more large droplets were present as the elevation angle increased. In some cases, a few large droplets often dominated (20% to 40%) the water volume at a particular measurement point. The shape of the CVF near the sprinklers depends on the sprinkler type, the elevation angle, and the water pressure. The shape of the CVF was unique for each sprinkler and location. In a limited number of cases (less than 50%) the CVF was found to conform to a log-normal, Rosin-Rammler or combination log-normal/Rosin-Rammler distribution. When the CVF curves conformed to a standard distribution, the constants for the distributions were unique for each sprinkler/elevation angle/water pressure combination and no relationship could be found between the constants and location or water pressure. The volume median droplet diameter is proportional to the inverse cube root of the Weber number as postulated by

Dundas [45]. However, the 2.7 proportionality constant that was put forth in the past

[46] is not universal for all sprinklers. The proportionality constants measured in this

study ranged from 0.72 to 2.48 with an average of 1.53. The trajectory analysis from

Chapter 1 suggests that the maximum horizontal distance that a droplet can travel is a

function of the droplet size and the initial velocity of the droplet. Larger droplets are able

to travel further than smaller ones. These experiments corroborate the results of the

trajectory analysis and suggests that the minimum median volume diameter below

sprinklers could be estimated at any location using trajectory analysis.

Sprinkler water flux can be calculated using PIV techniques by combining PIV

velocities with an estimate of the water volume fraction derived from the PIV images.

The water volume fraction can be estimated by a count of the visible water droplets in

PIV images with a resolution of 300 μm/pixel or finer because the PDI results in Chapter

6 showed that more than 90% of the water volume would be visible in the PIV images.

There is substantial variation in the water flux from sprinkler to sprinkler and within each

sprinkler spray. The maximum local flux measured was 215 kg·s^{-1}m^2 for the U25 at 103

kPa and the minimum local flux was 6.7 kg·s^{-1}m^2 for the P10A at 48 kPa. The maximum

flux ranged from 2.7 to 9.7 times the average flux for individual sprinklers. Changes in

pressure alter the distribution of the water flux to varying degrees. In addition, it is

impossible to determine a universal water flux distribution or to assume axisymmetry for

the water flux.

The results of this study are already being put to practical use. The National Institute of Standards and Technology (NIST) has modified its latest computational fluid dynamics model for fires, "Fire Dynamics Simulator," to accept the input for sprinkler sprays provided by this research. In addition, NIST has recently funded large-scale water distribution tests at Underwriters Laboratories using the sprinklers from this study to validate the computational water distribution results in the presence of fires up to 3MW in size.

9 References

1   Grant, G., Brenton, J., Drysdale, D. "Fire Suppression by Water Sprays", Progress in Energy and Combustion Science, Vol 26, pp. 79-130, 2000.

2   Prahl, Joseph M., Wendt, Bruce, "Discharge Distribution Performance for an Axisymmetric Model of a Fire Sprinkler Head", Fire Safety Journal, Vol 14, pp. 101-111, 1988.

3   Huang, J.C.P., "Break-up of axisymmetric liquid sheets", J. Fluid Mech", Vol 43, part 2, pp. 305-319, 1970.

4   Wendt, Bruce, Prahl, Joseph M., "Discharge Distribution for an Axisymmetric Model of a Fire Sprinkler Head", NBS-GCR-86-517, National Bureau of Standards, Gaithersburg, MD, 1986.

5   Chigier, N.A., "The Physics of Atomization", ICLASS-91 Proceedings, National Institute of Standards and Technology, Gaithersburg, MD, pp. 1-15, 1991.

6   Krishnan, G., Gakkar, R.P., Prakash, S., "Water Droplet Evaporation in Fire Plumes", ICLASS-91 Proceedings, National Institute of Standards and Technology, Gaithersburg, MD, pp. 97-104, 1991.

7   Yao, Cheng, "Overview of Sprinkler Technology Research", 5th Conference Proceedings of the International Association of Fire Safety Scientists.

8   "NFPA 13, Standard for the Installation of Sprinkler Systems", National Fire Protection Association, Quincy, MA, 1999.

9   Quintiere, James G., "Principles of Fire Behavior", Delmar Publishers, New York, 1998.

10   Evans, David D., "Ceiling Jet Flows", The SFPE Handbook of Fire Protection Engineering, Section 1, Chapter 9, National Fire Protection Association, First Edition, 1988.

11   Gupta A.K. Fire Plume - Theories and Their Analysis, J. Applied Fire Science, Vol 2(4), 1993.

12   Morton B.R., et. al. Turbulent Gravitational Convection from Maintained and Instantaneous Sources, Proc. Royal Society of London, Vol 234, 1956.

13   The SFPE Handbook of Fire Protection Engineering, Section 1, Chapter 6, National Fire Protection Association, First Edition, 1988.

14   Rayleigh, Lord, "On the Instability of Jets", Proc. London. Math. Soc. 10 4, 1878.

15   Weber, C.,"On the Breakup of a Liquid Jet", Z. Angew Math. Mech. 11 136 1931.

16   Dombrowski, N., Johns, W.R., "The Aerodynamic Instability of and Disintegration of Viscous Liquid Sheets", Chem. Eng. Sci. 18 203, 1963.

17   Dundas, P.H., "The Scaling of Sprinkler Discharge : Prediction of Drop Size", FMRC Serial No. 18792, Factory Mutual Research Corporation, Norwood, MA, 1974.

18   Thooyamani, K.P., Norum, D.I., "Equations Describing Sprinkler Droplet Velocity", Journal Of Irrigation And Drainage Engineering-ASCE, Vol 115, pp. 156-165, 1989.

19   McGrattan, K.B., Baum, H.R., Rehm, R.G., "Large Eddy Simulation of Fire Phenomena", National Institute of Standards and Technology, Gaithersburg, MD, 1998.

20   White, Frank M., "Viscous Fluid Flow", 2nd Ed., MCGraw Hill, Inc., New York,1991.

21   Chan, T. S., "Measurements of Water Density and Drop Size Distributions of Selected ESFR Sprinklers", Journal of Fire Protection Engineering, Vol. 6, No. 2, pp. 79-97, 1994.

22   Allen, Terence., "Particle Size Measurement", 3rd Edition, Chapman and Hall, New York, NY, 1981.

23   ASTM E799-92(1998) Standard Practice for Determining Data Criteria and Processing for Liquid Drop Size Analysis , American Society for Testing and Materials, 2001.

24   Subramaniam S., "Statistical modeling of sprays using the droplet distribution function"., Physics of Fluids, Volume 13, Number 3, March 2001.

25   Faeth G.M. "Evaporation and Combustion of Sprays, Prog Energy Combustion Science", Volume 9, Number 1, 1983.

26   Faeth, G.M., Hsiang, L.-P., Wu, P.K., "Structure and Breakup Properties of Sprays", Int. J. Multiphase Flow, Vol 21, pp. 99-127, 1995.

27   Chow, W.K., Yin, Rumin, "Review of Droplet Size Distributions for a Water Spray", Journal of Applied Fire Science, Volume 7(2), pp 181-194, Baywood Publishing Company, 1998.

28   Hayes, Warren D., "Literature Survey on Drop Size Data, Measuring Equipment and Discussion of the Significance of Drop size in Fire Extinguishment, NBSIR-85-3100, National Bureau of Standards, Gaithersburg, MD, 1985.

29   Widmann, J. F., "Characterization of a Residential Fire Sprinkler Using Phase Doppler Interferometry", NISTIR 6561; 36 p. August 2000.

30   Widmann, J. F. "Phase Doppler Interferometry Measurements in Water Sprays Produced by Residential Fire Sprinklers", Fire Safety Journal, Vol. 36, No. 6, pp. 545-567, September, 2001.

31   Widmann, J. F.; Sheppard, D. T.; Lueptow, R. M., "Non-Intrusive Measurements in Fire Sprinkler Sprays", Fire Technology, Vol. 37, No. 4, 297-315, 4th Quarter, October 2001.

32   Gandhi, P. D.; Steppan, D. "Using PDPA in Evaluation of Sprinklers", U.S./Japan Government Cooperative Program on Natural Resources (UJNR). Fire Research and Safety. 14th Joint Panel Meeting. Proceedings. May 28-June 3, 1998, Tsukuba, Japan, 256-263 pp, 1998.

33   Gandhi, P. D.; Sheppard, D.; Steppan, D. "Role of Component and Large-Scale Testing in the Evaluation and Design of Sprinklers", Fire Suppression and Detection Research Application Symposium. Research and Practice: Bridging the Gap. Proceedings. National Fire Protection Research Foundation. February 25-27, 1998, Orlando, FL, 211-217 pp, 1998.

34   You, Hong-Zeng, "Investigation of Spray Patterns of Selected Sprinklers with the FMRC Drop Size Measuring System", Proceedings of the First International Symposium of Fire Safety Science, pp. 1165-1176, 1986.

35   Adrian, R. J. "Double Exposure, Multiple-field particle image velocimetry for turbulent probability density". Optics and Lasers in Eng., Vol. 9, pp. 211-228, 1988.

36   Adrian, R. J., "Particle-imaging techniques for experimental fluid mechanics". *Annu. Rev. Fluid Mech.*, Vol. 23, pp. 261-304, 1991.

37   Adrian, R. J. & Yao, C. S. "Pulsed laser technique application to liquid and gaseous flows and the scattering power of seed materials". *App. Optics*, Vol. 24, No. 1, pp. 44 – 52, 1985.

38   Westerweel, J. 1997. "Fundamentals of digital particle image velocimetry". Meas. Sci. Technol. Vol. 8, pp. 1379 – 1392.

39   Meinhart, Carl D., Wereley, Steve T., "A PIV Algorithm For Estimating Time-Averaged Velocity Fields", Journal of Fluids Engineering, 122, Issue 2 pp. 285-289

40   Sheppard, D. T.; Lueptow, R. M. "Understanding Sprinkler Sprays : Trajectory Analysis", 15th Meeting of the U.S.-Japan Panel on Fire Research and Safety, San Antonio, Texas, March 2000.

41   Everest D., Atreya A. "PIV Measurements in Large-Scale Sprinkler Flows" Proceedings of PSFVIP-2, Honolulu, USA, May 16-19, 1999.

42   Everest D., Atreya A. "Simultaneous Measurements of Drop Size and Velocity in Large-Scale Sprinkler Flows Using Particle Tracking and Laser-Induced Fluorescence." TO BE PUBLISHED *******

43   "Incite PIV System", Version 3, TSI Incorporated, St. Paul, MN 55164, U.S.A.

44   "NFPA 13, Standard for the Installation of Sprinkler Systems", National Fire Protection Association, Quincy, MA 1999.

45   Dundas, P.H., "Technical Report Optimization of Sprinkler Fire Protection The Scaling of Sprinkler Discharge : Prediction of Drop Size", FMRC Serial No. 18792 RC73-T-40, Factory Mutual Research Corporation, Norwood, MA, June 1974.

46   Lawson J.R., Walton W.D., Evans D.D., "Measurement of Droplet Size in Sprinkler Sprays", NBSIR 88-3715, National Bureau of Standards, Gaithersburg, MD, February 1988.

47   "UL199 Automatic Sprinklers for Fire-Protection Service", 10th edition, Underwriters Laboratories, Northbrook, IL, 1997.

48   Everest D., Atreya A. "Simultaneous Measurements of Drop Size and Velocity in Large-Scale Sprinkler Flows Using Particle Tracking and Laser-Induced Fluorescence."